Federal Agency	U.S. Department of Energy Office of Fossil Energy
FOA Name	Energy Storage for Fossil Power Generation
FOA Number	DE-FOA-0002332
Award Number	DE-FE0032005 Project manager: Sarah K. Michalik
Project Title	**Reversible Methane Electrochemical Reactors as Efficient Energy Storage for Fossil Power**
Name, Title, Email Address, and Phone Number for the Prime Recipient	**Technical Contact :** Pejman Kazempoor, Associate Professor, pkazempoor@ou.edu, 405-325-7885
Prime Recipient Name and Address	University of Oklahoma 865 Asp. Ave., Felgar Hall, Norman, OK 73019
Prime Recipient's DUNS number	848348348
Principal Investigator(s)	**PI:** Associate Professor Pejman Kazempoor Director of Sustainable Energy and Carbon Management Center **Co-PI:** Assistant Professor Chuancheng Duan, *Kansas State University*
Period Covered by the Report	Final Report March 03,2021-September 31, 2023
Signature of Principal Investigator:	P.kazempoor _____ _____ Pejman Kazempoor

ACKNOWLEDGMENT
This material is based upon work supported by the Department of Energy under Award Number DE-FE0032005.

DISCLAIMER
This report was prepared as an account of work sponsored by an agency of the United States Government. Neither the United States Government nor any agency thereof, nor any of their employees, makes any warranty, express or implied, or assumes any legal liability or responsibility for the accuracy, completeness, or usefulness of any information, apparatus, product, or process disclosed, or represents that its use would not infringe privately owned rights. Reference herein to any specific commercial product, process, or service by trade name, trademark, manufacturer, or otherwise does not necessarily constitute or imply its endorsement, recommendation, or favoring by the United States Government or any agency thereof. The views and opinions of authors expressed herein do not necessarily state or reflect those of the United States Government or any agency thereof.

Table of Contents

List of Figures

List of Tables

1. Executive Summary

Reversible Protonic Electrochemical Cells (RePECs) present a promising solution to the integration of fossil fuel assets and energy storage challenges by facilitating the conversion between electrical and chemical energy while concurrently addressing carbon emissions. In electrolysis mode, PCERs transform electricity into durable, storable chemical fuels like syngas and methane. Conversely, these chemical fuels serve as fuel cell reactants, generating electricity on demand with minimal to zero emissions. Overcoming challenges related to optimal operation and high roundtrip efficiencies is crucial for the widespread adoption of such electrochemical cells. This report explores the integration of RePCECs with fossil fuel power plants and renewable energy sources, offering a potential energy storage solution.

The study utilizes experimental tests, computational modeling at various scales, and life cycle analysis to design and assess integrated RePCEC systems. Outcomes include experimental performance curves, a thermodynamic examination, calibration of cell and stack models, and steady-state simulation within a 600MW combined cycle power plant with carbon capture and wastewater treatment units. At full power plant load, stack and system roundtrip efficiencies can reach 72% and 51.37%, respectively. Further analysis at atmospheric pressure and 525℃ suggests an achievable high stack roundtrip efficiency, reducing overall system energy consumption and yielding a levelized cost of methane at $2.24/MMBtu. The life cycle analysis reveals a lower global warming potential compared to conventional methods. These findings, addressing both environmental and economic concerns, underscore the potential of RePCEC systems in large-scale energy storage and carbon emission reduction. With supportive governmental policies and incentives, these advancements could disrupt Energy storage industry, making RePCEC systems favorable for widespread implementation and commercialization.

2.0 Project Objectives

The overall objective of the project was to conduct a comprehensive Research & Development (R&D) program to demonstrate the suitability and future advancement and integration of reversible methane protonic ceramic electrochemical reactors (PCERs) as an efficient Energy Storage System (ESS) with fossil fuel power plants. Fundamental process and system models are developed to conduct a preliminary conceptual study and investigate the power plant system integration requirements, performance requirements, and technical and non-technical gaps for eventual implementation at system level. Technology maturation requirements is also investigated through identifying the critical technical elements and networking with industrial technology developers and end-users.

3. Description of Activities Performed

Technical progress is evaluated in alignment with the tasks outlined in the Statement of Project Objectives and milestones defined in the Project Management Plan. Further details on achievements are elaborated below.

1. Project Management and Planning

All quarterly reports and annual meetings were successfully conducted according to the established schedule.

2. Define the Proposed Energy Storage Technology:

We employed approaches including end-state approach as a systematic method in systems engineering to define the reversible methane PCER technology and identify the technology development requirements. A summary of the materials was compiled through a review of existing activities to comprehend the current state of technology, with highlighted advancements. Based on these studies, we identified gaps and subsequently summarized the current status in comparison to the expected outcomes outlined by the Department of Energy (DOE).

Reviewing the exciting materials and documents regarding the proposed technology, potential challenges are listed below:

- While reversible electrolysis cells offer versatility, there are efficiency losses associated with the reversible operation. Optimizing the design and materials is essential to mitigate these losses.
- Frequent cycling between electrolysis and fuel cell modes can pose durability challenges for the cell components. It is essential to choose materials that are compatible with both modes. For example, robust catalysts, stable ionomers, and corrosion-resistant electrodes.
- Follow up proper procedures during mode transitions is mandatory. Gradual changes in current and potential reduce stress, while sudden shifts can have adverse effects on component health and should be avoided.

Recent studies have focused on optimizing the microstructure of cell components, exploring new materials, and improving manufacturing processes to address efficiency and durability challenges. Though significant progress has been achieved in durability and cost analysis, however, cell performance and degradation rates are far away from the target of DOE and PCECs need to be efficiently integrated with other technologies, such as renewable energy sources or gasifiers.

Ensuring seamless integration and optimizing the overall system efficiency can be challenging and time-intensive. Till now system level study is not reported widely in literature. DOE has set a target to achieve a certain goal by 2030 in system level. Identifying and developing suitable materials for electrodes, electrolytes, and interconnects that balance performance, cost, and durability can be a time-consuming process. While progress in system-level studies of PCECs may be perceived as slow, ongoing research and development efforts, collaborative initiatives, and advancements in related fields are expected to contribute to the maturation of this technology over time. As technology advances and challenges are addressed, the pace of development may accelerate.

3. Experimental Studies to Define Reversible Methane PCER Performance Parameters

The results generated through Task 2 reveal areas of improvement and identify new materials that can enhance the efficiency and performance of the PCERs. The KSU team with OU support has conducted significant experimental studies to measure the current performance of the cells. Building on the areas of improvement suggested in Task 2, they have investigated the feasibility of different methods to enhance the performance and operation of Protonic Ceramic Cells (PCERs).

The goal of this task, following the completion of experimental tests, is to comprehend the novel features of the proposed technology. Performance curves representing the proposed technology's performance under various operating conditions have been established. Such curves are crucial for setting parameters required for the techno-economic evaluation of the concept.

3.1. Enhancing the CO_2 methanation activity

We demonstrated an extremely straightforward approach to enhance the CO_2 methanation activity of samarium-doped ceria-supported Ni (SDC-Ni) by altering the chelating agent-to-metal cation ratios (C/I ratios) and tuning the metal-support interactions. This approach can simultaneously modulate the morphology of Ni, crystal structure, chemical composition, and electronic structure of SDC-Ni. A C/I ratio of 0.1 gives rise to the highest CO_2-to-CH_4 yield at 250 °C (73.6%) among the catalyst studied in this work. The enhanced performances are attributed to the fact that SDC-Ni-0.1 concurrently exhibits the largest metallic Ni surface area, the highest Ni dispersion, high-area active interface, and strong metal-support interaction. These unique properties drastically reduce the C-O bond cleavage activation energy, which significantly facilitate formate decomposition, formyl hydrogenation, and subsequent methoxy-to-CH_4 conversion, leading to exceptional CO_2 conversion and CH_4 yield at 250 °C.

SDC-Ni-*x* (x=0, 0.01, 0.05, 0.1, 0.5 and 2.0) catalysts are synthesized via one-pot wet-chemistry method illustrated in Figure S1. A stoichiometric amount of samarium nitrate, cerium nitrate, and nickel nitrate is mixed with a certain amount of citric acid (CA) and ethylene glycol (EG). Metal citrates are first formed, reacting with the ethylene glycol, namely polyesterification, to generate a covalent network with trapped Sm, Ce, and Ni ions. The produced gel is subsequently dried and fired in air to synthesize CO_2 methanation catalysts. The C/I ratios can therefore determine the amount of polyesterified network and consequent homogeneity of metal ions dispersed throughout the network.

This facile one-pot approach can readily fabricate a composite of SDC and NiO under a wide range of C/I ratios (Figure S2 and Table S1. After reduction, the catalysts can then be reduced to SDC-supported Ni (Figure S3 and Table S2). No impurity phase is observed, validating that this approach could be applied for synthesizing SDC-Ni-*x* catalysts. The impact of C/I ratio on the surface area is shown Table S3. A surface area of 16.11, 24.96, and 30.57 cm^2/g is obtained under a C/I ratio of 0.01, 0.1, and 2.0, respectively. Increasing the C/I ratio causes a higher polyesterification rate, resulting in more covalent networks and consequently leading to higher porosity.

To understand the impact of Sm doping, CeO_2-supported Ni with 20 wt.% Ni (CeO_2-Ni-0.1) was synthesized via the same approach as SDC-Ni-0.1. The CH_4 yield over SDC-Ni-0.1 almost doubles the performance of CeO_2-Ni-0.1 (Figure S4A) at 250 °C, indicative of the beneficial impacts of Sm doping. We also compare the performances of SDC-Ni-0.1 with SDC-supported impregnated Ni (SDC-Ni-0.1-IM) and noted that the CH_4 yield of SDC-Ni-0.1 is more than six times higher than that of SDC-Ni-0.1-IM at 250 °C (Figure S4B). By employing this wet-chemistry catalyst synthesis approach, the CH_4 yield at 250 °C has been improved from ~11.2% to 73.3%, suggesting this method leads to enhanced metal-support interactions than wet impregnation.

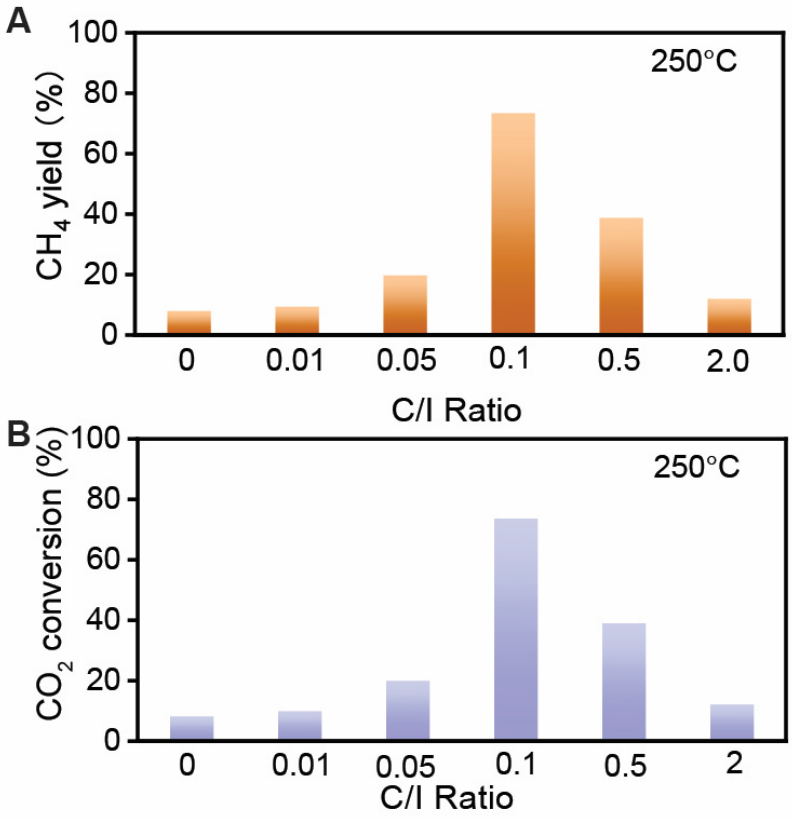

Figure 3.1. Catalytic performances of SDC-Ni-x (C/I ratio x = 0, 0.01, 0.05, 0.1, 0.5 and 2.0). (A) CO2-to-CH4 yield over SDC-Ni catalysts synthesized under various C/I ratios. (B) CO2 conversion as a function of the C/I ratio.

We then studied how to further tune the metal-support interactions by modulating the C/I ratio. The CH_4 yield as a function of the C/I ratio displays a volcano-like trend at 250 °C (Figure 3.1A).

SDC-Ni synthesized with a C/I ratio of 0.1 (i.e., SDC-Ni-0.1) exhibits the highest CH_4 yield (73.6%), which represents outstanding CO_2 methanation performances at 250 °C (Table S4). The CH_4 yield over SDC-Ni-0.1 is more than seven times and six times higher than SDC-Ni-0.01 and SDC-Ni-2.0, respectively. As shown in Figure S5 turnover frequency (TOF) of SDC-Ni as a function of the C/I ratio also shows the same trend, which implies modulating the C/I ratio can significantly tune the catalytic properties. An excessive amount of chelating agents, for instance, a C/I ratio of 2.0, is generally used to synthesize catalysts with small particle size and high surface areas. However, a C/I ratio of 2.0 does not give rise to the best catalytic performances. It has been recognized that the C/I ratio can substantially affect the CO_2 conversion while its impacts on CH_4 selectivity is not obvious (Figure 3.1B and Figure S6). For example, at 250 °C, SDC-Ni-0.1 shows a CO_2 conversion of 73.6%, which is 7.5 time of SDC-Ni-0.01 and 6.1 time of SDC-Ni-2.0. Moreover, this approach is also applied for synthesizing CeO_2-Ni catalysts. At 250 °C, the CH_4 yield over CeO_2-Ni-0.1 is ~13 times higher than that of CeO_2-Ni-2.0 (Figure S7), which suggest altering the C/I ratio could be employed to modulate various catalysts. Additionally, SDC-Ni-0.1 achieves a CH_4 selectivity of >99.5% that is slightly higher than the other four catalysts (Figure S6). Even at a H_2/CO_2 ratio of 1:1, SDC-Ni-0.1 also enables highly selective CO_2 hydrogenation to CH_4, implying the created active sites favor a certain CO_2 methanation pathway, which is not greatly impacted by the H_2/CO_2 ratio (Figure S8).

Both CH_4 yield and long-term durability are essential for economic CO_2 methanation and large-scale commercialization. We therefore determine the long-term stability of SDC-Ni-0.1 at 300 °C and 250 °C (Figure S9). There is no observable degradation after 700 hours of operation at 300 °C and an additional 700 hours of testing at 250 °C. After 1400 hours of testing, the temperature was increased back to 300 °C, the CH_4 yield can be almost recovered back to its initial performances, revealing its better stability. Post-mortem characterizations of the catalyst show no apparent agglomeration or coking (Figure S10).

3.2. Impacts of the C/I ratio on metal-support interactions, morphology, chemical composition, crystal structure, and electronic structure:

The metal-support interactions could be evidenced by the H_2 temperature-programmed reduction (H_2-TPR) profiles. H_2-TPR was therefore performed on SDC-Ni-*x* (*x* = 0.01, 0.1 and 2.0, Figure 3. 2A). There are three reduction peaks falling in the range of 365-410 °C (α), 430-470 °C (β), and 460-505 °C (γ), which are attributed to the NiO species with different extent of interactions with the SDC support [43, 44]. With increasing the C/I ratio, the peaks slightly shift to higher temperatures, indicating a high C/I ratio tends to decrease the reducibility of Ni species. In other words, the shift of reduction peaks to higher temperatures implies the presence of stronger Ni-support interactions [44]. Additionally, with increasing the C/I ratio, the α and γ peak area tends to increase while the β peak area decreases (Figure S11). Typically, the α peak is ascribed to NiO with a relatively small size while the β peak is attributed to NiO with a larger particle size [31, 45]. Increasing the C/I ratio tends to produce a higher amount of polyesterified network, which can give rise to a smaller grain/particle size (Figure 3. 2B). For example, a C/I ratio of 0.01 leads to a Ni grain size of 26.9 nm and SDC grain size of 11.4 nm, while the grain size of Ni and SDC can be reduced to 7.6 nm and 7.4 nm at a C/I ratio of 2.0 (Figure 3. 2B and Figure S12). This is consistent with the TPR

result that the β peak area of SDC-Ni-2.0 is higher than that of SDC-Ni-0.01. It is also noted that the particle size of Ni is more sensitive to the C/I ratios while the particle size of SDC is relatively similar, suggesting altering the C/I ratio can significantly tune morphology of metallic phase. Figure 3. 2A shows that an additional reduction peak (γ) presents in the TPR profile. The γ peak could be attributed to the exsolution of Ni nanoparticles from the SDC lattice, displaying the strongest metal-support interaction. As impregnation cannot dope SDC with Ni, H_2-TPR was also performed on SDC-Ni-0.1-IM, which does not display the γ peak (Figure S13), affirming the γ peak is related to the exsolution of Ni from SDC lattice. These results indicate this wet-chemistry approach can lead to stronger metal-support interactions than impregnation while modulating the C/I ratio could fine-tune the metal-support interactions. Additionally, the strong metal-support interactions could enhance the thermal stability of Ni nanoparticles and prevent its coarsening, which is essential for its long-term stability [44, 46].

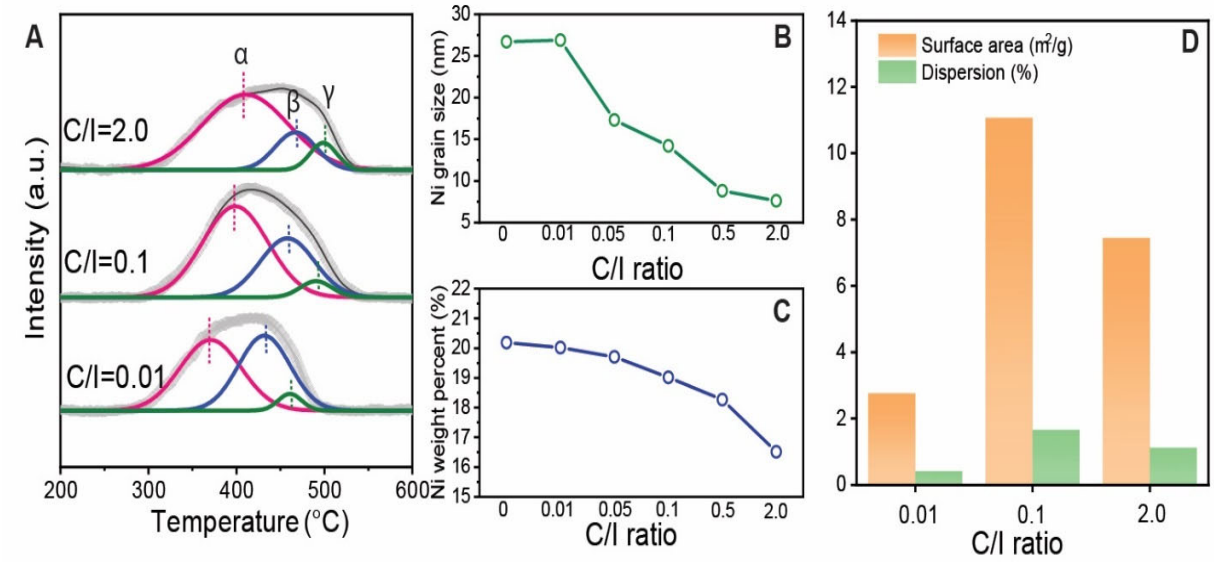

Figure 3. 2. Impacts of the C/I ratio on structural properties of SDC-Ni-x. (A) H2-TPR profiles of SDC-Ni-x (x = 0.01, 0.1 and 0.2). (B) The Ni grain size as a function of the C/I ratio. (C) The amount of metallic Ni as a function of the C/I ratio. (D) The metallic Ni surface area and dispersion of SDC-Ni-x (x = 0,01, 0.1, and 0.2).

Extensive efforts have been devoted to fabricating catalysts with increasingly smaller particles. However, simply reducing the particle size of Ni nanoparticles does not successively improve the catalytic activity [28], while the intermediate Ni particle size potentially lead to the highest catalytic activity (Figure 3.1A and Figure 3. 2B). Therefore, the particle size is not the only determination factor that affects the catalytic performance. Increasing the C/I ratios can also enhance the amount of Ni ions entangled in the polyesterified networks, thus, increasing the amount of Ni doped into the SDC lattice (Figure S14). Figure 3. 2C shows the weight percent of Ni present in reduced SDC-Ni as a function of the C/I ratio. The Ni loading of these catalysts is initially designed as 20 wt.%. The weight percent of metallic Ni in SDC-Ni-0.01 is ~20.0 wt%, indicating the Ni doped into SDC

is negligible. Increasing the C/I ratios enhances the amount of Ni incorporated into the SDC lattice (decreasing the amount of metallic Ni), leading to ~1.0 wt. % Ni doped in SDC at C/I=0.1 and ~3.5 wt.% Ni doped in SDC at C/I=2.0. As the ionic radius of Ni ions (55 pm) is smaller than Sm ions (95.8 pm) and Ce ions (87 pm) [47], a high C/I ratio could increase the Ni concentration in SDC and consequently decrease the lattice constant of SDC , while the C/I ratio does not impact the lattice parameters of NiO and Ni (Figure. S15). It should also be noted that the lattice constants of reduced SDC are bigger than as-fired SDC (Figure S15A), which could be ascribed to the exsolution of Ni nanoparticles from the SDC lattice or the reduction of Ce^{4+} to Ce^{3+} ions. The amount of exsolved Ni nanoparticles and the total metallic Ni surface area are key to the CO_2 methanation activity. H_2 pulse chemisorption was conducted to determine the metallic Ni surface area and its dispersity. There is a consensus in the existing studies that smaller metallic particles with high dispersion exhibit larger active metal surface area, giving higher H_2 uptake capacity[48]. While SDC-Ni-0.1 catalyst, with the medium particle size, possesses the highest the Ni surface area and dispersity (Figure 2D). It should be noted that the metallic Ni surface area is determined by the amount of metallic Ni and its particle size. Increasing the C/I ratios is beneficial to obtaining smaller Ni particles (Figure 2B). However, it will also promote the Ni diffusion into SDC lattice, decreasing the amount of metallic Ni (Figure 3. 2C). Thus, an intermediate C/I ratio (0.1) results in the highest metallic surface area and Ni dispersion, which consequently leads to the best catalytic performances.

X-ray photoelectron spectroscopy (XPS) was also performed to establish the C/I ratios – electronic structure relationships. Figure 3. 3 and Table S5 summarize the XPS analysis results of reduced representative SDC-Ni-x (x= 2.0, 0.1, and 0.01). Figure 3. 3A shows that increasing the C/I ratio tends to enhance the oxygen vacancy concentration, which is due to the higher amount of Ni doped into SDC (Figure S14). The essential role of oxygen vacancies in CO_2 methanation has been proven, showing higher oxygen vacancy concentration could improve CO_2 conversion[31] . However, as a C/I ratio of 2.0 increases the doping of Ni in SDC, the amount of metallic Ni is low at a C/I ratio of 2.0 (Figure 3. 2C), which indicates SDC-Ni-2.0 cannot deliver the highest catalytic performance. The signal of Ni^{3+} can be clearly distinguished from that of Ni^{2+} ions (Figure 3. 3B). Distinctly, with increasing the C/I ratio, the amount of Ni^{3+} increases and SDC-Ni-2.0 exhibits the highest amount of Ni^{3+}. The exsolution of Ni nanoparticles creates Ni vacancies in the SDC, which oxidizes some Ni^{2+} ions to Ni^{3+} ions to maintain the charge neutrality [49, 50]. It has been recognized that the abundance of existing Ni vacancies and Ni^{3+} ions could also induce the stronger metal-support interactions and enhanced catalytic performance [51, 52]. Increasing the C/I ratio tends to increase the amount of Ni vacancies and Ni^{3+} ions, confirming the metal-support interactions could be enhanced at a higher C/I ratio, which is consistent with the TPR results. Figure 3. 3C and Table S5 show the concentration of Ce^{3+} tends to increase at a higher C/I ratio, which is due to the Ni doping that could reduce the oxidation state of Ce from Ce^{4+} to Ce^{3+}. The XPS results imply the amount of Ni dopped into SDC and the metallic Ni could be controlled by altering the C/I ratio, which can then modulate the metallic Ni surface area, oxygen vacancies, and metal-support interactions.

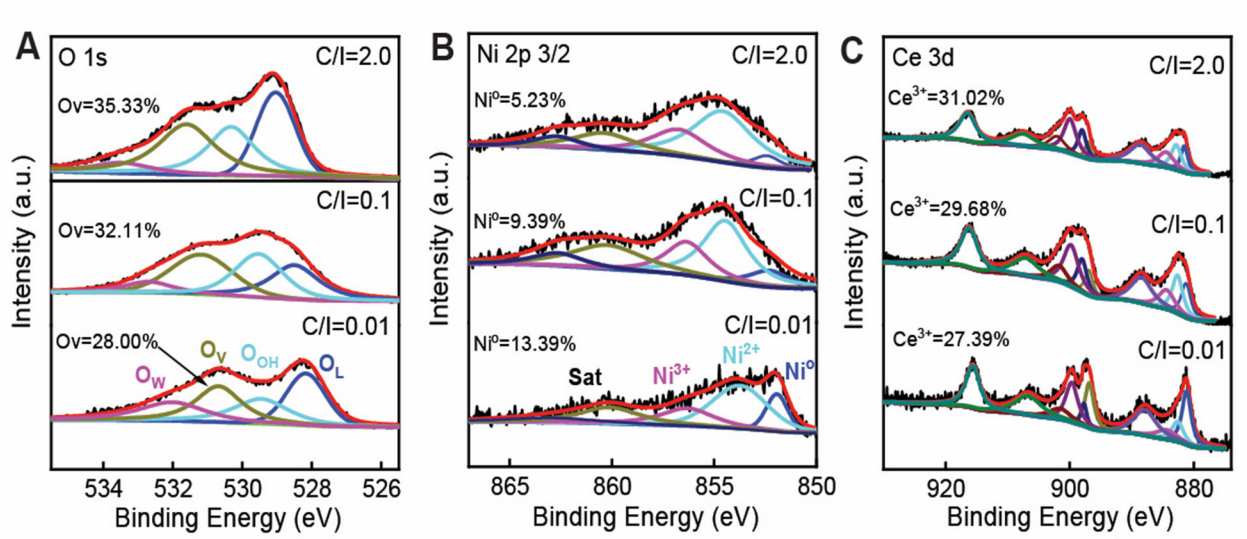

Figure 3. 3. Impacts of the C/I ratio on the electronic structure of SDC-Ni-x (x=0.01, 0.1, and 2.0). XPS spectra of the reduced SDC-Ni-*x* synthesized with different C/I ratios (0.01, 0.1, and 2.0). (A) O 1s, (B) Ni 2p3/2, (C) Ce 3d.

3.3 The interplay between the metal-support interaction and the Ni morphology

"The metal-support interactions are of great significance to high CO_2 methanation activity, which is determined by the structure of both SDC and Ni. The TEM images and corresponding particle size distribution show a C/I ratio of 2.0 leads to a smaller particle size than a C/I ratio of 0.1 (Figures 3.4A and 3.4B). Complementing the bright-field TEM images, as shown in Figures 3.4C and 3.4D, the high-angle annular dark-field scanning transmission electron microscopy (HAADF-STEM) images and corresponding energy dispersive X-ray spectroscopy (EDS) mapping show a C/I ratio of 0.1 leads to a bigger Ni particle/grain size than catalysts synthesized under a C/I ratio of 2.0 (Figures 3.4E-3.4H). This finding is in line with the XRD results (Figure 3. 2B). The high-resolution TEM (HRTEM) images shown in Figure S16 show that a C/I ratio of 2.0 gives rise to SDC with a smaller interplanar spacing than that of SDC-Ni-0.1, further affirming the fact that a high C/I ratio enhances the Ni dopped into SDC. It has been found that the SDC particle size is not significantly affected by the C/I ratio (Figure S12). Therefore, the amount of exsolved Ni nanoparticles, total metallic Ni surface area, and the metal-support interactions cooperatively determine the catalytic activities. As illustrated in Figure 3. 4I, SDC-Ni-0.01 exhibits weak metal-support interaction and has a low metallic Ni surface area, leading to poor CO_2 methanation performance. SDC-Ni-2.0 exhibits strong metal-support interaction. However, a high amount of Ni is trapped by SDC lattice and the metallic Ni surface area is also relatively low, creating less active interface and consequently low CO_2 methanation activity. The intermediate amount of C/I ratio (C/I=0.1) gives rise to relatively strong metal-support interaction while simultaneously has the highest metallic Ni surface area and largest active interface area, which contributes to the exceptional CO_2 methanation performances.

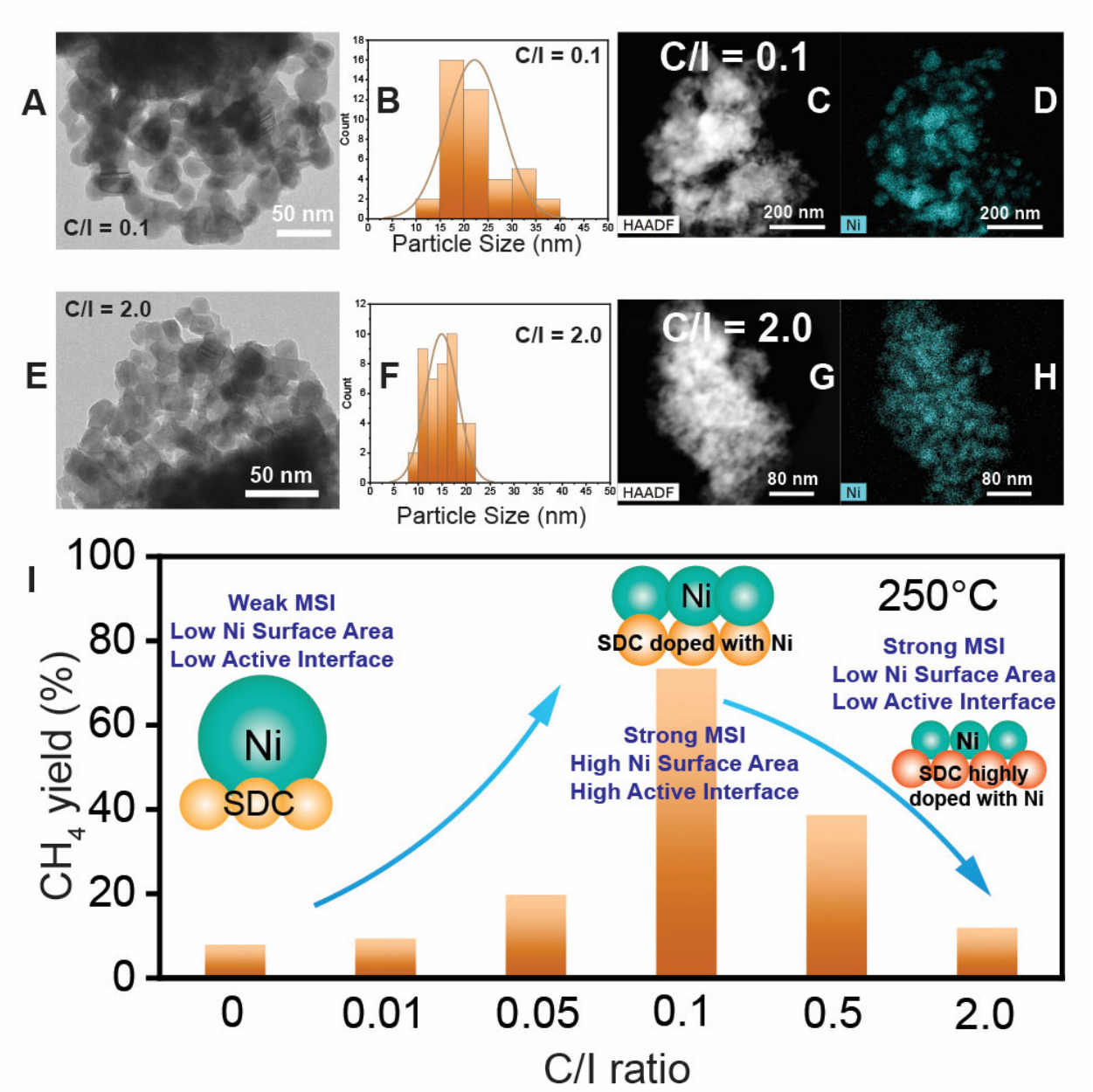

Figure 3. 4. The relationship between the C/I ratio and catalyst morphology. (A-D) Bright-field TEM image, particle size distribution, and HAADF-STEM image with EDS mapping of reduced SDC-Ni synthesized under a C/I ratio of 0.1. (E-H) Bright-field TEM image, particle size distribution, and HAADF-STEM image with EDS mapping of reduced SDC-Ni synthesized under a C/I ratio of 2.0. (I) Schematic illustration of the impacts of C/I ratio on catalytic morphology and the interplay between the metal-support interaction and Ni particle size.

2.3. In-situ operando DRIFTS to probe the CO_2 methanation kinetic of SDC-Ni-x

To better understand how the C/I ratio could significantly impact the catalytic performances, comprehensive in-situ operando DRIFTS measurements were conducted to probe the intermediate species and identify the CO_2 methanation pathways. Time-resolved DRIFT spectra were recorded upon changing the atmosphere of the high-temperature reaction chamber, identifying the reactive-adsorbed species and their corresponding roles in catalytic reactions.

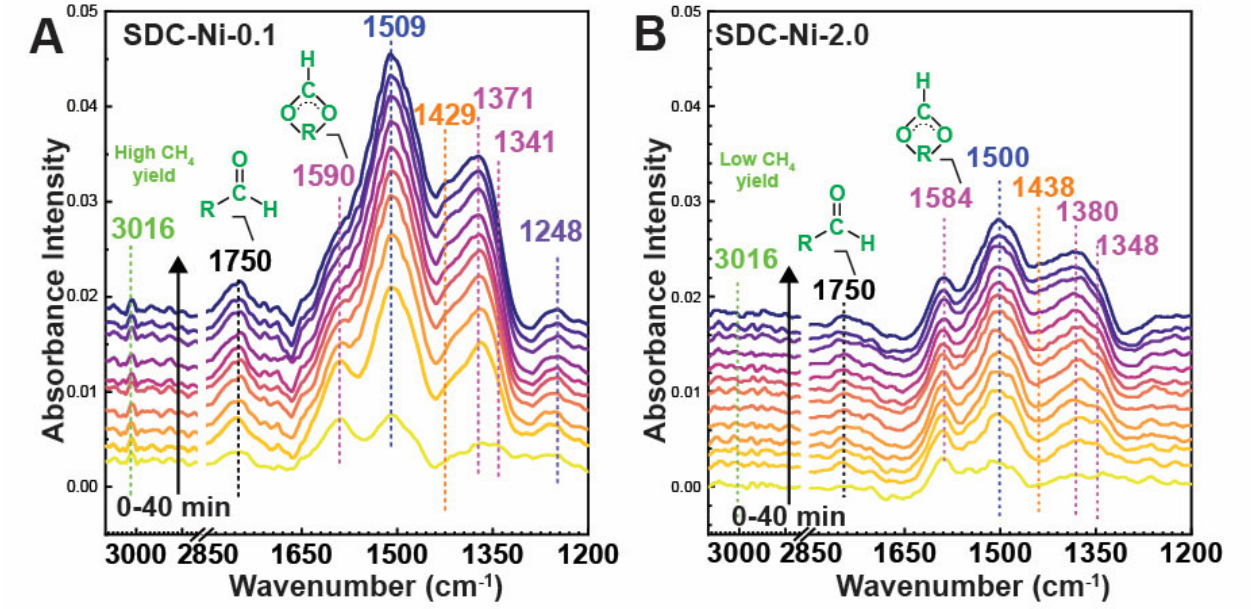

Figure 3. 5. Time-resolved DRIFT spectra of CO2 methanation over (A) SDC-Ni-0.1. (B) and SDC-Ni-2.0. The spectra were collected when the feed gas was switched from 100 sccm UHP Ar to 11 sccm CO_2, 44 sccm H_2, and 45 sccm UHP Ar at 250 °C.

Figure 3. 5 presents the operando DRIFT spectra of CO_2 methanation over SDC-Ni-0.1 and Ni-SDC-2.0 at 250 °C. The evolution key species' infrared (IR) signals were recorded after switching the gas from ultra-high purity (UHP) Ar to 11 sccm CO_2, 44 sccm H_2 and 45 sccm Ar. Some IR bands gradually grow while some bands vanish, enabling probing of the active species involved in CO_2 methanation. The CH_4 (3016 cm^{-1}) detected over SDC-Ni-2.0 is not as obvious as the CH_4 formed over SDC-Ni-0.1, which is consistent with the packed bed reactor testing (Figure 3. 1A). No detectable CO peaks were found from both catalysts (Figure S17), indicating they are highly selective for CH_4 production. As shown in Figure 3. 5, after switching the gas, the intensity of bands belonging to monodentate carbonate (~1500 cm^{-1}, ~1370 cm^{-1}), bidentate formate (~1588 cm^{-1}, 1300-1340 cm^{-1}), bicarbonate (~1430 cm^{-1}, ~1646 cm^{-1}), formyl (~1750 cm^{-1}), and carboxylate (~1248 cm^{-1}) tend to change, suggesting CO_2 methanation embraces those species[8, 53-56]. After ~40 minutes of treatment, the concentration of these species achieves equilibrium. At 250 °C, bidentate formate species (~1588 cm^{-1}) over Ni-SDC-0.1 quickly vanish while the concentration of formyl (~1750 cm^{-1}) simultaneously increases, suggesting that formate species could readily decompose to formyl. Formyl could then be hydrogenated to methoxy and subsequently CH_4 [57]. Nevertheless, the IR signals of formyl over SDC-Ni-2.0 are not significant while the bands belonging to formate are strong. Therefore, the formate species are not prone to decompose over SDC-Ni-2.0 and the subsequent hydrogeneration of formyl to CH_4 is ceased, leading to low CH_4 yield. C-O bond cleavage is the crucial step during the formate-to-formyl process, and thus activation energy of C-O bond cleavage over SDC-Ni-0.1 is lower than SDC-Ni-2.0. Moreover, upon changing the atmosphere, the IR signals of monodentate carbonate emerge and grow, suggesting the monodentate carbonate species could be one of the reactive-adsorbed species.

To confirm formate and formyl are the key species during CO_2 methanation and better understand the uniqueness of SDC-Ni-0.1, formic acid was used as the reactant[58]. Upon exposure to formic acid (Figure S18), multiple IR bands readily develop, which can be assigned as the gaseous formic acid and intermediate species on the catalyst. After changing the gas from diluted formic acid to Ar (Figure 6A and 6B), we focus on studying the kinetic of formate decomposition. The formate can decompose or be converted over SDC-Ni-0.1 with a much faster speed than that over SDC-Ni-2.0. After treatment under Ar for 40 minutes, there are no obvious signs of formate groups over SDC-Ni-0.1. However, the formate species remain on SDC-Ni-2.0 upon outgassing the sample. This observation is consistent with the conclusion made during CO_2 methanation, confirming that C-O bond cleavage and formate decomposition kinetics over SDC-Ni-0.1 is much faster than that over SDC-Ni-2.0. Therefore, SDC-Ni-0.1 leads to higher CO_2 methanation activity.

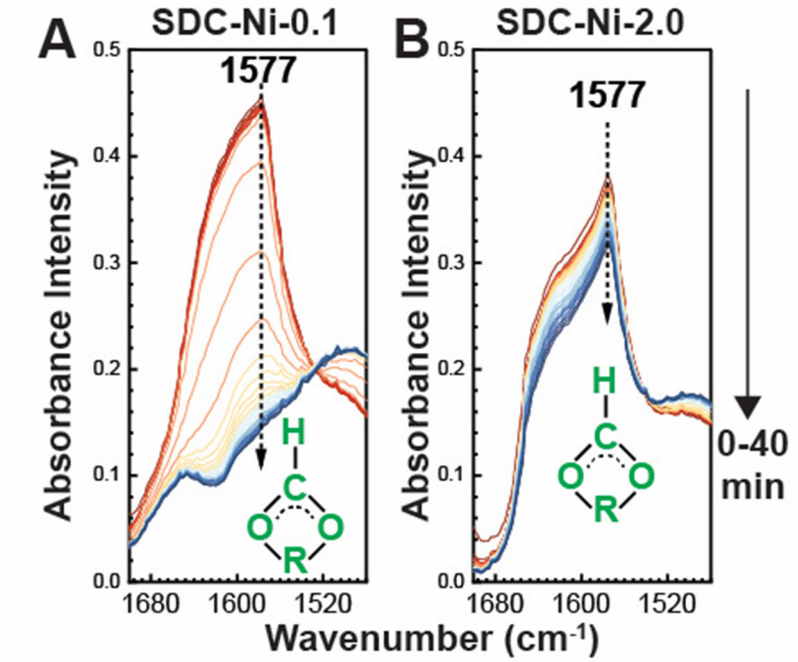

Figure 3. 6. Evolution of DRIFT spectra collected at 250 °C over SDC-Ni-0.1(A) and SDC-Ni-2.0 (B). Both catalysts were pre-treated under a mixture of Ar with HCOOH for 1 hour. The spectra were collected after the atmosphere was changed from the mixture of Ar with HCOOH to UHP Ar.

To further strengthen the conclusion that CH_4 is produced via the formate pathway and better understand how SDC-Ni-0.1 leads to enhanced catalytic performances, the gas composition was then switched from Ar to 20% H_2 balanced with Ar, providing H_2 for hydrogenating adsorbed species on the catalysts. The resulting spectra over both catalysts are shown in Figures 3.7A–3.7D. As the hydrogenation is resumed, the intensity of carbonate, hydroxyl, and bicarbonate species gradually decreases (Figure S18). The residue and low-concentration formate species over SDC-Ni-0.1 can quickly decompose and form formyl species which are subsequently hydrogenated to CH_4 (Figure 3.7B). CH_4 can be produced over SDC-Ni-0.1 that is originated from the formate species, reinforcing the formate pathway established in this work. Furthermore, no methoxy was

observed while CH_4 could be produced, suggesting the second C-O cleavage and methoxy-to-methane process over SDC-Ni-0.1 are fast. After ~4 minutes of treatment under H_2, the formate species over SDC-Ni-0.1 are fully converted while the formate over SDC-Ni-2.0 is still evident after 40 minutes. Moreover, although methoxy (2920 cm^{-1}) is observed on SDC-Ni-2.0, methane is not produced, which indicates that C-O cleavage is sluggish during the hydrogenation of methoxy to methane over SDC-Ni-2.0.

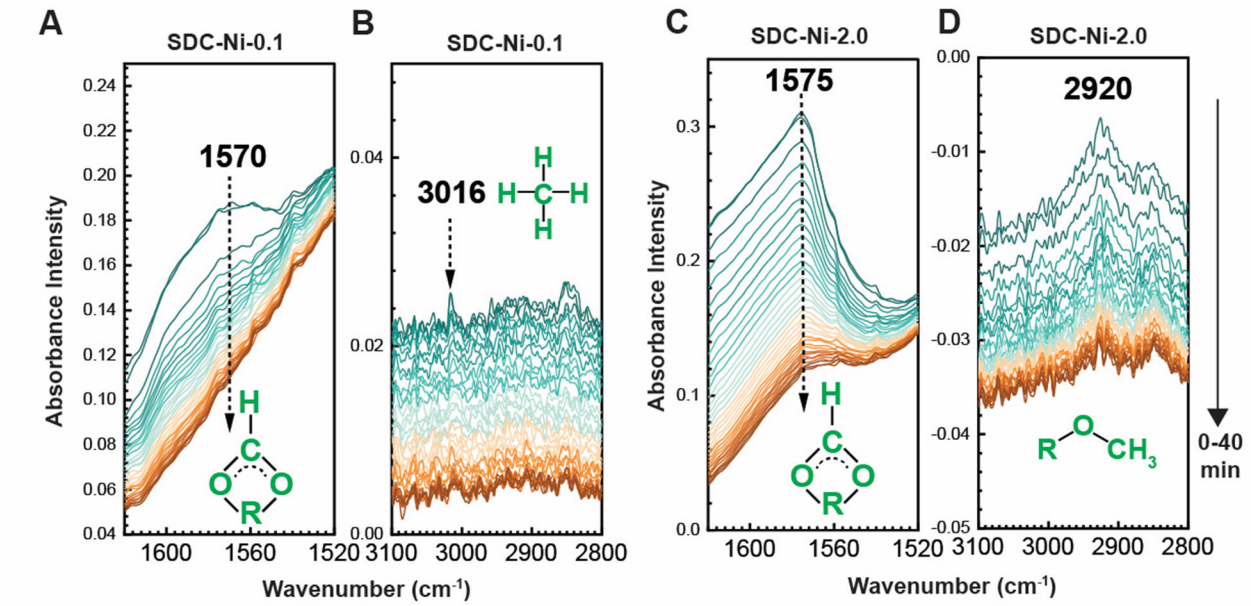

Figure 3. 7. Evolution of DRIFT spectra collected at 250 °C over SDC-Ni-0.1(A-B) and SDC-Ni-2.0 (C-D). Both catalysts were pre-treated under a mixture of Ar with HCOOH for 1 hour followed by the degassing under UHP Ar for 1 hour. The spectra were collected after the atmosphere was changed from Ar to 20% H2 balanced with Ar.

Figure 3. 8A displays the proposed CO_2 methanation mechanism over SDC-Ni catalysts, which follows the formate-formyl-methoxy pathway. The C/I ratio does not affect the CO_2 methanation pathway while it impacts the kinetics of intermediate steps. The C-O bond cleavage is the foremost step of formate decomposition to formyl and subsequent methoxy to methane. CO_2 methanation over SDC-Ni therefore involves two kinds of C-O bond cleavage, the rates of which determine the overall CH_4 yields. Both formate decomposition and methoxy-to-methane process need hydrogen to accomplish C-O bond cleavage. The amount of Ni surface sites could determine the available of chemisorbed hydrogen. As shown in Figure 3. 8B, SDC-Ni-0.1 has higher metallic Ni surface and larger active interface than that of SDC-Ni-2.0; thus, the C-O bond cleavage during the steps of formate to formyl and methoxy to methane are faster over SDC-Ni-0.1 than SDC-Ni-2.0. Therefore, the CH_4 yield over SDC-Ni-0.1 is much higher than that over SDC-Ni-2.0.

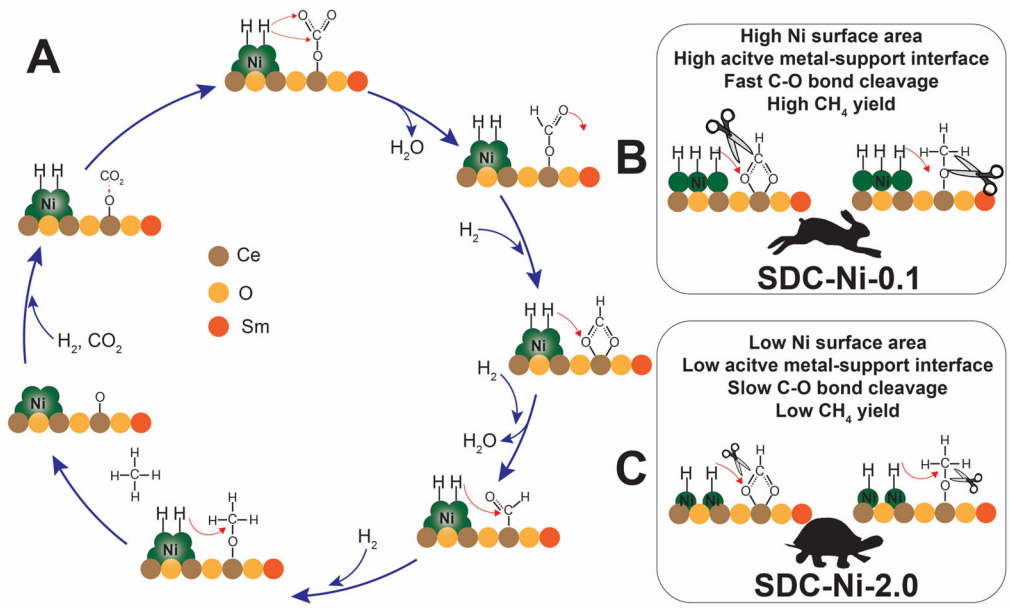

Figure 3. 7. (A) Proposed mechanism of CO2 methanation over SDC-Ni catalysts. (B) The C-O bond cleavage over SDC-Ni-0.1 during formate-to-formyl process and methoxy-to-methane process is fast. (C) The C-O bond cleavage over SDC-Ni-2.0 during formate-to-formyl process and methoxy-to-methane process is sluggish.

Schematic illustration of the one-pot wet-chemistry method (Figure S1); XRD patterns and Rietveld refinement of catalysts (Figure S2 and S3, Table S1 and S2); CH_4 yield comparisons (Figure S4) ; TOF (Figure S5) and selectivity (Figure S6), TPR (Figure S11), grain size (Figure S12), Ni doping amount (Figure 3. 14), lattice constant (Figure S15), BET (Table S3) and XPS (Table S5) of SDC-Ni-*x*; CH_4 yield of CeO_2-Ni catalysts (Figure S7); CH_4 selectivity of SDC-Ni-0.1 at different H_2/CO_2 ratio (Figure S8); Long-term stability (Figure S9), SEM images (Figure S10) and TEM (Figure S16) of SDC-Ni-0.1; TPR comparison of SDC-Ni-0.1 and IM (Figure S13); DRITF of SDC-Ni-0.1 and 2.0 (Figure S17-S18); Performance comparisons of CO_2 methanation catalysts (Table S4).

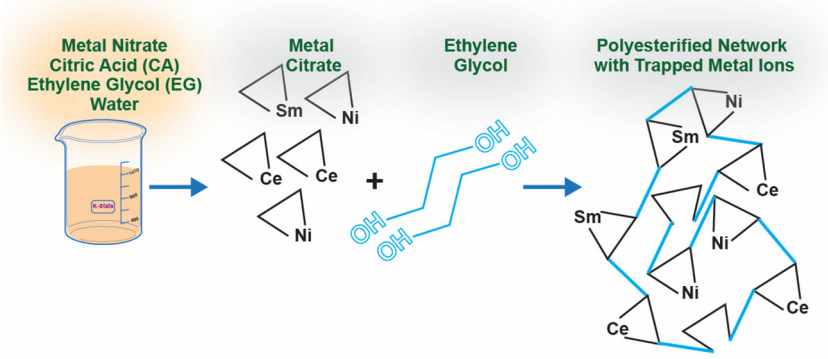

Figure S1. Schematic illustration of the one-pot wet-chemistry method employed for synthesizing SDC-Ni catalysts.

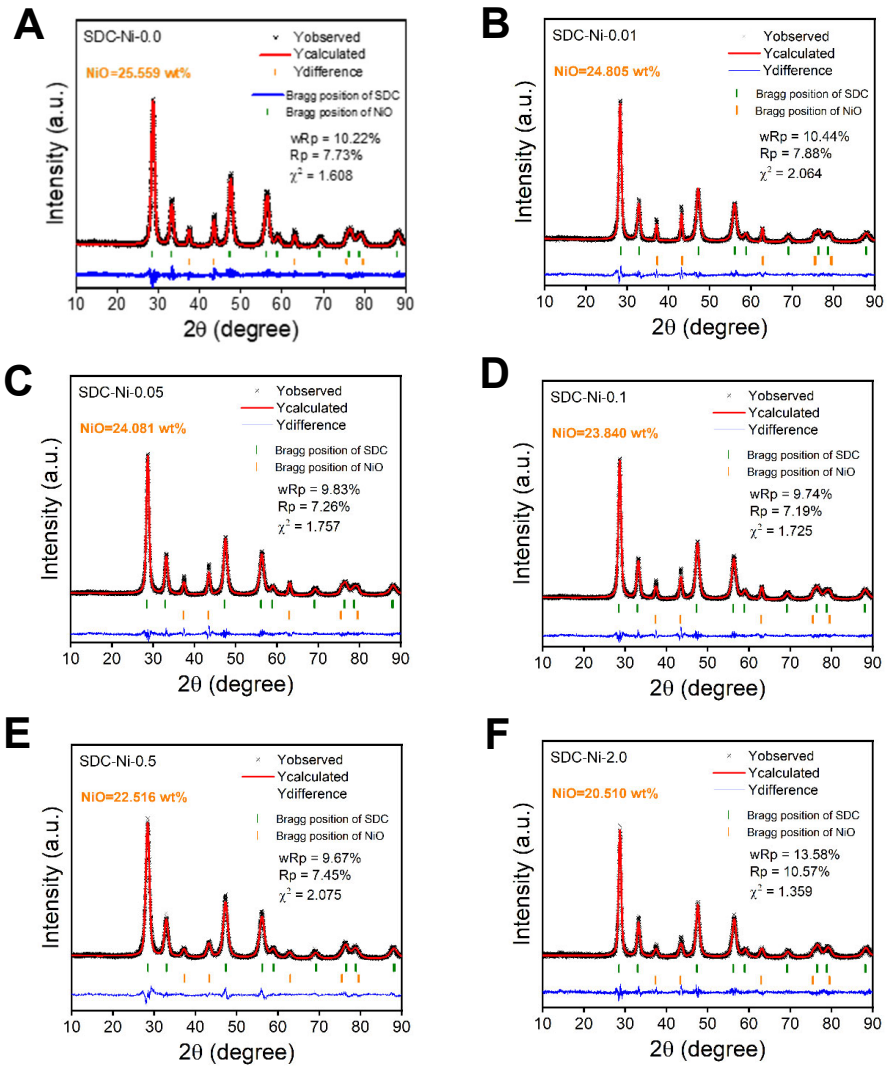

Figure S2. XRD patterns and Rietveld refinement of as fired SDC-Ni with various C/I ratios. (A) 0.0, (B) 0.01, (C) 0.05, (D) 0.1, (E) 0.5, (F) 2.0.

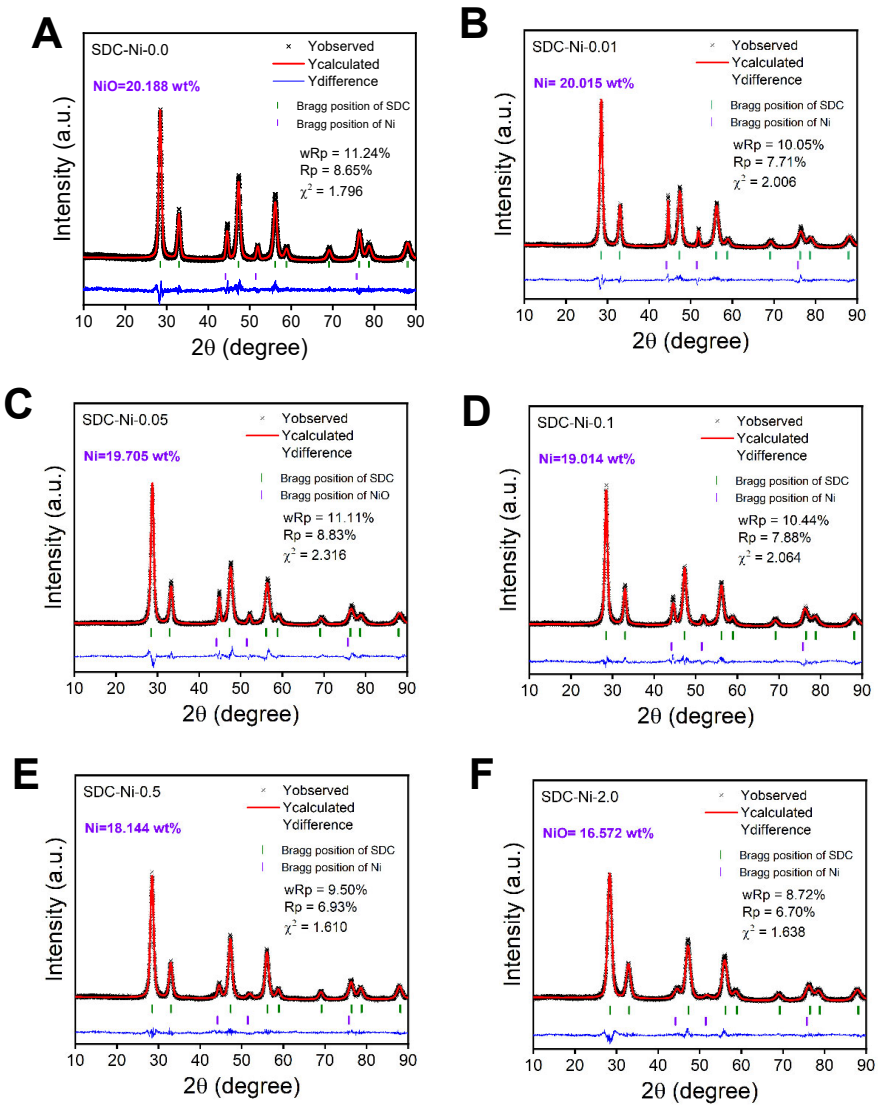

Figure S3. XRD patterns and Rietveld refinement of reduced SDC-Ni with various C/I ratios. (A) 0.0, (B) 0.01, (C) 0.05, (D) 0.1, (E) 0.5, (F) 2.0.

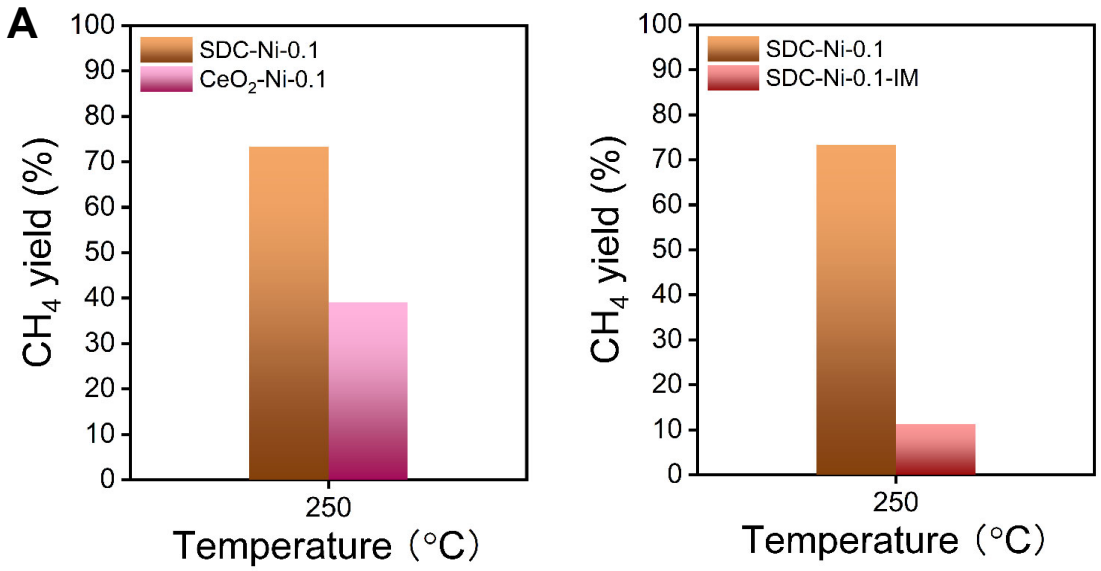

Figure S4. Comparison the CH_4 yield of SDC-Ni-0.1 with (A) CeO_2-Ni-0.1 and (B) SDC-Ni-IM. Testing temperature is at 250 °C with H_2/CO_2=4:1 at a flow rate of 20 sccm. The weight of each catalyst is 0.1g.

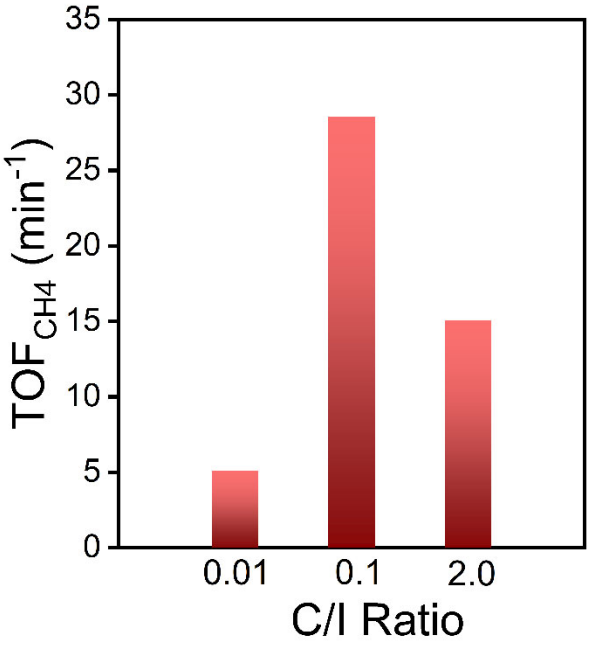

Figure S5. TOF of SDC-Ni-*x* catalysts with C/I ratios of 0.01, 0.1 and 2.0 at 250 °C

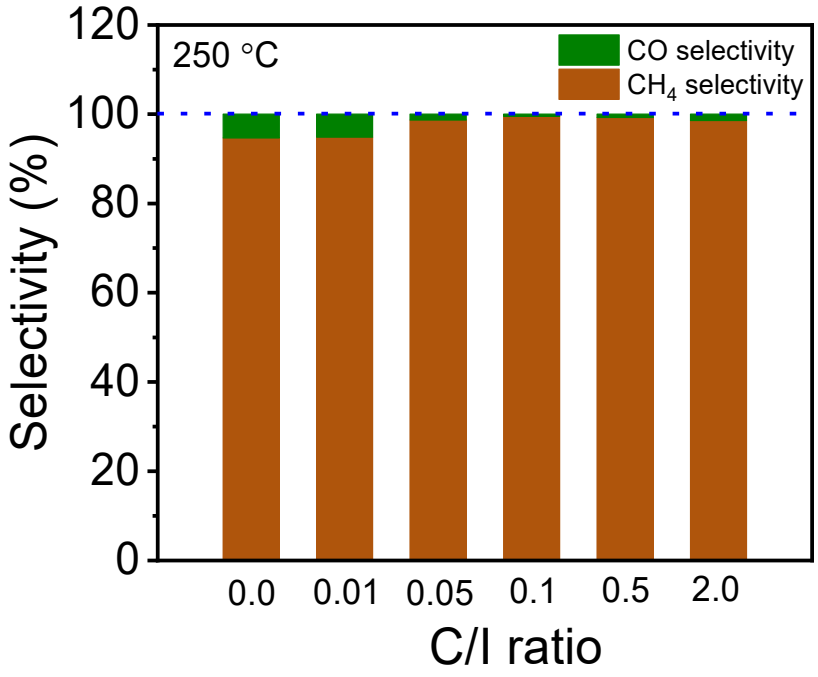

Figure S6. CH_4 and CO selectivity of SDC-Ni-*x* catalysts with various C/I ratios at 250 °C. All catalysts are tested under H_2/CO_2=4:1 at a flow rate of 20 sccm. The amount of loaded catalyst is 0.1g.

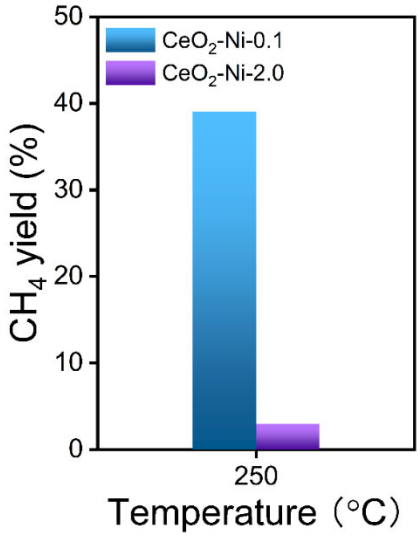

Figure S7. CH_4 yield of CeO_2-Ni-0.1 and CeO_2-Ni-2.0 at 250 °C with H_2/CO_2=4:1 at a flow rate of 20 sccm. The weight of each catalyst is 0.1g.

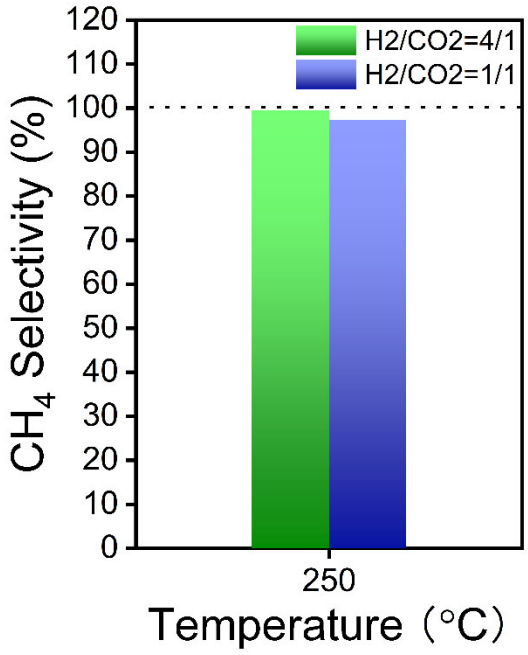

Figure S8. CH_4 selectivity of SDC-Ni-0.1 at 250 °C. SDC-Ni-0.1 was tested under H_2/CO_2=4/1 and H_2/CO_2=1/1 at a flow rate of 20 sccm. The amount of SDC-Ni-0.1 is 0.1g.

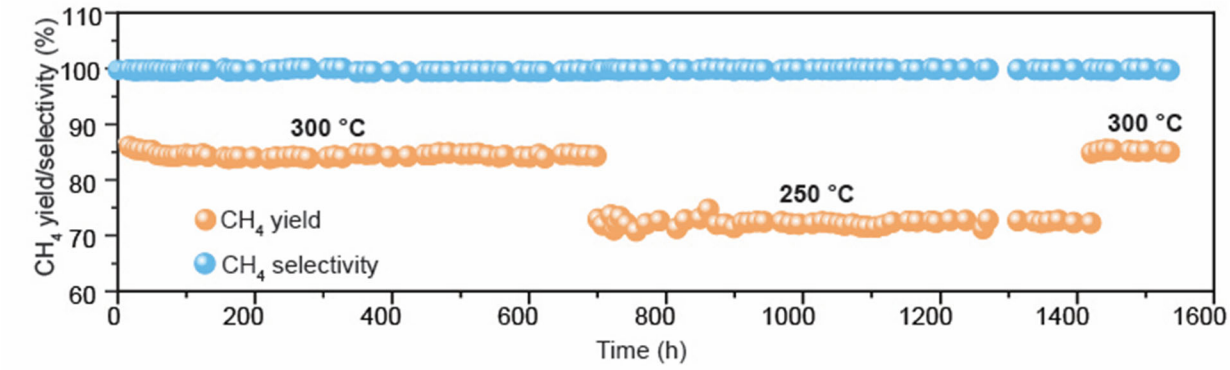

Figure S9. Long-term stability testing of CO_2 methanation over SDC-Ni-0.1 at 300 °C and 250 °C with H_2/CO_2=4:1 at a flow rate of 20 sccm. The weight of the catalyst is 0.1g.

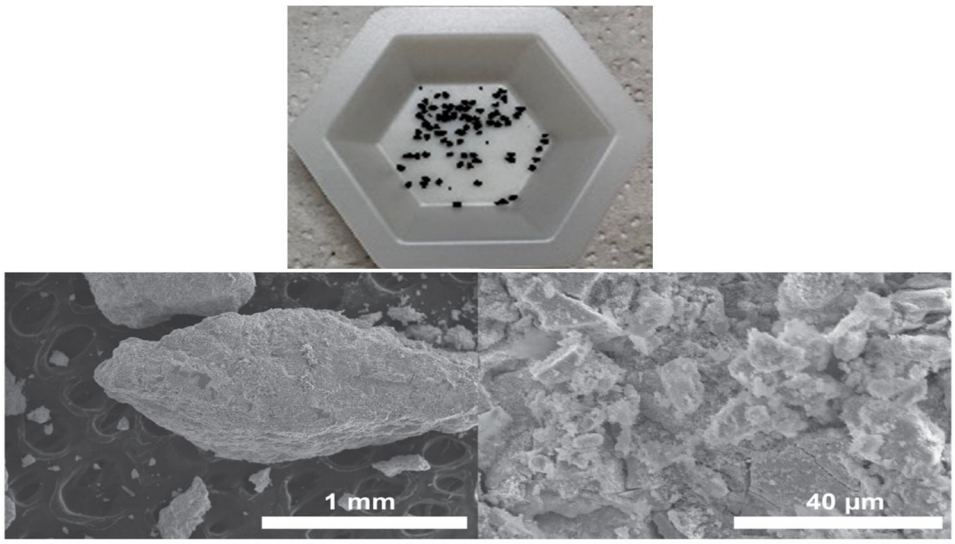

Figure S10. Photo and SEM images of SDC-Ni-0.1 after long-term testing.

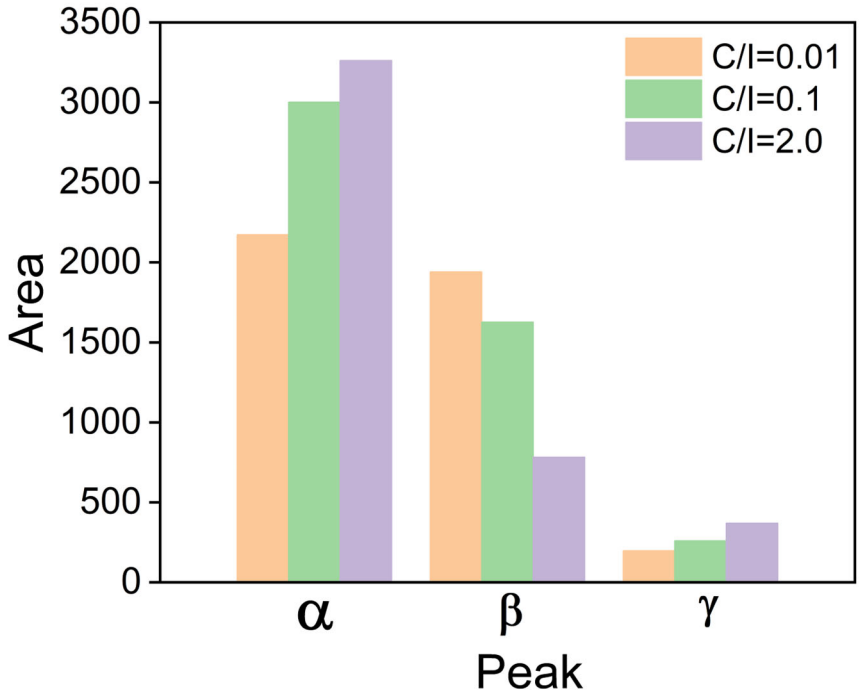

Figure S11. TPR deconvolution results of SDC-Ni-*x* catalysts with C/I ratios of 0.01, 0.1 and 2.0.

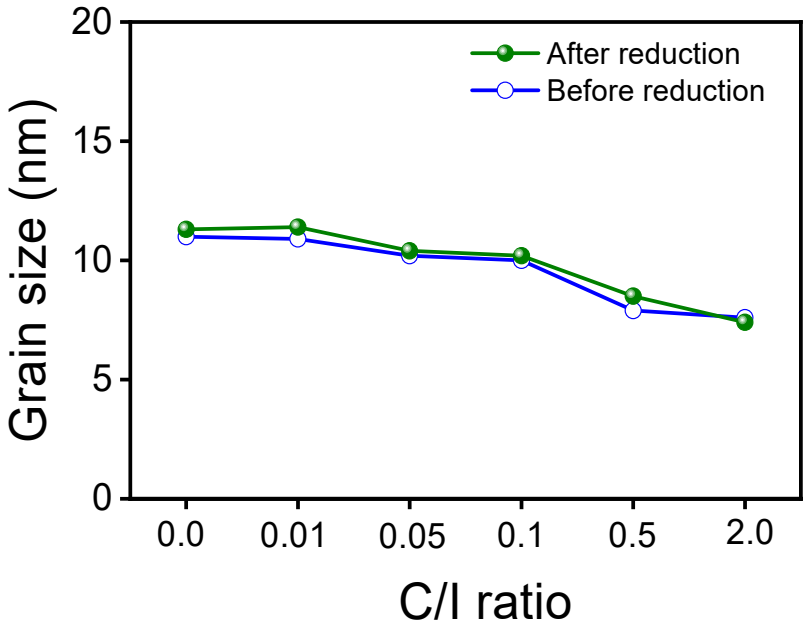

Figure S12. The grain size of SDC as a function of C/I ratio.

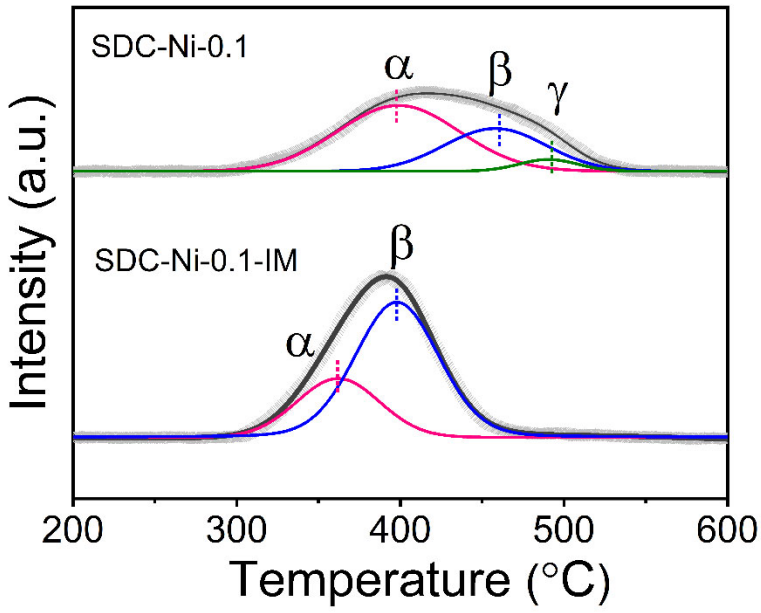

Figure S13. The H_2-TPR profiles of SDC-Ni-0.1-IM and SDC-Ni-0.1.

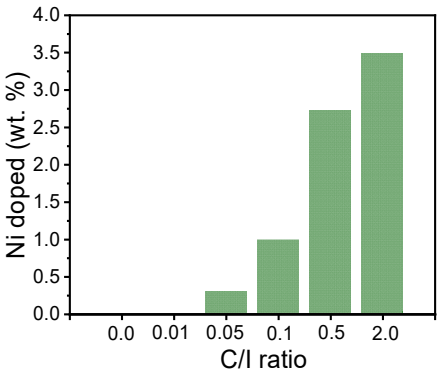

Figure S14. The amount of Ni incorporated into SDC lattice as a function of C/I ratio.

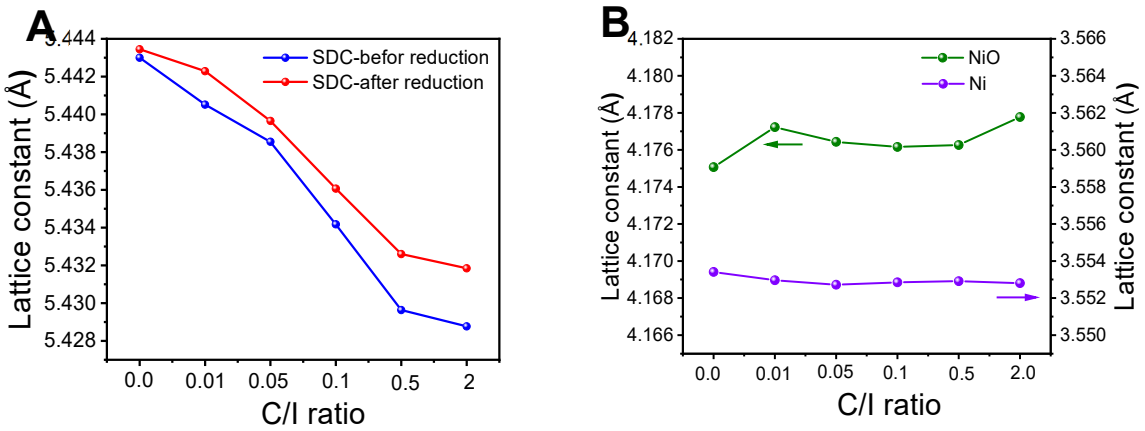

Figure S15. The lattice parameters as a function of C/I ratios. (A) SDC, (B) NiO and Ni.

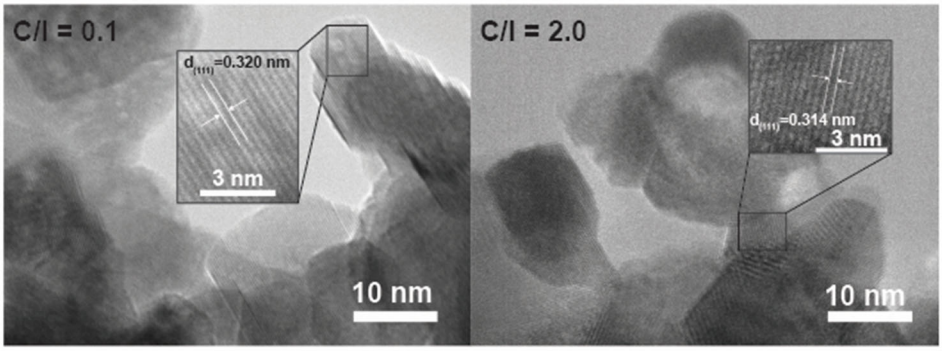

Figure S16. High-resolution TEM image of reduced SDC-Ni synthesized under a C/I ratio of 0.1.

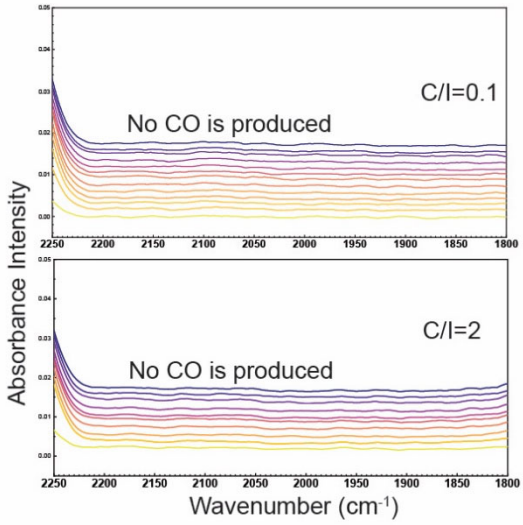

Figure S17 Time-resolved DRIFT spectra of CO2 methanation over (A) SDC-Ni-0.1. (B) and SDC-Ni-2.0. The spectra were collected when the feed gas was switched from 100 sccm UHP Ar to 11 sccm CO_2, 44 sccm H_2, and 45 sccm UHP Ar at 250 °C.

Table S1. The XRD Rietveld refinement results of SDC-Ni at C/I=0.0, 0.01, 0.05. 0.1. 0.5 and 2.0 before reduction

Sample	Phase	a=b=c (Å)	α=β=γ (°)	*NiO (%)*	χ^2	$_wR_p$ (%)	R_p (%)
SDC-Ni-0.0	SDC-0.0	5.4430	90	25.559	1.608	10.22	7.73
	NiO	4.1751	90				
SDC-Ni-0.01	SDC-0.01	5.4405	90	24.805	1.994	9.92	7.52
	NiO	4.1772	90				
SDC-Ni-0.05	SDC-0.05	5.4385	90	24.081	1.757	9.83	7.26
	NiO	4.1764	90				
SDC-Ni-0.1	SDC-0.1	5.4342	90	23.840	1.725	9.74	7.19
	NiO	4.1762	90				
SDC-Ni-0.5	SDC-0.5	5.4296	90	22.516	2.075	9.67	7.45
	NiO	4.1763	90				
SDC-Ni-2.0	SDC-2.0	5.4287	90	20.510	1.359	13.58	10.57
	NiO	4.1778	90				

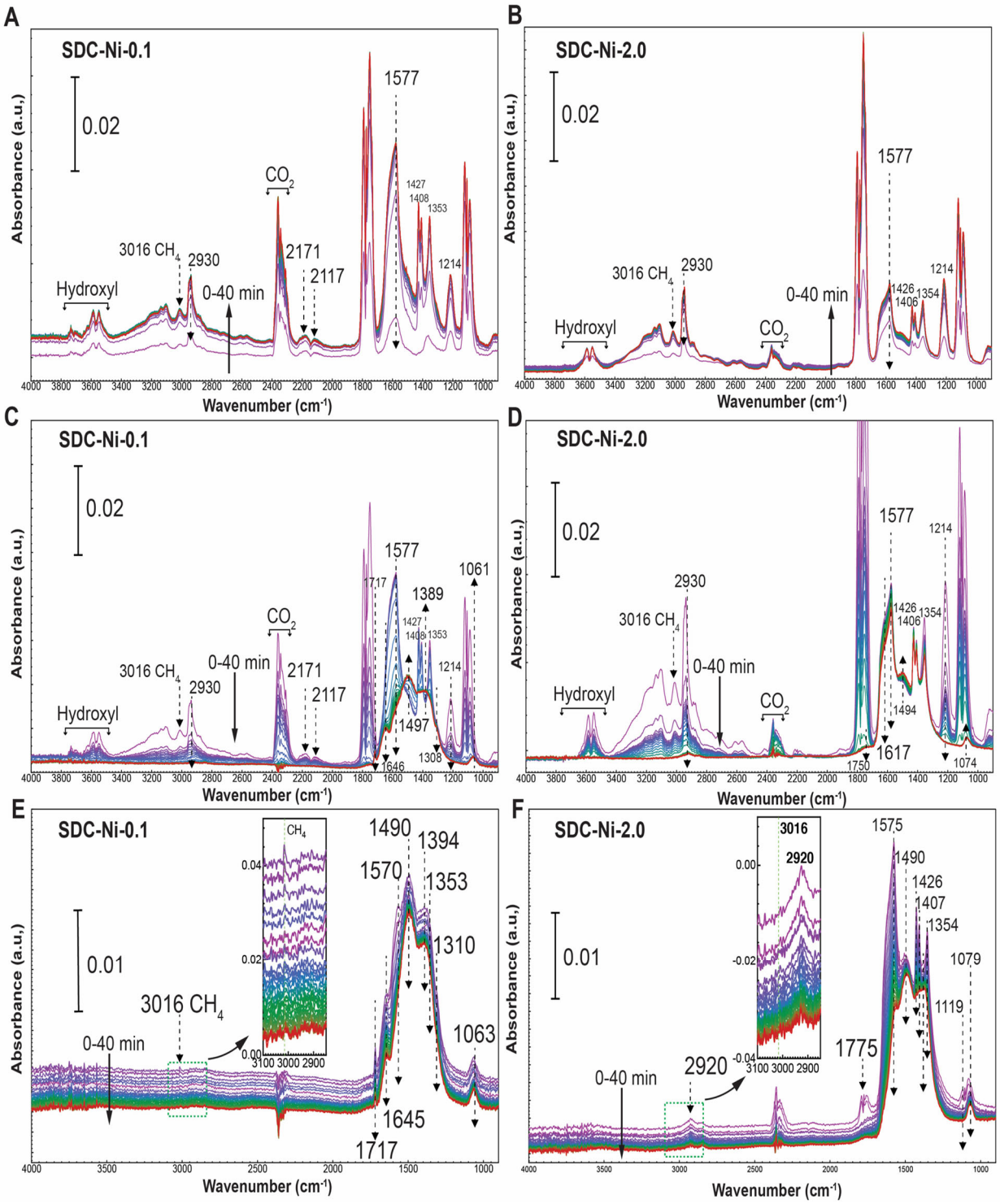

Figure S18 – Evolution of DRIFT spectra collected at 250 °C over SDC-Ni-0.1 and SDC-Ni-2.0 (A) (B) The feed gas was switched from Ar to Ar with HCOOH. (C) (D). The feed gas was changed back to UHP Ar. (E) (F). The atmosphere was changed from Ar to 20% H_2 balanced with Ar.

Table S2. The XRD Rietveld refinement results of SDC-Ni at C/I=0.0, 0.01, 0.05. 0.1. 0.5 and 2.0 after reduction

Sample	Phase	a=b=c (Å)	α=β=γ (°)	*Ni (%)*	χ^2	$_{w}R_p$ (%)	R_p (%)
SDC-Ni-0.0	SDC-0.01	5.4434	90	20.081	1.796	11.24	8.65
	Ni	3.5534	90				
SDC-Ni-0.01	SDC-0.01	5.4423	90	20.015	2.006	10.05	7.71
	Ni	3.5530	90				
SDC-Ni-0.05	SDC-0.05	5.4396	90	19.705	2.361	11.11	8.83
	Ni	3.5527	90				
SDC-Ni-0.1	SDC-0.1	5.4361	90	19.014	2.064	10.44	7.88
	Ni	3.5529	90				
SDC-Ni-0.5	SDC-0.5	5.4326	90	18.144	1.610	9.50	6.93
	Ni	3.5530	90				
SDC-Ni-2.0	SDC-2.0	5.4318	90	16.572	1.638	8.72	6.70
	Ni	3.5528	90				

Table S3 BET surface area of SDC-Ni catalysts with different C/I ratios before reduction

Catalyst	BET surface area (m^2/g)
SDC-Ni-0.01	16.11
SDC-Ni-0.1	24.96
SDC-Ni-2.0	30.57

3.4. Protonic ceramic fuel cells for the dry reforming of methane (DRM-PCFCs)

Figure 3. 1A displays the scenario for implementing DRM-PCFCs, which function as fuel cells that intensify DRM with electrochemical power generation. The generated power can be utilized by some energy sectors; thus, DRM-PCFCs can serve as decentralized power sources. The produced syngas or hydrogen can also be converted to value-added chemicals by chemical manufacturers. The intrinsic performance of pristine PCFCs and DRM catalysts is essential for achieving high power density. As shown in Figure 3. 8B, to minimize the overpotential ascribed to the oxygen reduction reaction, a newly developed composite cathode ($BaCo_{0.4}Fe_{0.4}Zr_{0.1}Y_{0.1}O_{3-\delta}$ + $BaCe_{0.7}Zr_{0.1}Y_{0.1}Yb_{0.1}O_{3-\delta}\delta$) was employed 33. Additionally, a PCFC electrolyte was fabricated via ultrasonic spray coating (Figure S2) to reduce its thickness to ~6 μm (Figure 3. 8B), which reduced ohmic resistance. $BaZr_{0.8}Y_{0.2}O_{3-\delta}$ (BZY20) + Ni was used as the anode. A DRM catalyst developed in this work, SDC-Ni-Ru, was employed as an effective catalytic layer on the anode (Figure 3. 8B inserted figure). As shown in Figure 3. 8C, without the DRM catalyst, the PCFC performance was poor due to the low catalytic activity of BZY20+Ni for DRM, which generates low amounts of hydrogen for power generation. The DRM catalyst developed in this work led to an ~ 2.5-fold increase in the PCFC performance at 650 °C (Figure 3. 8C). Compared with literature results (Table S1), unprecedented performance for power generation was obtained. For example,

at 650 °C, the PCFCs yield a peak power density of 0.94 W cm^{-2} using a mixture of CH_4 and CO_2 as the fuel, which doubles the performance of state-of-the-art PCFCs (Figure 3. 8D). Moreover, the intermediate-temperature (550-650 °C) DRM-PCFCs achieved higher performance than high-temperature (700-850 °C) DRM-SOFCs, indicating the DRM catalyst developed in this work exhibits outstanding catalytic activity at reduced operating temperatures (Table S2).

3.5.Rationally designed DRM catalyst with enhanced catalytic activity and coking tolerance

The DRM catalysts were synthesized via a one-pot wet-chemistry method and subsequent *in situ* exsolution. Three catalysts were synthesized and studied in this work: $Sm_{0.2}Ce_{0.7}Ni_{0.15}O_{2-\delta}$ (SDC-Ni), $Sm_{0.2}Ce_{0.7}Ru_{0.15}O_{2-\delta}$ (SDC-Ru), and $Sm_{0.2}Ce_{0.7}Ni_{0.1}Ru_{0.05}O_{2-\delta}$ (SDC-Ni-Ru). As shown in Figure S3, the X-ray diffraction (XRD) patterns of the as-synthesized catalysts show that SDC-Ni consists of Ni-doped SDC, which exhibits a cubic fluorite structure and a small amount of NiO, indicating that the solubility of Ni in SDC is lower than 15 mol%. SDC-Ru is composed of Ru-doped SDC and RuO_2. However, the XRD pattern of as-synthesized SDC-Ni-Ru does not show noticeable peaks indexed to either NiO or RuO_2, implying that most of the Ni and Ru is dissolved in the SDC lattice, which could be beneficial for the creation of more metallic clusters/nanoparticles during subsequent *in situ* exsolution under a reducing atmosphere.

After reduction, as shown in Figures 3.9A-C, the catalysts are reduced to SDC-supported monometallic/bimetallic clusters/nanoparticles. The reduced SDC-Ni comprises SDC and metallic Ni, while SDC-Ru contains SDC and metallic Ru. The XRD pattern for reduced SDC-Ni-Ru shows peaks associated with metallic Ni. We hypothesized that Ru also exsolves from the SDC lattice. However, the intensity of the Ru peaks is small and might have arisen from an extremely small amount of metallic Ru. As shown in Figure 3. 9C and Table S3, XRD Rietveld refinement was conducted to analyze the XRD pattern of reduced SDC-Ni-Ru. The reduced SDC-Ni-Ru comprises three phases: SDC, metallic Ni, and metallic Ru. The amounts of metallic Ni and Ru are calculated as 3.0 wt.% and 2.7 wt.%, respectively, slightly lower than the maximum amounts (3.4 wt.% for Ni and 2.9 wt.% for Ru), indicating that small amounts of Ni and Ru remain in the SDC lattice. Therefore, the reduced SDC-Ni-Ru is composed of Ni and Ru-doped SDC, metallic Ni, and metallic Ru.

H_2-temperature programmed reduction (H_2-TPR) (Figure 3. 9D) and TEM analysis (Figures 3.9E-F) were performed to study the exsolution, microstructure, and chemical composition of the reduced catalysts. The H_2-TPR profiles shown in Figure 3. 9C present the nature of Ni and/or Ru in these catalysts and also allows for investigations of the interactions between the metallic phase and the SDC support 34. The reduction temperature, at which the H_2-TPR profile peaks, indicates the degree of interaction of the metallic phase with the oxide support 35. A relatively high reduction temperature indicates that the metallic phase strongly interacts with the oxide support 16. Typically, the *in situ* exsolution of Ni from the oxide support requires a higher reduction temperature than that needed to reduce bulk NiO particles, suggesting that *in situ* exsolved Ni has stronger interactions with the oxide support than interactions between bulk Ni particles and the oxide support. The H_2-TPR profile of SDC-Ni displays two overlapping peaks at approximately 265 °C and 356 °C, which could correspond to the reduction of bulk NiO particles (area c) and *in*

situ exsolution of Ni (area d), respectively. The H_2-TPR profile SDC-Ru also shows two overlapping peaks with peak temperatures of 95 °C and 145 °C, which correspond to the reduction of bulk RuO_2 particles (area a) and *in situ* exsolution of Ru (area b). These H_2-TPR profiles are consistent with the XRD results. The as-synthesized SDC-Ni is composed of Ni-doped SDC and NiO, while SDC-Ru consists of Ru-doped SDC and RuO_2. Additionally, the H_2-TPR profile of SDC-Ni-Ru presents two main peaks at 143 °C and 330 °C, which are close to the temperature required to exsolve Ni and Ru from the SDC lattice, suggesting that the low-temperature peak (area b) is related to the exsolution of Ru. The high-temperature peak (area d) corresponds to the exsolution of Ni. Prior to the peak assigned to the exsolution of Ni, the H_2-TPR profile of SDC-Ni-Ru shows the reduction of small amounts of bulk NiO particles, implying that NiO is not fully dissolved in the SDC lattice and a minor amount of NiO exhibits as bulk NiO particles. Additionally, the peak corresponding to the Ni cluster of the SDC-Ni-Ru sample shifts to a lower temperature compared to that of SDC-Ni, indicating that the active H species adsorbed on the pre-reduced Ru^o sites could readily spillover to the neighboring Ni species in SDC lattice, and consequently promoting the exsolution of Ni from SDC bulk 36; 37. Therefore, the reducibility of the SDC-Ni-Ru catalyst is enhanced, compared to the Ru-free SDC-Ni catalyst. Moreover, the presence of Ru can closely interact with NiO species, resulting in a high dispersion on the SDC-Ni-Ru sample, which might also lead to the Ni exsolution at a relatively low temperature 38.The peak associated with the reduction of bulk RuO_2 is not clear, indicating that Ru is almost fully dissolved in the SDC lattice, which is also consistent with the XRD results. Although the XRD pattern for reduced SDC-Ni-Ru does not clearly display the peaks corresponding to Ru, the H_2-TPR profiles and XRD Rietveld refinement results suggest that Ru clusters/nanoparticles can also be created on SDC via *in situ* exsolution upon reduction.

The synergistic effect between Ni and Ru is significant for improving DRM activity. To identify the structure of *in situ* exsolved Ni and Ru, energy-dispersive X-ray spectroscopy (EDS) mapping and high-resolution transmission electron microscopy (HR-TEM) images are shown in Figures 3.9E-F. In the figures, all the constituent elements of the oxide support (Sm, Ce, and O) are uniformly distributed. Ni exhibits two structures, including Ni nanoparticles and Ni clusters. The Ni nanoparticle shown in Figure 3. 9D is attributed to the reduction of relatively large bulk NiO particles, while the Ni clusters are exsolved from the SDC lattice. The Ni clusters are homogeneously dispersed on the SDC. Additionally, the EDS mapping shows that Ru is uniformly distributed, and no Ru nanoparticles are observed, indicating that metallic Ru only exists as Ru clusters. These EDS mapping images are consistent with the XRD results and H_2-TPR profiles. The HR-TEM image (Figure 3. 9F) shows a lattice plane with a d-spacing of 0.317 nm, corresponding to the SDC (111) plane, which matches well with the XRD Rietveld refinement results (0.315 nm).

The surface electronic structure of the reduced DRM catalysts was investigated using X-ray photoelectron spectroscopy (XPS) (Figures 3.9G-J and Table S4). To present the photoemission feature of Ni 2p3/2 of SDC-Ni and SDC-Ni-Ru, the photoemission feature of Ni 2p1/2 is not shown in Figure 3.9G. The XPS spectra show that Ni displays both oxidative (Ni^{2+}) and metallic (Ni^0)

states. The amount of metallic Ni is low in both catalysts (11.6 mol% for SDC-Ni-Ru and 25.3 mol% for SDC-Ni), which could be ascribed to the rapid oxidation of surface Ni clusters (Figure 3. 9G) 16. Similar phenomena were also observed for the Ru 3p3/2 spectra of SDC-Ni-Ru and SDC-Ru catalysts (Figure 3. 9H). The surface Ru clusters tend to be oxidized when exposed to air, leading to the formation of Ru^{4+}. It should be noted that the SDC-Ni-Ru catalyst presents lower Ni^0/Ni^{2+} and Ru^0/Ru^{4+} ratios than SDC-Ni and SDC-Ru, respectively, suggesting that the Ni and Ru in SDC-Ni-Ru tend to form clusters that interact strongly with the SDC support, which is consistent with the H_2-TPR results. These results are combined with the XPS and H_2-TRP analysis to confirm that both Ni and Ru primarily exist as clusters on SDC-Ni-Ru.

Three types of oxygen species were identified on these catalysts (Figure 3. 9I): lattice oxygen (O_L), hydroxyl species (O_{OH}), and chemisorbed H_2O (O_W) 39. With the addition of Ru to the catalyst, the concentration of O_W increases from ~8 mol. % to ~11 mol. %, suggesting that the introduction of Ru could improve the water uptake capability of the catalyst. The amount of hydroxyl species, formed by the subsequent water molecule dissociation, on SDC-Ni-Ru and SDC-Ni is higher than that on SDC-Ru, implying the dissociation process can be promoted by Ni. Increasing the oxygen vacancy concentration favors the formation of hydroxyl species, implying that Ni addition (acceptor dopant) could increase the oxygen vacancy concentration in SDC 39. It has been widely recognized that a high oxygen vacancy concentration is also essential for DMR 40; 41. Therefore, all the characterizations suggested that SDC-Ni-Ru could synergize the advantages of both Ni and Ru, yielding enhanced DRM performance and coking tolerance.

3.6. DRM-PCFCs for simultaneous power generation, chemical production, and greenhouse gas mitigation

To determine the catalytic activities of the catalysts developed in this work, we first examined and compared the catalytic performance of SDC-Ni-Ru with SDC-Ru and SDC-Ni in a packed bed reactor (PBR), which is shown in Figures 3.10A-C and Figures S4. SDC-Ni-Ru is much more active and coking tolerant. Both hydrogen and carbon monoxide production rates increase with increasing temperature, which might have occurred because the high operating temperatures favor the highly endothermic DRM reaction (Figure 3. 10A and Figure S4A). As shown in Figures 3.10A and S4, SDC-Ni-Ru achieves the highest hydrogen and carbon production rates, indicating that Ni and Ru synergize to promote DRM. As DRM-PCFCs consume the produced H_2 to generate power electrochemically, a high hydrogen production rate is essential for a high current density (i.e., high power density). Operating the DRM-PCFCs under an enhanced current density can further promote the conversion of CO_2 and CH_4. Therefore, obtaining a high hydrogen production rate is key to achieving high-performance power generation, chemical production, and greenhouse gas mitigation.

The Arrhenius plots of the hydrogen production rate as a function of operating temperature shown in Figure 3. 10A indicate that SDC-Ni-Ru exhibits a lower activation energy (32.5 kJ/mol) than either SDC-Ru (42.0 kJ/mol) or SDC-Ni (51.7 kJ/mol), suggesting that Ni and Ru synergistically decreases the overall apparent activation energy for DRM 31. The lowered activation energy is vital for improving the DRM performance at <650 °C.

The second major challenge associated with DRM is its high propensity for coking. Therefore, catalyst stability is essential for integrating DRM catalysts with PCFCs. Long-term stability testing of these three catalysts was conducted at 650 °C (Figure 3. 10B and Figure S4B). SDC-Ni shows severe degradation, with a nearly 50% decrease in DRM performance after 60 hours of operation. The postreaction characterizations show a considerable amount of carbon formed on SDC-Ni (Figure S5). On the other hand, SDC-Ni-Ru and SDC-Ru retain stable operations for ~120 hours, suggesting that Ru is critical for enhancing coking tolerance. The PBR outlet gas compositions were also monitored as a function of time to confirm the stability of SDC-Ni-Ru. As shown in Figure 3. 10C, the total concentration of unreacted CH_4 and CO_2 remain at ~10% for 110 hours, indicating that SDC-Ni-Ru is stable during DRM.

DRM-PCFCs were then built by coating SDC-Ni-Ru on our PCFCs (Figure S6). The performance of the DRM-PCFCs was evaluated with a CH_4 and CO_2 mixture (CH_4 to CO_2 ratio = 1) that was fed to the anode, and ambient air was fed to the cathode. Figures 3.10D-E and S6-S7 compare the performance of the DRM-PCFCs equipped with SDC-Ni-Ru and without catalyst, which clearly shows that the DRM-PCFCs with SDC-Ni-Ru has significantly enhanced power density at 550-650 °C. For example, at 650 °C, SDC-Ni-Ru shows an increase in the peak power density from 380 mW cm^{-2} to 940 mW cm^{-2}, outperforming state-of-the-art DRM-PCFCs reported in the literature (Figure 3. 8D and Table S1). Additionally, as SDC-Ni-Ru displays a relatively low activation energy for DRM (Figure 3. 10A), it is expected that SDC-Ni-Ru could lead to more significant improvement at low operating temperatures. As shown in Figure 3. 8C, at 550 °C, the DRM-PCFCs achieve a practical PPD of 300 mW cm^{-2}, which is more than four times higher than that of pristine DRM-PCFCs. The open circuit voltage (OCV) of DRM-PCFCs, especially at 550 °C, still reaches ~950 mV (versus 750 mV for the pristine PCFC), suggesting that the SDC-Ni-Ru catalyst layer effectively converts CH_4 and CO_2 to syngas, which is consistent with the DRM performance demonstrated in PBRs. The corresponding EIS spectra (Figure S7A and Figure S8A) show that both ohmic resistance (Figure S9) and electrode polarization resistance (Figure 3. 10F) are substantially reduced on SDC-Ni-Ru, suggesting that such a catalytic layer enables an anode atmosphere that has a high H_2 concentration. To better visualize and differentiate the processes that occur in the DRM-PCFCs, distribution of relaxation time (DRT) analysis of EIS spectra was conducted and is presented in Figure S10. The DRT plots are divided into three main regions, the low frequency (LF, 100-1000 Hz), intermediate frequency (MF, 5000-50000 Hz), and high frequency (HF, >50000 Hz) regions, corresponding to mass transport, surface exchange kinetics, and the charge transfer process, respectively 43; 44; 45. First, the LF peak substantially decreases when SDC-Ni-Ru is used as the internal DRM catalyst, indicating that the gas diffusion process is significantly accelerated, which is attributed to the fact that SDC-Ni-Ru enhances CH_4 and CO_2 conversion and produces more H_2. Second, the DRM-PCFC with SDC-Ni-Ru also exhibits smaller MF peaks, indicating that surface exchange processes could also be promoted by SDC-Ni-Ru. Additionally, the catalytic layer could also improve the charge transfer steps. At 550 °C, the HF peak in the DRM-PCFC without the catalytic layer split into two peaks, implying that an additional charge transfer barrier exists, which suggests that the BZY-Ni anode is not active for DRM at 550

°C 46. The stability of the optimized DRM-PCFCs was then examined for simultaneous power generation, chemical production, and greenhouse gas mitigation. Figure 3. 10G shows that both DRM-PCFCs decorated with SDC-Ni-Ru and pristine PCFCs were tested at a constant current density of 500 mA cm^{-2}. The SDC-Ni-Ru-decorated DRM-PCFC attains a terminal voltage that stabilized at ~ 0.8-0.75 V, with slight degradation. The DRM-PCFC continuously generate electricity with a power density as high as 400 mW cm^{-2}, converting CO_2 and CH_4 to syngas (Figure S11A). However, the pristine PCFC shows severe degradation, with the terminal voltage decreasing from 500 mV to nearly 0 mV within 2 hours. This PCFC achieves much lower CH_4 and CO_2 conversion, while the produced H_2 concentration drops to 5% (Figure S11B). The severe degradation could be ascribed to coking, which blocks active sites for DRM. Due to the SDC-Ni-Ru catalytic layer, the SEM images of DRM-PCFCs do not show noticeable microstructural changes or carbon deposits on the anode of SDC-Ni-Ru-decorated DRM-PCFC (Figure S12), indicating that SDC-Ni-Ru improves the coking tolerance of the PCFC anode. Conversely, a considerable amount of carbon was observed on the anode of pristine PCFCs (Figure S13). Additionally, we have conducted the second DRM-PCFC stability testing (Figure 10H), which achieves >85 hours of stable operation at 650 °C, further confirming the improved durability of DRM-PCFC equipped with the SDC-Ni-Ru catalyst. To the best of our knowledge, we have for the first time lowered the operating temperature of DRM-PCFC stability testing to 650 °C 6; 11; 12; 14. As CO is produced at the anode, decreasing the operating temperature tends to favor the coking via Boudouard reaction. Therefore, all previous DRM-PCFC stability were evaluated at >700 °C to avoid coking and achieve durable operation. Despite the stability testing was not performed for an extremely long period (e.g., >1000 hours), the stability demonstrated in this work is much longer than all previously reported DRM-PCFCs and DRM-SOFCs 11; 12; 14; 47; 48; 49; 50.

3.7. In situ spectroscopy studies of the DRM catalyst

In situ DRIFTS experiments were conducted to probe the active intermediate species involved in DRM and understand the DRM mechanisms. As shown in Figures 3.11A-C, time-resolved DRIFTS spectra over three catalysts were collected upon changing the atmosphere from ultrahigh purity (UHP) Ar to CO_2 gas in a high-temperature DRIFTS cell chamber to identify the reactive absorbed species 51; 52. After the gas was switched, peaks for gaseous CO_2 (~2353.5 cm^{-1}) quickly emerged. Concomitantly, the intensity of the bands belonging to monodentate and bidentate carbonate species gradually increase, implying that they are involved in the CO_2 absorption process (Figure 3.11A-C). Monodentate carbonate was observed on SDC-Ni-Ru and SDC-Ru, while only bidentate carbonate was formed on SDC-Ni. To confirm that the monodentate and bidentate carbonates are the intermediate species chemically adsorbed on the catalysts, DRIFTS spectra were acquired during CO_2 desorption by switching the CO_2 gas to UHP Ar. As shown in Figure S14, the bands assigned to gaseous CO_2 quickly disappeared. At the same time, the carbonate species remained unchanged, confirming that the monodentate and bidentate carbonates could serve as the actively adsorbed species for DRM. After all gaseous CO_2 was removed from the reactor, the reactor atmosphere was changed to CH_4 (Figures 3. 11D-F). Upon exposure to CH_4, formyl (~1750 cm^{-1}) was observed on SDC-Ni-Ru and SDC-Ru 53, while CO species were

simultaneously produced on these two catalysts. When SDC-Ni-Ru and SDC-Ru were exposed to CH_4 for longer periods of time, the carbonate species (i.e., monodentate carbonate) gradually decrease, and the CO band tends to decrease, indicating that the carbonate species are consumed and converted to CH_4. Nevertheless, neither formyl nor CO was detected over the SDC-Ni catalyst. Furthermore, the bands associated with bidentate carbonate remained unchanged after the atmosphere was changed to CH_4, indicating that the carbonate species (i.e., bidentate carbonate) on SDC-Ni react slowly with CH_4 and produce an undetectable amount of CO, which is consistent with the PBR results, which shows that SDC-Ni displays poor DRM activity.

In situ Raman spectroscopy was conducted on both catalysts to study the coking tolerance of SDC-Ni-Ru and SDC-Ni. Compared with postreaction characterization, this *in situ* characterization approach reveals practical information about the dynamic interactions between the reacting gaseous species and catalysts. As shown in Figures 3. 11G-H, Raman spectra were collected as a function of time after the catalysts were exposed to a CO_2-CH_4 mixture. The D-band (1350 cm^{-1}) and G-band (1580 cm^{-1}), signs of coking, appeared quickly on SDC-Ni after ~35 mins. Therefore, SDC-Ni is prone to coking, which is consistent with the PBR results. With increasing operating time, the intensity of both peaks increases. An additional 2D band evolved at 2680 cm^{-1} after 50 mins, indicating continuous coke accumulation and graphene formation. In contrast, no clear signs of coking were observed on the SDC-Ni-Ru catalyst even after 1000 mins of treatment, further validating that SDC-Ni-Ru has significantly enhanced coking tolerance relative to SDC-Ni.

Figure 3. 11I presents the proposed DRM mechanism with SDC-Ni-Ru, which shows how Ni and Ru synergize to enhance DRM activity and promote coking tolerance. Ni favors the activation of CH_4, and CH_4 molecules dehydrogenate to CH_3*, CH_2, and CH*, consequently producing H_2. Without the oxidation of CH* to CHO*, further dehydrogenation can lead to coking. However, the bidentate carbonate formed on SDC-Ni does not actively react with CH*. Therefore, SDC-Ni is unfavorable for the oxidation of CH* and subsequent CO production. Additionally, SDC-Ni is more prone to coking. On the other hand, the addition of Ru accelerates the activation of CO_2 while altering CO_2 activation, forming monodentate carbonate, which is more active in oxidizing CH*. Therefore, CHO* readily forms on SDC-Ni-Ru and SDC-Ru, leading to CO production and enhanced coking tolerance.

3.8.Density functional theory (DFT)

Model SDC-Ni and SDC-Ru catalysts consisting of Ni_4 and Ru_4 clusters supported on SDC substrates were employed for DFT modeling to elucidate the conversions of CH_4 and CO_2 at different active sites. XRD Rietveld refinement (Figure 3. 9C) and HAADF-EDS mapping results (Figure 3. 9E) indicated that Ni and Ru clusters coexist independently on the SDC support. Therefore, the reactions taking place on Ni and Ru clusters were modeled individually. SDC-supported pyramidal Ni4 and Ru4 clusters were chosen since these are the simplest 3D metal catalyst clusters consisting of both interfacial metal sites and free metal sites. This configuration has been widely adopted to represent supported metal catalysts for DFT calculations [54; 55; 56; 57; 58]. The optimized catalyst models are illustrated in Figures 3.12A-D. For the SDC substrate, 4 Ce atoms in the CeO_2 (111) slab were replaced with Sm atoms. The lattice constant of the

optimized SDC is 5.411 Å, in good agreement with the XRD measurements reported in Table S3 (5.448 Å). The Sm doping sites were determined according to a report by Ren and coworkers 59. Because of the valence state difference between Ce and Sm, Sm doping is expected to promote oxygen vacancy formation. The most stable oxygen vacancy positions are indicated by black circles in Figure 3.12C-D. Both the Ni_4 and Ru_4 clusters bond with three surface lattice oxygen atoms. Upon optimization, the top Ru atom in Ru_4 displays slight tilting toward one of the surface Ce atoms.

3.9. Free energy profiles

The free energy profiles depicting DRM on different active sites are shown in Figure 3. 12E. All Gibbs free energies were estimated at 873 K (600 °C) and 1 bar using the standard statistical mechanical approach 60. The gas phase reactants (CH_4 and CO_2) and the clean surface were used as the free energy reference state. Free energy changes and energy barriers of elementary steps are shown in Table S5. The binding energies (BE) of the intermediate species reported in Table S6 are defined according to Eqn. 1:

$$BE = E_{total} - E_{adsorbate(g)} - E_{surface} \quad (1)$$

where E_{total}, $E_{adsorbate(g)}$, and $E_{surface}$ represent the total energies of the adsorbed surface species, adsorbate in the gas phase, and clean surface, respectively. The optimized structures of the intermediate species on the SDC-Ni and SDC-Ru surfaces are illustrated in Figure S15 and Figure S16, respectively.

3.10 Activation of CH_4 and CO formation routes

The initial C-H bond activation is a rate-limiting step in the DRM process, which usually takes place at metal sites 31; 32; 61. As shown in Figure 3. 12E, the first C-H bond activation is exothermic on both Ni_4 and Ru_4. The energy barrier on Ni_4 is 0.58 eV, which is lower than that on Ru_4 (1.04 eV). The dissociated CH_3* then undergoes stepwise decompositions to yield CH*. On Ni_4, the formation of CH* is facile, with negligible energy barriers. Overall, CH_4 decomposition is favored on Ni sites. On Ru_4, the conversion of CH_3* into CH_2* is more hindered. Moreover, *in situ* DRIFTS reveals the presence of the CHO intermediate only on the SDC-Ru and SDC-Ni-Ru surfaces. Hence, we can conclude that on SDC-Ni, the CH* → C* → CO* pathway is favored.

3.11. Adsorption and Conversion of CO_2

In situ DRIFTS also suggests different configurations for the carbonates formed on SDC-Ni and SDC-Ru. All the corresponding structures were optimized using DFT calculations and used for free energy calculations. As shown in Figure S15, on SDC-Ni, the carbon in CO_2 binds the surface lattice oxygen of SDC, with one of the O atoms in CO_2 located near the oxygen vacancy site and the other anchored by Ni_4. On SDC-Ru, as shown in Figure S16, the C in CO_2 binds a surface SDC lattice oxygen, while one of the CO_2 oxygens is anchored by Ru_4. Both configurations have been identified on the CeO_2 surface in previous research by *in situ* DRIFTs and DFT calculations 52; 62. The adsorbed CO_2 has lower free energy on Ru_4. As shown in Table S6, the binding energies of CO_2 on SDC-Ni_4 and SDC-Ru_4 are -1.47 eV and -1.72 eV, respectively. The CO_2 dissociation energy on the Ru_4 site is also much lower than that on the Ni_4 site (1.66 eV lower), which makes

the CO_2 activation process exothermic on the Ru_4 site but endothermic on the Ni_4 site. Therefore, CO_2 activation is favorable on the Ru_4 site. Combined with CH_4 decomposition, CH* is more likely to utilize the O atoms from CO_2 dissociation, producing CHO* as the intermediate for CO* production.

3.12. Synergistic Effect between Ni and Ru

The DFT calculations performed on SDC-Ni and SDC-Ru yielded findings consistent with *in situ* DRIFTS and enabled us to elucidate the reaction pathways at different active sites in SDC-Ni-Ru. It was found that Ni_4 is more active for the activation of CH_4, which works as a carbon and hydrogen supply for DRM, while Ru_4 plays a larger role in enhancing CO_2 adsorption and activation. As shown in Figure 11I, in the absence of Ru, stronger CH_4 activation may result in excessive carbon formation and make the C to CO conversion less efficient. Overall, this limits the performance of the entire DRM process. In a dual-site system, the Ru component contributes the necessary oxygen source. In this work, we demonstrated that the unique ability of Ni and Ru could be utilized simultaneously in a unified SDC-Ni-Ru system. The Ni sites provide high CH_4 activation capacity, while the Ru sites could activate CO_2 effectively, which significantly improves DRM performance. A similar synergistic effect was also revealed on a CeO_2-Ni-Ru catalyst for the DRM reaction 31. The free energy of SDC-Ni-Ru is plotted in Figure 3. 12E with the solid green line and shows that the energy barriers are mitigated significantly through the simultaneous use of Ni and Ru, especially for activating the first C-H bond of CH_4, CH* → CO* formation, and CO_2 activation.

3.13. Coke formation

The different characteristics of the Ni and Ru sites and the synergic effect also account for the coking resistance of SDC-Ru and SDC-Ni-Ru. On the SDC-Ni surface, the high capacity for CH_4 activation provides abundant carbon. However, the lack of an oxygen supply led to an accumulation of carbon on the surface, which is responsible for the poor coking resistance of SDC-Ni. For the SDC-Ru catalyst, a weaker carbon supply and abundant oxygen atoms from CO_2 activation make carbon accumulation on the surface more difficult. On the SDC-Ni-Ru surface, even though Ni sites boost the carbon supply, the accumulated carbon could be removed efficiently by coupling with oxygen supplied by the strong CO_2 activation on the Ru sites.

Besides, the free energy changes and energy barriers for C-C coupling on Ni_4 and Ru_4 were calculated, as shown in Figure S17 and Table S5. Both the activation energy barrier and free energy change in C-C coupling are higher on Ru_4 in Figure S17 (1.08 eV higher of energy barrier, 1.26 eV higher of free energy change), consistent with the observation that the Ru sites are more durable during DRM.

3.14. Summary

Herein, the operations of high-performance PCFCs, which intensify electrochemical power generation through DRM, were successfully demonstrated for power generation, chemical production, and greenhouse gas mitigation. A novel, custom-made DRM catalyst, SDC-Ni-Ru, was developed for the PCFCs, which simultaneously accelerates CH_4 activation, CO_2 activation, and mitigation of coking, leading to exceptional DRM performance and coking tolerance. The

PCFCs decorated with the SDC-Ni-Ru internal DMR catalyst achieve groundbreakingly high power densities of 0.94, 0.65, and 0.30 W cm^{-2} at 650 °C, 600 °C, and 550 °C, respectively, and outperform all previous DRM-PCFCs. Both experimental and computational studies were conducted to probe the DRM mechanisms and understand how the synergistic effect between Ni and Ru facilitates DRM and improves coking tolerance. The results of this work highlight the potential of DRM-PCFCs to address the challenges associated with power generation, chemical manufacturing, and greenhouse gas mitigation.

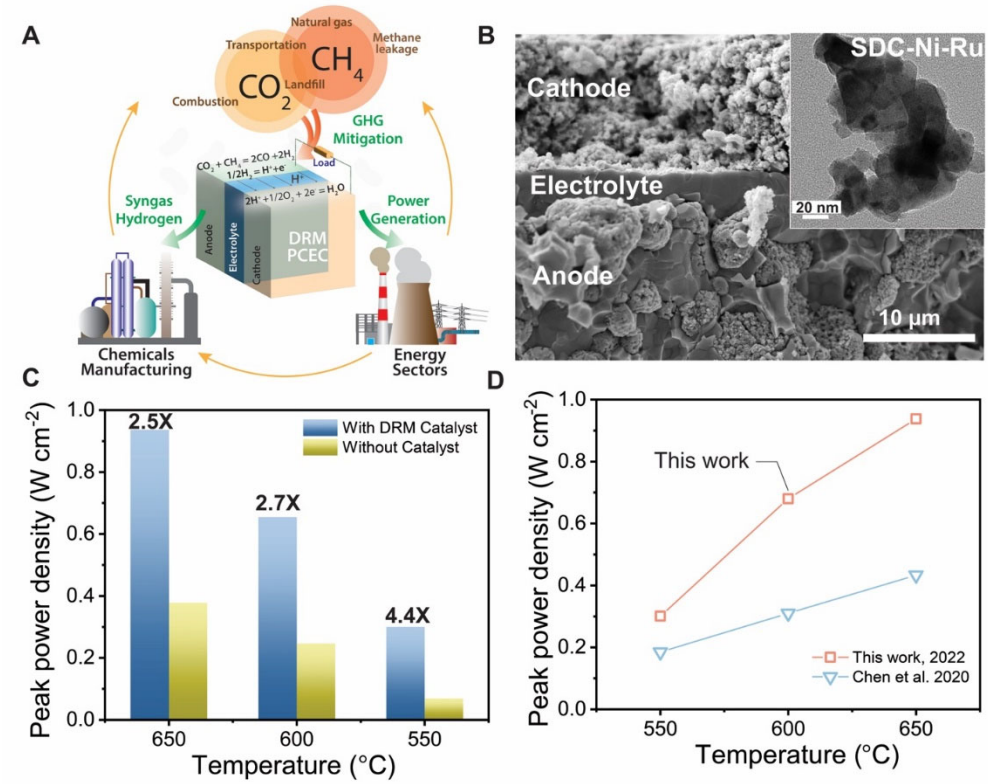

Figure 3. 8. DRM-PCFCs for electrochemical power generation, chemical production, and greenhouse gas mitigation. (**A**) An illustration of implementing DRM-PCFCs for simultaneous power generation, chemical production, and greenhouse gas mitigation. (**B**) A cross-sectional SEM image of the DRM-PCFC. The inserted figure shows the TEM image of the SDC-Ni-Ru catalyst coated on the PCFC anode. (**C**) Comparison of peak power densities (PPDs) of DRM-PCFCs with and without the SDC-Ni-Ru catalytic layer. (**D**) Comparison of PPDs of our DRM-PCFCs with state-of-the-art DRM-PCFC.

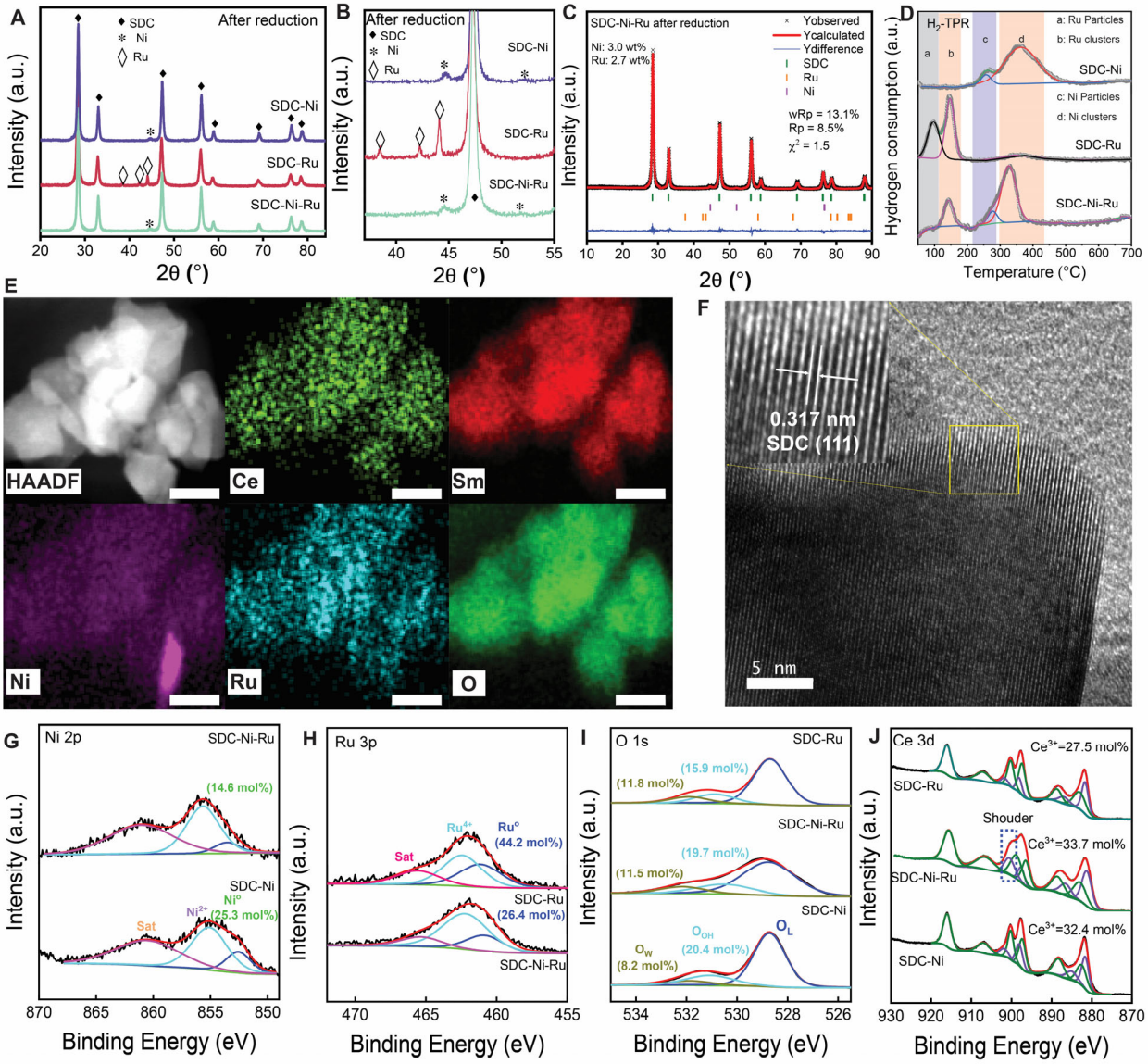

Figure 3. 9. The crystal structure, microstructure, and electronic structure of DRM catalysts. (**A**) X-ray diffraction (XRD) patterns of SDC-Ni, SDC-Ru, and SDC-Ni-Ru after reduction. (**B**) Enlarge scan range from 35 to 55° of the patterns shown in (A). (**C**) XRD pattern of reduced SDC-Ni-Ru and refinement results. (**D**) H_2-temperature programmed reduction (H_2-TPR) of SDC-Ni, SDC-Ru, and SDC-Ni-Ru. (**E**) High-angle annular dark-field (HAADF) and EDS mapping images of reduced SDC-Ni-Ru. The scale bar is 20 nm. (**F**) High-resolution transmission electron microscopy (HR-TEM) image of reduced SDC-Ni-Ru. X-ray photoelectron spectroscopy (XPS) of (**G**) Ni 2p, (**H**) Ru 3p, (**I**) O 1s, and (**J**) Ce 3d for reduced SDC-Ni, SDC-Ru, and SDC-Ni-Ru. The purple line refers to Ce^{3+} and the green line corresponds to Ce^{4+}.

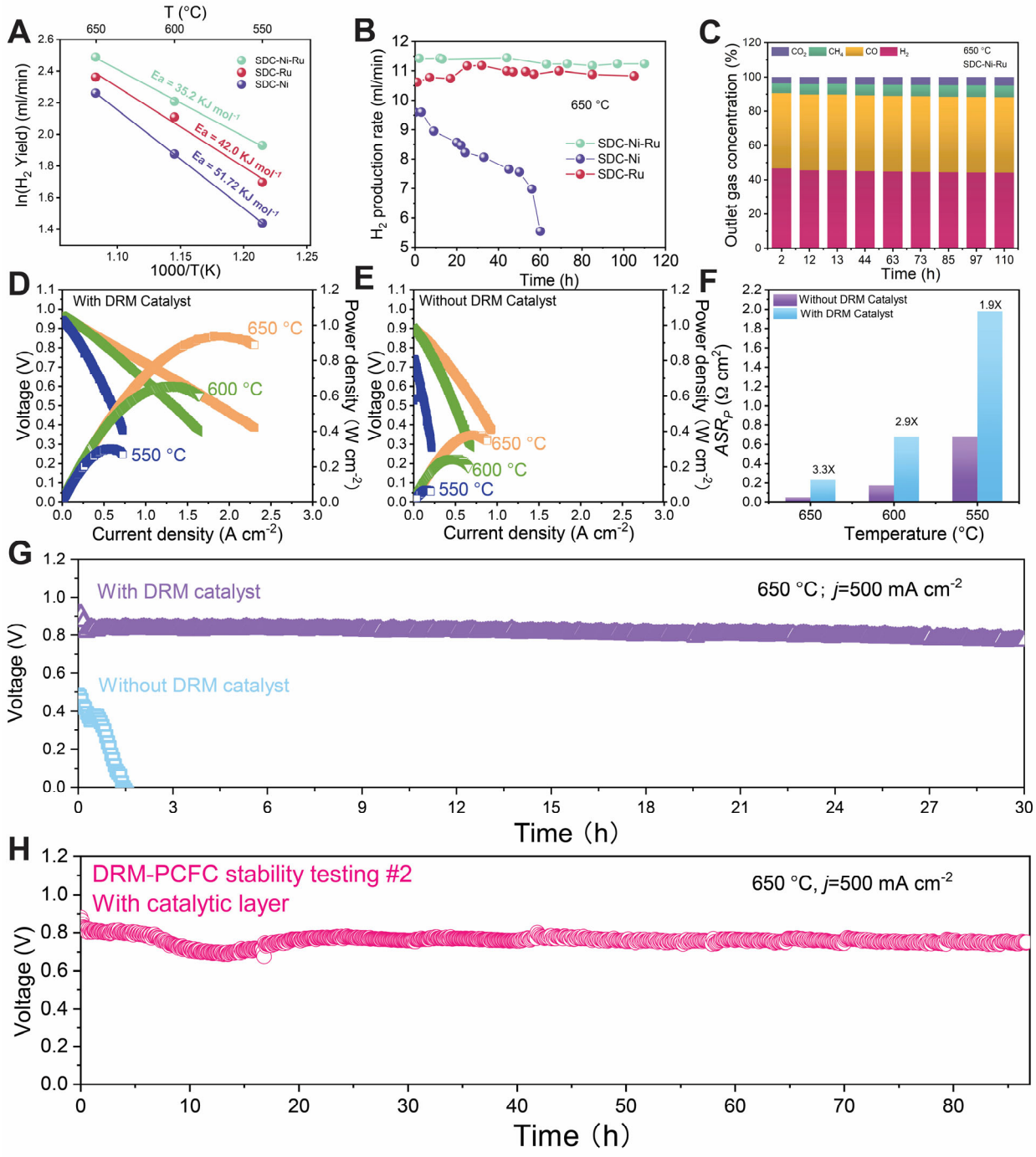

Figure 3. 10. DRM-PCFCs equipped SDC-Ni-Ru internal DRM catalyst for power generation, chemical production, and greenhouse gas mitigation. (A) Arrhenius plots for H_2 production rate achieved on SDC-Ni, SDC-Ru, and SDC-Ni-Ru in packed bed reactors. (B) The H_2 production rate as a function of operation time obtained on SDC-Ni, SDC-Ru, and SDC-Ni-Ru in packed bed reactors. (C) The packed bed reactor outlet gas concentration as a function of operation time for SDC-Ni-Ru at 650 °C. (D) *I-V* and *I-P* curves of a DRM-PCFC decorated with the SDC-Ni-Ru as the internal DRM catalytic layer at 650-550 °C. A mixture of CH_4 and CO_2 with a CH_4:CO_2 ratio of 1:1 was fed to the anode and ambient air was fed to the cathode. (E) *I-V* and *I-P* curves of a DRM-PCFC without catalytic layer applied at 650-550 °C. The testing

conditions are the same as the PCFCs shown in Figure 3D. (F) Comparison of the area specific electrode polarization resistance (ASR_P) of DRM-PCFCs with and without the SDC-Ni-Ru catalyst. (F) Comparison of electrochemical stability of DRM-PCFCs with and without the SDC-Ni-Ru catalyst at 650 °C. The PCFCs were tested under a constant discharging current density of 500 mA cm^{-2}. (H) The second stability testing of DRM-PCFCs with the SDC-Ni-Ru catalyst at 650 °C and a current density of 500 mA cm^{-2}, which further validates the durability of DRM-PCFCs.

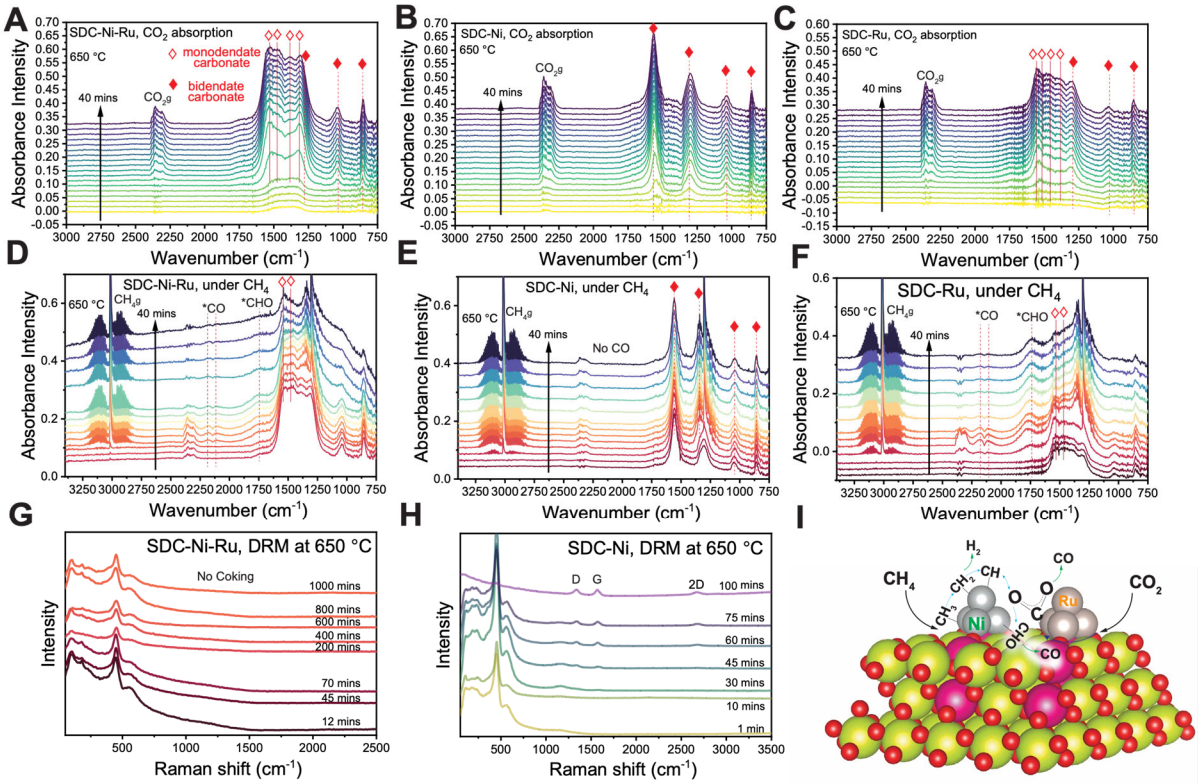

Figure 3. 11. In situ DRIFTs and Raman spectroscopy to probe the intermediate species and coking tolerance for DRM. *In situ* DRIFTs spectra of CO_2 absorption on (**A**) SDC-Ni-Ru, (**B**) SDC-Ni, and (**C**) SDC-Ru at 650 °C. All samples were first reduced at 650 °C for 1 h and cooled down to 25 °C under H_2. The atmosphere was then changed to ultrahigh purity (UHP) Ar to collect the background. Upon changing the feeding gas from UHP Ar to 20 sccm CO_2 and 20 sccm Ar, the spectra were collected as a function of operation time. *In situ* DRIFTs spectra of dry reforming of methane by chemically adsorbed species on (**D**) SDC-Ni-Ru, (**E**) SDC-Ni, and (**F**) SDC-Ru at 650 °C. After purging 100 sccm UHP Ar for CO_2 desorption, the atmosphere was then switched to 20 sccm CH_4 and 20 sccm Ar. *In situ* Raman spectroscopy of DRM on (**G**) SDC-Ni-Ru and (**H**) SDC-Ni at 650 °C. The gas fed to the high-temperature Raman cell was 10 sccm CH_4 and 10 sccm CO_2. D indicates disordered carbon. G corresponds to the graphite. 2D is attributed to the 2-dimentional graphene. (**I**) Proposed DRM mechanism on SDC-Ni-Ru. The Ce, O, Sm, Ni, and Ru atoms are in yellow, red, wine, grey, and brown, respectively.

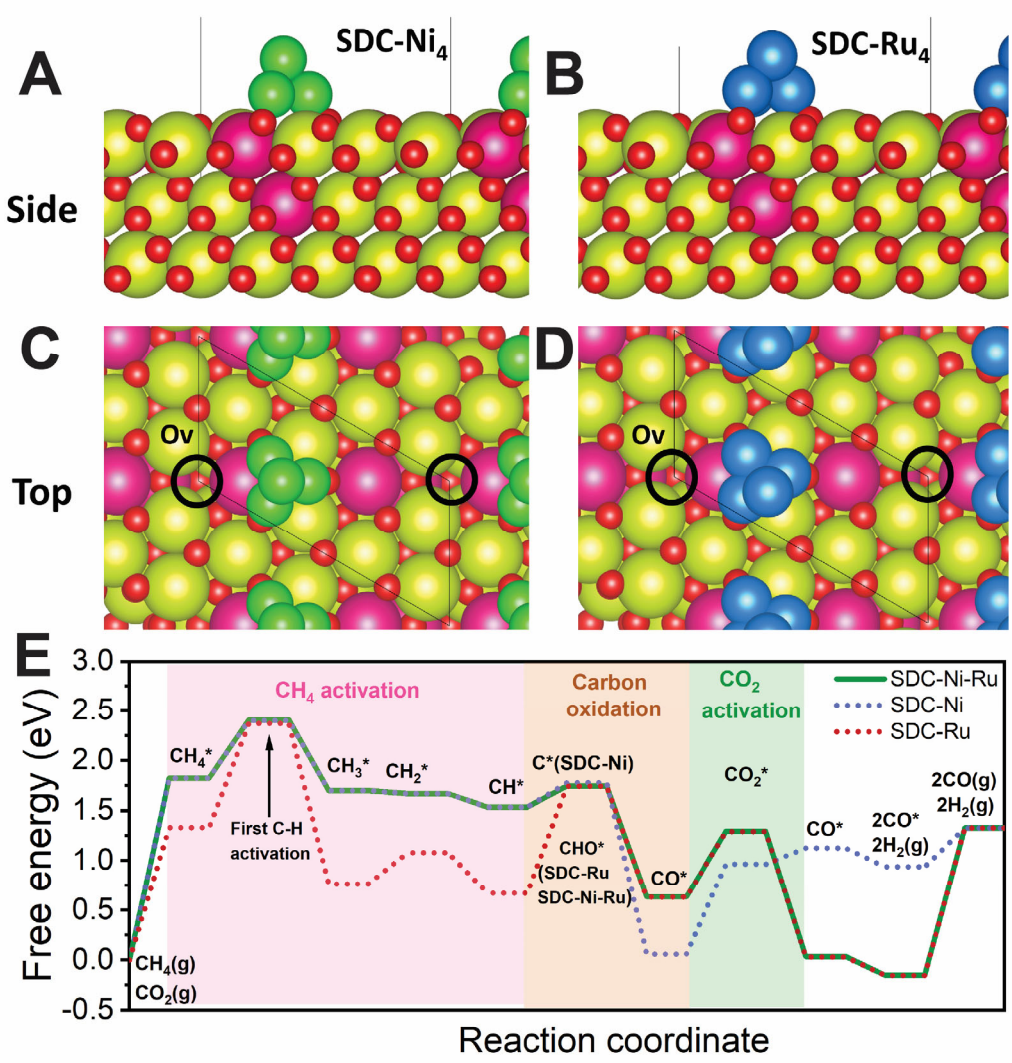

Figure 3. 12. DFT calculations to study the synergistic effects between Ni and Ru for DRM. (Optimized $SDC\text{-}Ni_4$ (**A**, **C**) and $SDC\text{-}Ru_4$ (**B**, **D**) surfaces. Solid black lines indicate the supercell boundaries. Positions of oxygen vacancies are indicated with black circles. The Ce, O, Sm, Ni, and Ru atoms are in yellow, red, wine, green, and blue, respectively. (**E**) Free energy diagram depicting DRM performance on SDC-Ni, SDC-Ru, and SDC-Ni-Ru generated at 873 K and 1 bar. Key pathways include CH_4 activation, carbon oxidation, and CO_2 activation.

4. Comprehensive Computational Modeling of Reversible Methane PCER

For accurate system evaluation, reduced-order models of less complexity are required. These models should be detailed enough to correctly represent the complex physical phenomena inside each device but lean enough to be implemented into a system model and solved within a reasonable calculation time. The goal of this task is to develop such models as a bridge between the more sophisticated and lower-order models.

Our models are currently designed to represent details of reactive porous-media transport, elementary catalytic chemistry, and electrochemistry within unit cells of PCERs. Briefly, we have constructed a one-dimensional button-cell model for PCECs using the Engineering Equation Solver (EES). The model specifically focuses on the co-electrolysis of CO_2 and H_2O to produce methane. The model is validated and calibrated with experimental results. The model shows lower voltage output as the operating temperature increases and predicts the cell potentials at lower operating current densities. It also gives insight on the effect on the overpotentials on the cell output which enhances dexterity in its design and choice of stack and building materials. The model presents the rate of methane production at different temperatures and revealed that efficient PCEC for co-electrolysis of CO_2 and H_2O is operated in the temperature range of 420-470°C and the optimum being 450°C at the rate of 0.0391 $moldm^{-3}min^{-1}$. Presumably from the model, it shows there is need for enough water for higher CH_4 production and the water electrolysis is the rate determining step in co-electrolysis of CO_2 and steam in PCEC. The outcomes of the model rationalize the potential utilization of the PCEC as a CO_2 sink for decarbonization purpose and methane production that can be transferred into real life fuel utilization.

In this work, we validated the OCV of modeled perovskite-supported PCEC for co-electrolysis of water and CO_2 for methane production and compare it with available experimental results. The polarization curves for the electrolysis-methane synthesis at 500°C and other temperatures compared with the empirical data are shown in Figure 4.1. It was reported that the operating temperature range for efficient operation of the PCEC is from 400-600, so the average of these temperatures (500 °C) is chosen as a base and reference validation temperature. Figure 4.1(b) further compares the experimental data and our model in this work at 450, 500 and 550°C. To probe if our model is a good representation of the experimental results, errors between the two data were estimated as shown in Figure 4.2. The errors at all temperatures fall below the highly significant error reference of 0.001 which is strong evidence of the reliability of our model. Likewise, statistically comparing our model with the empirical data using the Wilcoxon signed rank test, at the 0.05 level shows that there is no significant difference between the two.

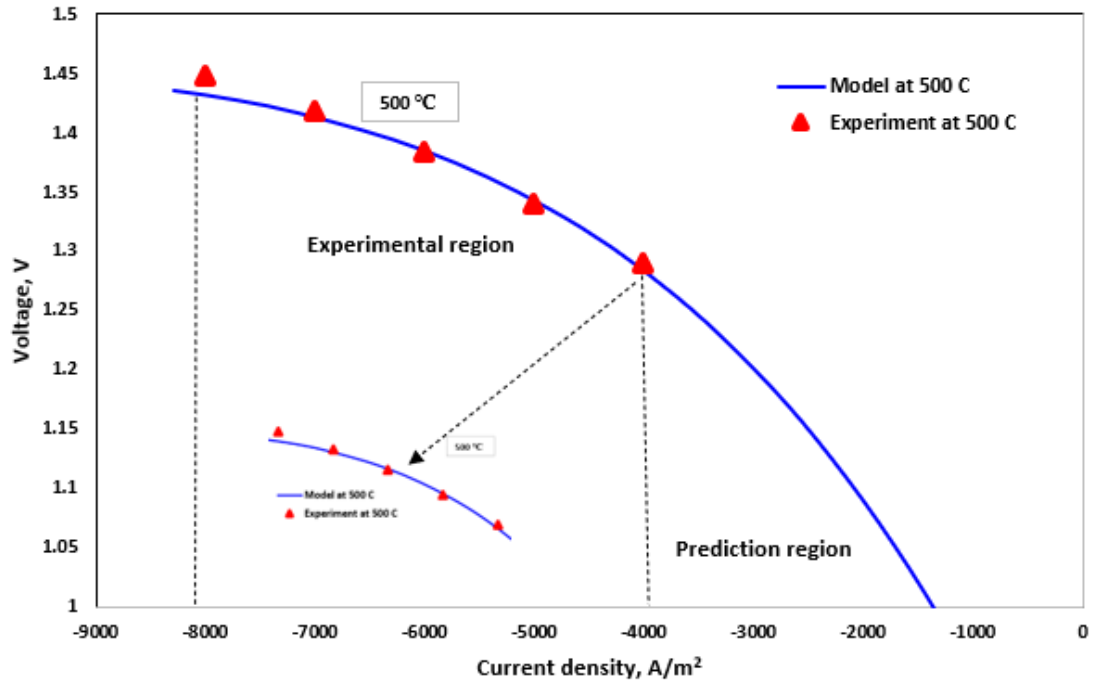

(a)

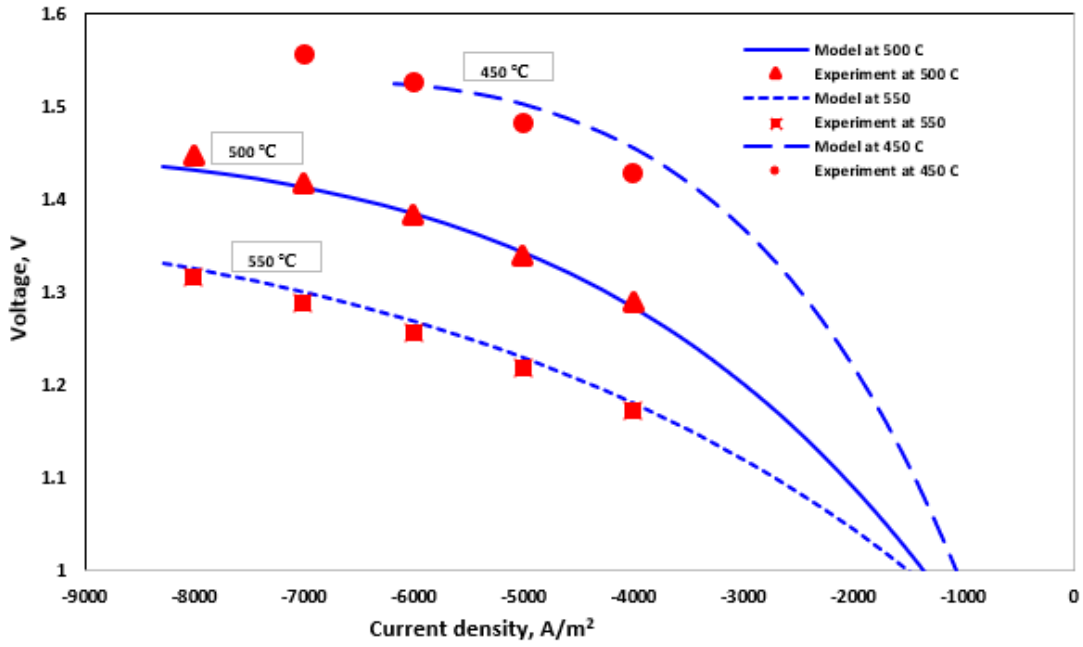

(b)

Figure 4.1: Comparison between the polarization curves of model simulation results and experimental data a) comparing at 500°C b) prediction at other temperatures and lower current densities.

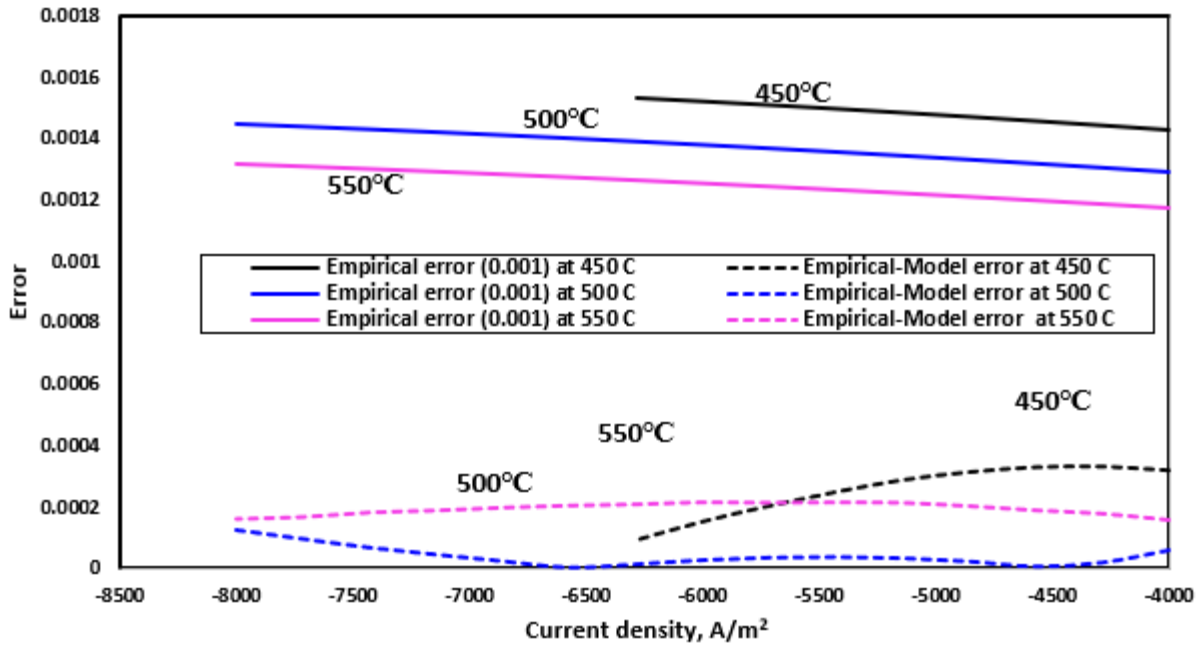

Figure 4.2: Error curve for the empirical and model results

The stack model for the RePCEC is calibrated and validated using the experimental results developed by KSU and Colorado School of Mines. The cell is validated for 5 cm^2 unit stack PCEC with BCZYYb electrolyte (almost 8μm) and 60 wt % NiO and 40 wt% BCZYYb fuel electrode (about 0.8mm) composition. The air electrode composition is 80 wt% BCFZY and 20 wt% BCZYYb. The validation is carried out individually on both modalities, as shown in Figure 4.3 (a) and (b). In all cases, it is assumed that there is adequate sealing of the stack and no significant gas leakage to minimize the resistance losses. In the experimental test at these temperatures, methane is directly fueled into the PCFC using a fuel mixture of CH_4, steam, and N_2 with flow rates 20, 67 and 80 sccm, respectively. This composition resulted in a steam-to-carbon ratio of 3.35. A high N_2 flow rate is supplied to lower the concentration of steam and mitigate its flow rate fluctuations. However, it is anticipated this might reduce the performance of the cell due to the dilution effect caused by the excess of non-reactive nitrogen gas. Figure 4.3 (a) show the PCFC operation polarization curve for comparing the experimental results with the model results at different temperatures 400-550 ℃. Here, the cathode composition is made up of 10% H_2O and 90% O_2 and the anode composition is 12% CH_4, 48% N_2, and 40% steam. The model exhibits a high degree of precision and minimal error across a wide range of current densities, and the stack voltage considers all the significant types of polarizations and overpotentials, the ohmic, concentration, and activation overpotential.

Likewise, Figure 4.3 (b) shows the PCEC mode operation polarization curves comparing this model and experimental results. It was reported that the operating temperature range for efficient operation of the PCEC is from 400-600, however, the experimental work uses temperatures 400-550℃. As depicted in Figure 4.3(b), there is a non-linear increase in the operating voltage from

1.3 to 1.5 V as the current density increases from -4000 to -10000 Am^{-2} at 500 °C as expected. The same trend is observed in the empirical data and the model prediction at other temperatures as shown in the figure.

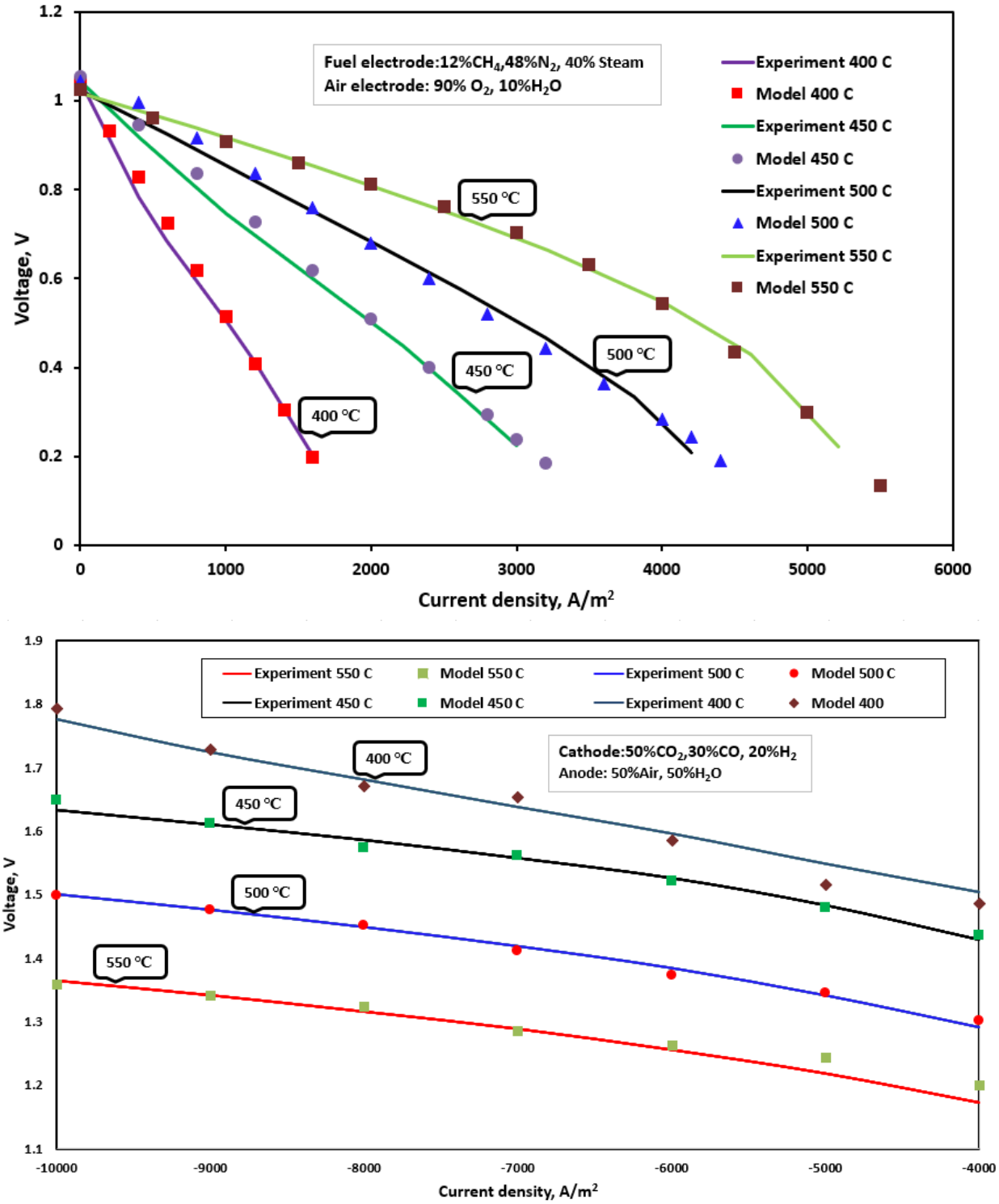

Figure 4.3: PCFC stack validation I-V curve and Polarization curve (a) PCFC (b) PCEC

Due to the intricacy and the complexity of the co-electrolysis reaction in the PCEC, the empirical study supplies the fuel electrode with is a gas mixture of CO_2 and N_2, without H_2. Thus, the reducing environment during the operation is only maintained by the H_2 produced from the electrolysis process at the steam electrode. Therefore, to avoid possible oxidation of the Ni catalyst and maintain continuous co-electrolysis reaction due to limiting reactant, the minimum current density during the test was set as 4000 A/m^2. However, due to the versatility of the model we are able to predict a situation where the nickel catalyst is not oxidized or an alternative non-oxidizable catalyst of similar activity is used. Consequently, we extend the polarization curves to a current density of 0 A/m^2 at 500°C shown in Figure 4.4 to address the open-circuit voltage (OCV) for both modalities. A correlation between the experimental results and this model as depicted in Figure 4.2 (a) shows the degree of precision in the model. At all temperatures and current densities, the maximum error observed in the model compared to the experimental results is 2% which can be statistically considered as accurate most especially in the electrochemical community.

The stack model is used to predict the operation of the cell in PCFC mode with a different fuel composition and temperatures as shown in Figure 4.5. The polarization characteristics curves as different temperatures shows that the power density increases with temperature. The peak operating power density for co-electrolysis of CO_2 and H_2O is 0.22 W/cm^2 at 0.63 V and 550 °C. This performance is superior to the reported power density of 0.18 W/cm^2 at 0.8 V and 600 °C. which reveal a developmental progress in the PCFC design and its materials. The power densities at other temperatures 500, 450 and 400 °C are 0.144, 0.1 and 0.05 W/cm^2 respectively.

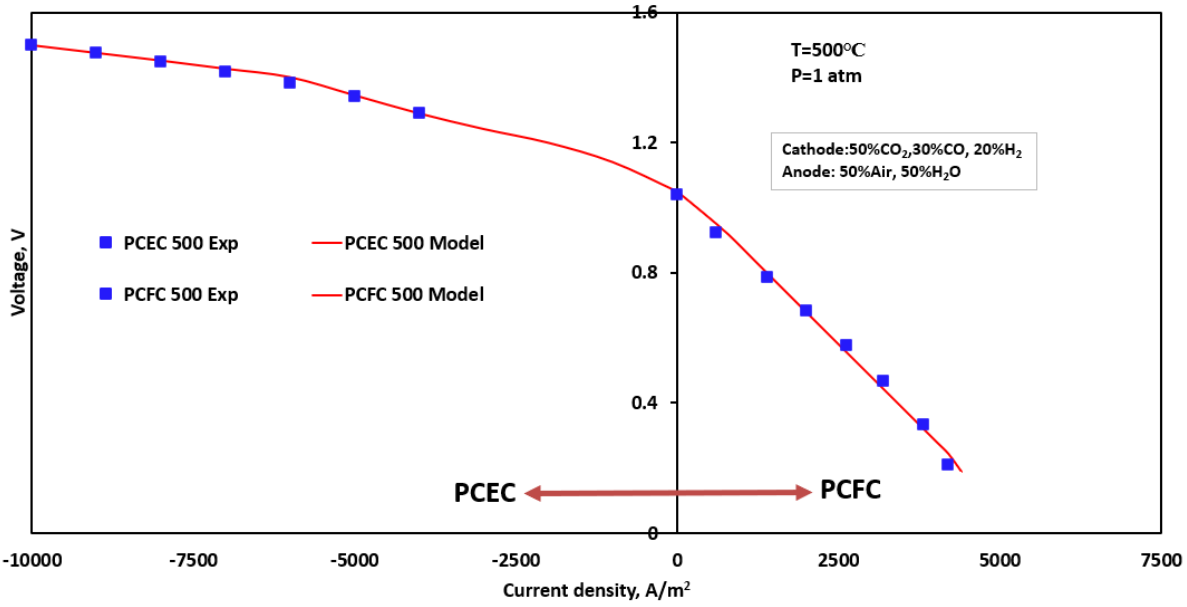

Figure 4.4: The reversible operation of RePCEC

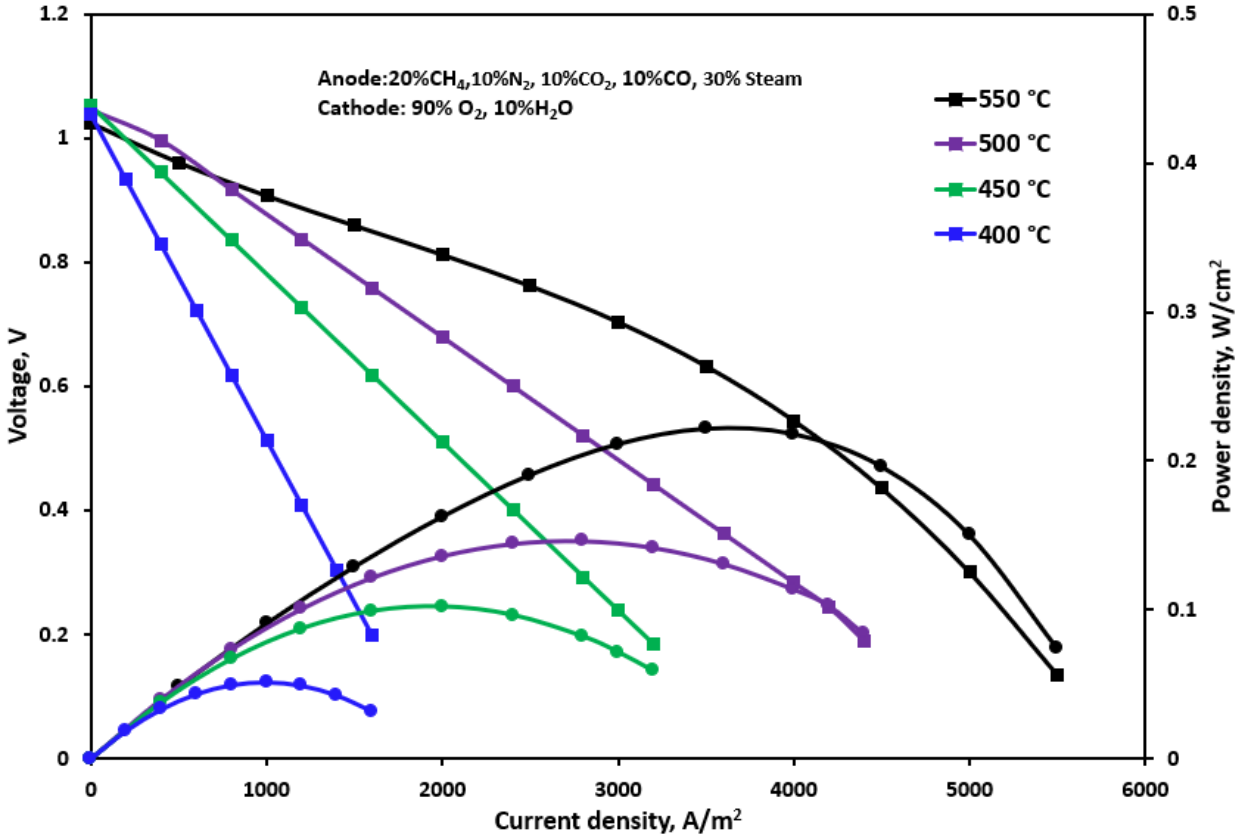

Figure 4.5: The I-V and P-V curves of the PCFC stack from the model

5 – Comprehensive Techno-economic System Modeling of Reversible Methane PCER

The goal of this task is to use Techno-economic analysis (TEA) to quantify the benefits of the new energy storage technology and identify the critical performance and cost parameters. Conducted a comprehensive TEA for this new energy storage technology. National Energy Technology Laboratory (NETL) recommended analysis procedures are employed as a guideline to ensure the quality and completeness of the analysis.

5.1- Develop a Technology Analysis Plan (TAP) and Performance Model

The stack model is simulated in Task 4 and its operation in a reversible protonic ceramic electrochemical cell system is evaluated through the use of a computational model. The system configuration to get a high quantity of the primary reactants (CO_2 and H_2O) into the stack during its integration for a system level design is key to achieving high methane production. While higher stack roundtrip efficiency of over 80% is achievable when integrated with combined cycle powerplant of 600MW, the overall system efficiency is limited by the BoP power demand. To achieve overall system level performance for an isothermal operation of this type, the BoP energy should be appropriately integrated both at the upstream and downstream of the system to minimize energy consumption and heat loss. The stack isothermal operation benefits from high methane production for its heat to balance up with the demand during steam electrolysis which will eventually improve the system performance. To accomplish this, operations need to be within the

temperature range of 450-525℃. Results show that 450℃ and 525℃ are the optimum temperatures for methane production and stack roundtrip efficiency respectively. The generation of heat within the RePCEC stack, especially during electrolysis mode, represents a significant limitation within the system and is influenced by factors like current density, reactant composition, and operating temperature. Analyzing these operational parameters parametrically uncovers trade-offs between stack durability, thermal management and finally stack and system efficiencies.

Another distinguishing advantage about the co-electrolysis in the RePCEC, is the potential to simultaneously generate hydrogen from the system. This gives a dual chemical storage for renewables, as the hydrogen can be taken in parts from the system loop as posited in the system configurational design which gives the highest stack and system efficiencies. Detailed profitability analysis will reveal the economic value this will add to the process.

There are different configurations for the integrated system. The process flow diagram for the integrated system for hydrogen production is shown in Figure 5.1. The system is based on RePCEC connected to two different sources of high pressurized steam (HPS) and CO_2 from power plant aimed at being integrated into the grid. In this process, 500 m^3/s flue gas from combined cycle power plant with 600 MW total capacity is passed through an electrostatic precipitator to remove the particulate matters with insignificant pressure loss. The outlet from the precipitator is sent to the water removal. Other flue gas composition (CO_2, N_2, O_2) is stored in the exhaust tank and passed through the heater to increase its temperature to the PCEC cathode inlet temperatures of 400-550℃. Likewise, water from a wastewater/ freshwater reservoir at ambient temperature and atmospheric pressure is pumped to the water treatment and recovery unit (WTRU) at a pressure of 250kpa with the goal of evaporating it to generate steam. The recovered water from the flue gas is pumped to a heat exchanger where it is superheated and evaporated for high pressurized steam generation, and the HPS here is mixed with that obtained from the WTRU. The mixed HPS stream is stored in the exhaust tank and enters the PCEC stack anode after passing a pre-heater where it is heated to the inlet temperature range of 400-550 ºC. This lower the required entropic heat to decompose the steam endothermically when compared to liquid water and as a result reduces power consumption. The heater is designed to utilize waste heat from the PCEC's product lines, leaving the system considering that a larger percentage of the heat added to the feed stream is retained in the exit gas stream. Waste heat from external sources also works suitably with the heater. Heat integration recuperation is carried out such that the heat from the stored gases in both the exhaust and fuel tanks are used by the heaters and heat exchanger at the stack inlets and outlets respectively. Likewise, the heat removed from the flue gas is used by the WTRU, water heater and evaporator as the case may be. Air from the ambient environment is compressed, preheated, and supplied to the system to flush out the produced oxygen from the electrolysis reactions in the PCEC. This also serves as a medium for carrying heat into the stack to meet the boundary conditions, and the streams exit the stack. An external source of heat ($T\Delta S$) is essential as it reduces the required electricity per volume of hydrogen gas produced compared to other electrolyzer technologies. The change from liquid water to steam electrolysis enhances an appreciable drop in the demand for electricity followed by a steady decrease with increasing temperature.

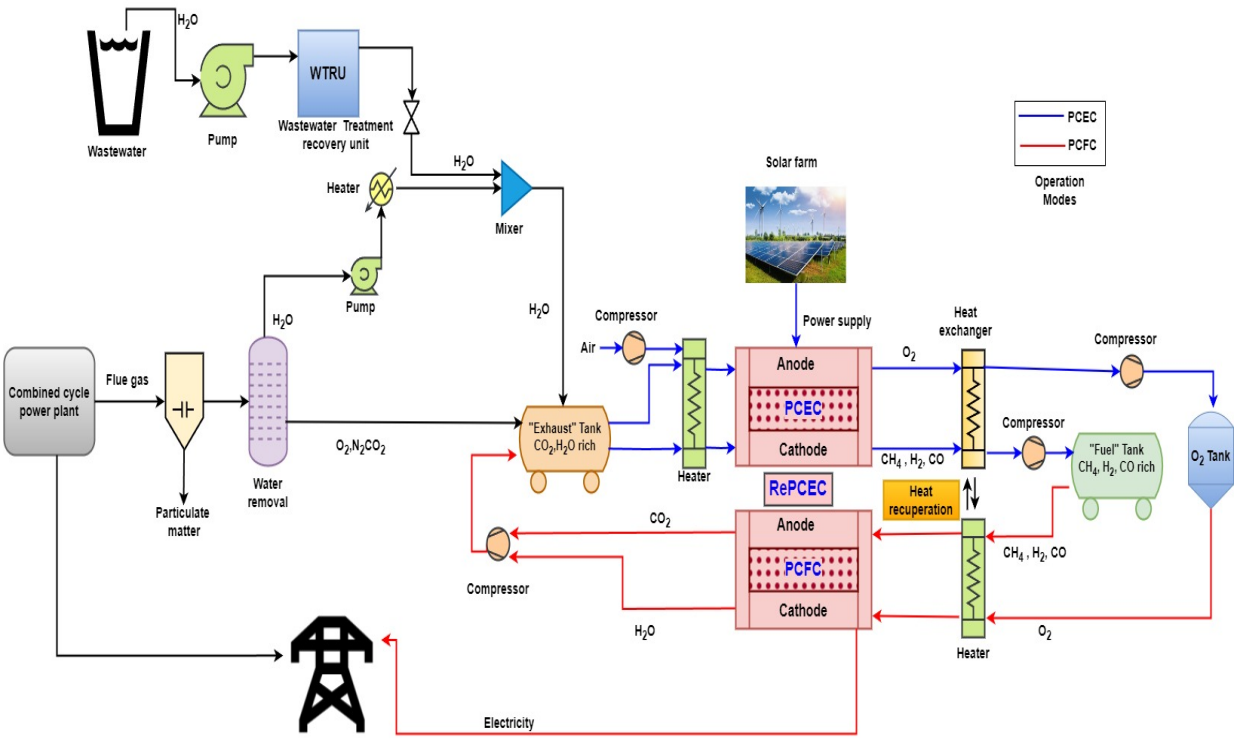

Figure 5.1: The RePCEC integrated system for co-electrolysis of CO_2 and H_2O (base case, BC)

The results show that the percentage conversion of CO_2 is 55.7%. The rate of methane production, its percentage production and its selectivity are 1795 kmol/h, 35.9% and 62.6% respectively. The stack and system roundtrip efficiencies for this base case are 65.18% and 42.79% respectively, suggesting that there is a notable decrease in efficiency due to the BoP energy consumption for the process. This higher energy can also be traced to the huge volume of non-participating gases like nitrogen from the flue gas that needs to be heated and passed across the components along with the participating gas like CO_2. The exhaust tank requires higher energy to maintain its isothermicity with this quantity of gases in the PCEC mode. Another challenge with the tank in the PCEC mode is the required tank volume to contain the exhaust from the flue gas. The gases from the powerplant and steam are at higher temperatures compared to the tank storing temperature which can be explored to reduce the energy consumption by the BoP. The fuel tank experiences similar unnecessary storage of the inert gas during operation as its content is dependent on what the exhaust tank is passing to the stack. Depending the on the grid energy demand and storage time before utilization, conducting a more detailed analysis with increased accuracy is essential to investigate the transient effects of the storage tanks (particulary the exhaust tank), considering specified tank geometry and materials. This is necessary to finalize this aspect of the system design. However, applying some cleaning equipment and reconfiguring this base case might give better stack and system efficiency and performances.

We have conducted more analysis to determine the optimal system configurations and operational conditions for use in a large-scale energy storage application. There are different configurations for the integrated system which influence the overall and PCEC stack efficiency. This ranges from the input feed generation from the BoP configuration and returning of the products from the downstream back into the stack. Following the base case discussed above, this system is without a carbon capture system. It can be observed in this base case that the feedstocks to the fuel channel have only 4.3 mol% CO_2 which is one of the primary reactants. Having a system that can remove a higher percentage of CO_2 might improve the system both technically and economically. In the work performed by OU team, the designed two-staged membrane carbon capture system (TSMCCS) with relatively cheap cost of CO_2 capture of 27.35 \$/tCO_2. From the study, the retentate having higher concentration of the inactive gases exit at higher pressure and can replace the compressed air in the base case without carbon capture system (CCS). There is a dual economic benefit of this, reduction in both capital and operating costs. The capital cost saves from non-procurement of compressor. Likewise, the operating cost saves from the compressor operational cost and energy required to keep these inert gases at the stack and BoP components operating temperatures. However, an extra tank is required to store them. This seems milder as the needed quantity might be stored and put in the remain for an immediate use. Adding a carbon capture system to this base configuration gives a new one shown in Figure 5.2. The system here is based on RePCEC connected to two different sources of high pressurized steam (HPS) and CO_2 from two-staged membrane carbon capture system (TSMCCS) integrated into the grid and renewable energy sources. In this case, higher mol% of the CO_2 captured from the power plant goes to the cathode side of the stack with O_2 and N_2 serving as sweep gas. While there are several runs and powerplant loading carried out for CCS, 100% loading is used in this case.

The mol% of CO_2 fed into the stack is over 60% unlike the base case with just 4.3%. Running the system under this condition results in the percentage conversion of CO_2 of 73.3%. The rate of methane production, its percentage production and selectivity are 3100.6 kmol/h, 62.01% and 92.27% respectively. The stack and system roundtrip efficiencies for this base case are 72.1% and 51.37% respectively. While all the performance metric parameters are higher with the CCS system, the overall system efficiency is low. This typically shows the influence of the BoP energy requirement on the overall system efficiency as the additional energy demand by the CCS system plays it role. It is noteworthy to mention that the RePCEC stack itself is highly energy consuming. However, the total moles of CO_2 available for reaction is lower than the base case.

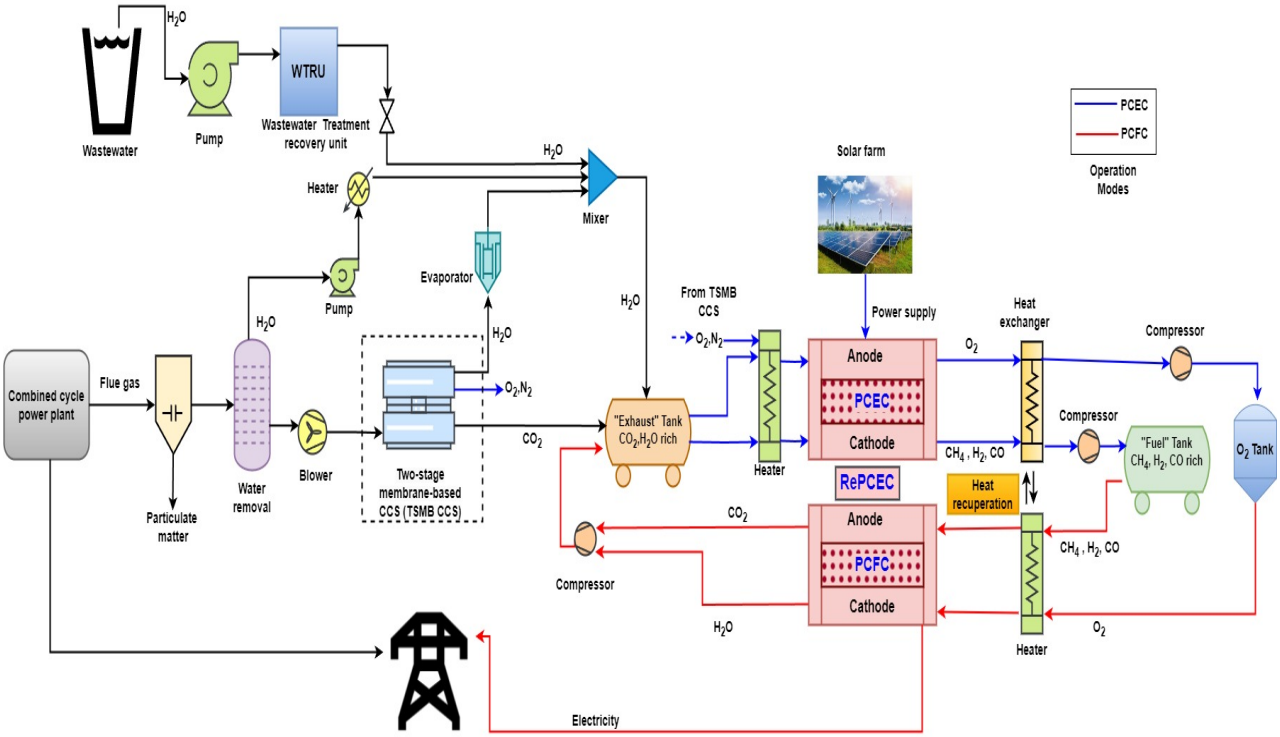

Figure 5.2: The RePCEC integrated system for co-electrolysis of CO_2 and H_2O with carbon capture system (BC +CCS)

Making more CO_2 for reaction is likely to increase both the stack and system performance. This can be achieved by adding more exhaust tanks reserved for CO_2 storage. Likewise, the efficiency of the CCS is key to high stack and system performance. High level energy recovery design among the BoP is very critical for system performance, most especially among the heater, cooler, water separator and the compressors. This needs to be carefully managed at the system upstream. Comparing the base case without and with CCS, the results show that the latter outperformed by all metrics. So, the focus and attention are the improvement of this base case with CCS.

The inclusion of recycle, bypass, purge streams and several cleaning systems in the strategic part of the operation system is essential for high productivity which therein gives different configurations. However, the system economics required adequate attention to decide which of this addendum equipment is needed and place to put it in the process stream. After diligent management of the upstream with the previously suggested strategies ranging from additional tanks and heat integration to enhance the availability of active reactant and reduce energy demand, then the improvement of the downstream is necessary.

Segregating the reactants generation section at the upstream of the base configuration with CCS, further configurations will focus on the downstream. While dealing with the downstream, stringent measures are needed to identify possible area heat integration and energy demand. Also, the upstream would be run simultaneously with the downstream at different operating conditions to quickly identify point of needs and improvement. This also enhances synchronization. Three additional configurations are added to the two base cases. Different system design setups are assessed using roundtrip efficiency and stored energy density as evaluation criteria. The first of

the three configurations is recycling of the upstream product for the PCEC operation mode. It has been mentioned that the base case with CCS is the focal configuration, however, to study the effect of product recycling, recycles are attached to the two base cases. This recycle stream configuration is typical of the previous two configurations, what differs is the addition of the recycle stream to the product of the PCEC mode operation. The simulations are carried out at the same operating conditions. As stated in the results for the two cases, the amount of unreacted CO_2 in the product streams is 44.3% and 26.7% for the base case (BC) and the BC with CCS (BC+CCS) respectively. The recycle stream takes this unreacted CO_2 in part or as whole back to the feed stream for reaction. This enhances more production of methane, and also saves energy from generating fresh CO_2 to the required feed temperature. Even though energy is expended in the recycling stream, this is not comparable to what is required to generate the same amount of CO_2.

The second configuration after the base cases, is the use of an additional storage tank to support the exhust tank which makes CO_2 abundantly available for the stack. The CO_2 for the extra storage tank is gotten from the TSMB CCS retentate and addition from an external source can also be used. The last configuration considered is this work is addition of purge to the exit streams. The exiting oxygen from the anode is purged and put to other uses. The heat from the high temperature oxygen can be integrated into other part of the system or sent to the plant for use. In this case, the required O_2 tank volume required is smaller compared to when it is not purged which definitely serve an economic purpose. Likewise, hydrogen is purged from the cathodic channel of the PCEC operational mode. This seems to have both economic and environmental benefits; it reduces competition between the combustion of methane and hydrogen in the stack. While purged hydrogen can be used for other green purposes, the system also reduces the quantity of unreacted methane. In all purging cases, energy is saved from maintain the

Five main configurations with two supplementary ones have been considered in this work namely and initialized respectively as follows,

a. Base case (BC);
b. Base case with carbon capture system (BC+CCS)
c. Base case with recycle stream (BC+RS)
d. Base case with carbon capture system and recycle stream (BC+CCS+RS)
e. Base case with carbon capture system, recycle stream and extra water stream (BC+CCS+RS+H_2O)
f. Base case with carbon capture system and purge stream (BC+CCS+PS)
g. Base case with carbon capture system, purge stream and exhaust tank (BC+CCS+PS+Tank)

The cases c-e is considered as one main one, to study the impact of recycle stream on the system performance. Recycle ratio of 0.2 is chosen as the base parameter across all configurations to avoid accumulation of unused reactants. For the purging configuration, 5000 kmol/h of hydrogen is purged from the process stream after the PCEC mode operation. Figure 5.3 and Table 5.1 show the results of the simulation for these configurations at the described system operation and parameters.

From the table, there are situations whereby the flowrates of the produced methane are the same. This can be traced to the depletion of one of the reactants and the steam in this case. Addition of CCS as previously posited enhance the stack and system performances. However, excess steam is not favorable for the stack and mild for the overall system performance. As shown in the table, purging some of the exit gases before storage is both beneficial to the stack and system performance. Identifying this, further studies is carried out on these cases with some other operating parameters and detailed in later part of this section.

Using the CCS permeate alone for the base case with CCS gives CO_2 conversion, methane production rate and Selectivity of 15.1%, 162.1 kmol/hr and 23.43% respectively. However, the RePCEC stack roundtrip efficiency of 66.6% for this configuration is higher than the 65.2% for base case. The higher values of other metric other than the stack efficiency for the base case is expected due to higher feedstock flow rate permitted by the configuration in the system.

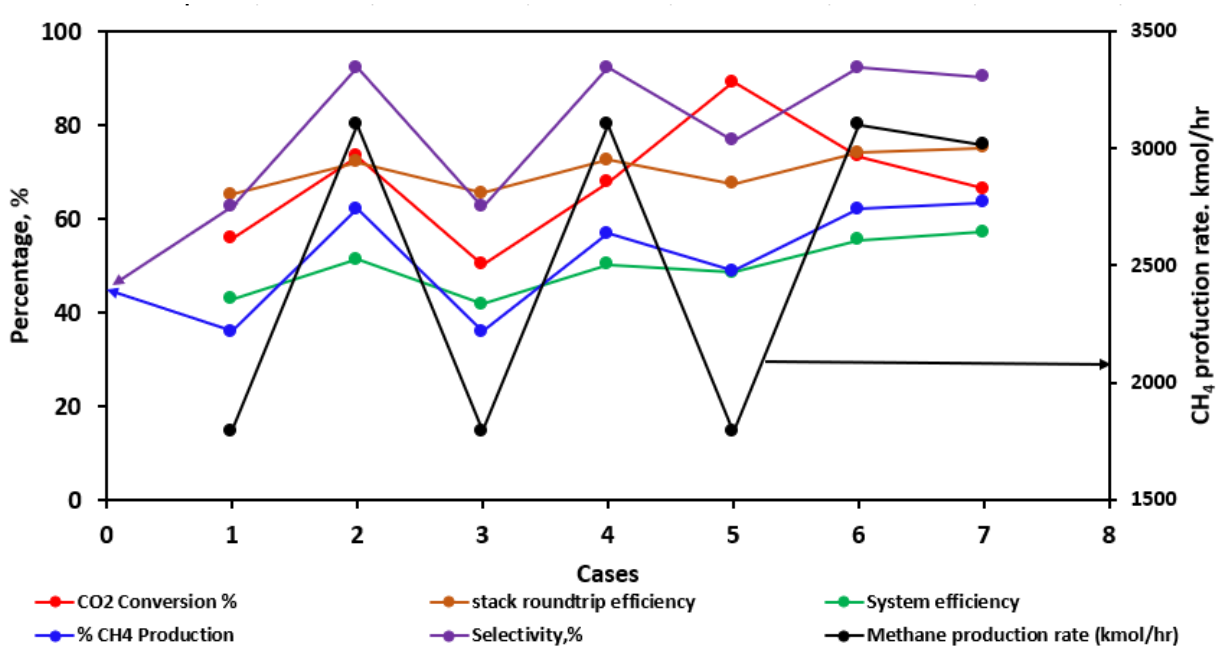

Figure 5.3: Simulation result of cases. 1= Base case, BC, 2= BC with CCS, 3= BC +RS, rr=0.2, 4= BC+CCS+RS, rr=0.2, 5= BC+CCS+RS+ H_2O, 6= BC+CCS+PS and 7= BC+CCS+ PS+Tank

Table 5.1: Simulation results for various configurations

Configurations	CO_2 Conversion %	Stack roundtrip efficiency	System efficiency	% CH_4 Production	Methane production rate (kmol/hr)	Selectivity,%
Base case, BC	55.7	65.18	42.79	35.9	1795	62.59
BC with CCS	73.3	72.1	51.37	62.01	3100.6	92.27
BC +RS, rr=0.2	50.16	65.5	41.81	35.9	1795.1	62.59
BC+CCS+RS, rr=0.2	68.72	72.48	50.24	56.8	3100.6	92.27
BC+CCS+RS+ H_2O	89.11	67.41	48.52	48.47	1795	76.7
BC+CCS+PS	73.3	74.1	55.48	62.01	3100.6	92.27
BC+CCS+ PS+Tank	66.42	75.08	57.22	63.49	3015.6	90.19

rr= Recycle ratio

5.2 Life Cycle Analysis (LCA)

The LCA process entails four fundamental frameworks, namely:

1. Goal and scope definition (system description and objectives): Base case having the carbon capture system integrated is considered. The integrated RePCEC system is powered by a solar farm housing an advanced solar photovoltaic (PV) system. The goal of this LCA is to evaluate the global warming potential of this technology for the production of methane from a co-electrolysis operation. The system boundary is as shown in Figure 5.4. The scope of this work begins with raw materials for the manufacturing of the PCEC and the BOP components and the utilities as indicated in Figure 5.5. A cradle-to-gate analysis is carried out, and the plant decommissioning is not considered. The cradle-to-gate gives and simplifies the assessment of the production process from raw material to the desired product (methane) and its use. It accounts for the carbon footprint of the continuous operation of the process unlike cradle-to-grave that account for the environmental of the whole plant with the equipment.
2. Inventory analysis (data collation-knowing and quantifying the energy and materials in and out of the system): The proposed plant embodied three separate units integrated with a combined cycled powerplant namely, the two-stage membrane-based carbon capture system, the steam generating unit that comprises other BoP components, and co-electrolysis unit that houses the RePCEC. The number of BoP components and the energy demand in each unit is as modeled in Aspen HYSYS and the throughput and products are results from the Aspen HYSYS simulation. The Ecoinvent database is relied on for the emission from the manufacturing process for secondary data and for some processes their

data are not easily accessible from literature and Aspen HYSYS. Solar farm which houses several solar PVs is used to supply power to the plant. For solar PV, local data in the United States was used from the SimaPro database.

3. Impact assessment (measuring the environmental effects of the system): SimaPro offers various standard methods for impact assessment, each encompassing 10 to 20 impact categories. However, a preferred approach is a more comprehensive method that enables the aggregation of values into a unified score. Additionally, a crucial aspect is to focus on the vital elements, classification, and characterization, as outlined in ISO 14040/44, which constitute the minimum requirements in Life Cycle Assessment (LCA). This study employs TRACI 2.1 with version 1.03 as the life cycle impact assessment (LCIA) method and adopts the US 2008 as the normalization and weighting set. The United States and North America are potential targets for this work, so its criteria are a perfect match for their set of conditions. Tool for the Reduction and Assessment of Chemical and Other Environmental Impacts (TRACI) is a midpoint oriented LCIA methodology developed by the U.S. Environmental Protection Agency specifically for the US using input parameters consistent with US locations. TRACI is an environmental impact assessment tool that provides characterization factors for Life Cycle Impact Assessment (LCIA), industrial ecology, and sustainability metrics. Characterization factors quantify the potential impacts that inputs and releases have on specific impact categories in common equivalence units. Its impact categories include Ozone depletion, Climate change, Acidification, Eutrophication, Smog formation, Human health impacts, and Ecotoxicity.

The co-electrolysis of H_2O and CO_2 from flue gas of a 600MW combined cycle power plant is carried out using an integrated RePCEC system comprising of the RePCEC stack and BoP components. The BoP components consist of the exhaust tank, compressor, heater evaporator, blower, heat exchanger, mixer, electrostatic precipitator, pump, and the two-stage membrane-based carbon capture system as shown in Figure 5.4. The environmental impact of all the components is analyzed using the TRACI 2.1 LCIA method.

Figure 5.6 shows the characterization network of all the BoP components. The thickness of the arrow indicates the contribution of a component towards the product (BOP). Selection of the right equipment from database, accurate weight allocation and well-defined boundary are critical to reliable LCA. From the figure, the pipeline that transports the natural gas is having the highest impact contribution to the environmental decadence. It has the greatest global warming contribution followed by the storage tanks. Intuitively, this seems not correct as other bigger equipment is expected to make higher environmental contribution.

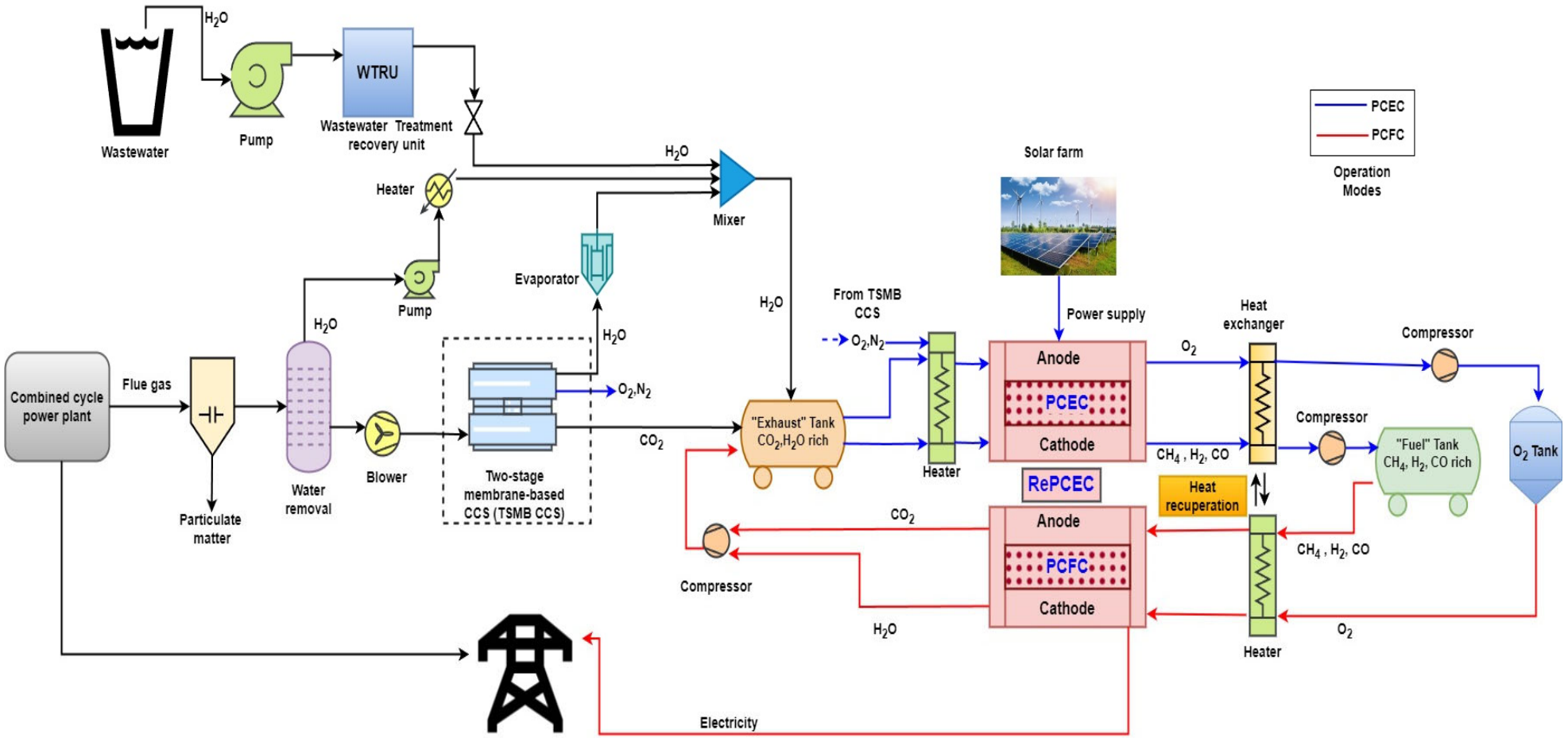

Figure 5.4: Reversible protonic ceramic electrochemical cell (RePCEC) for co-electrolysis of H_2O and CO_2 powered by solar energy

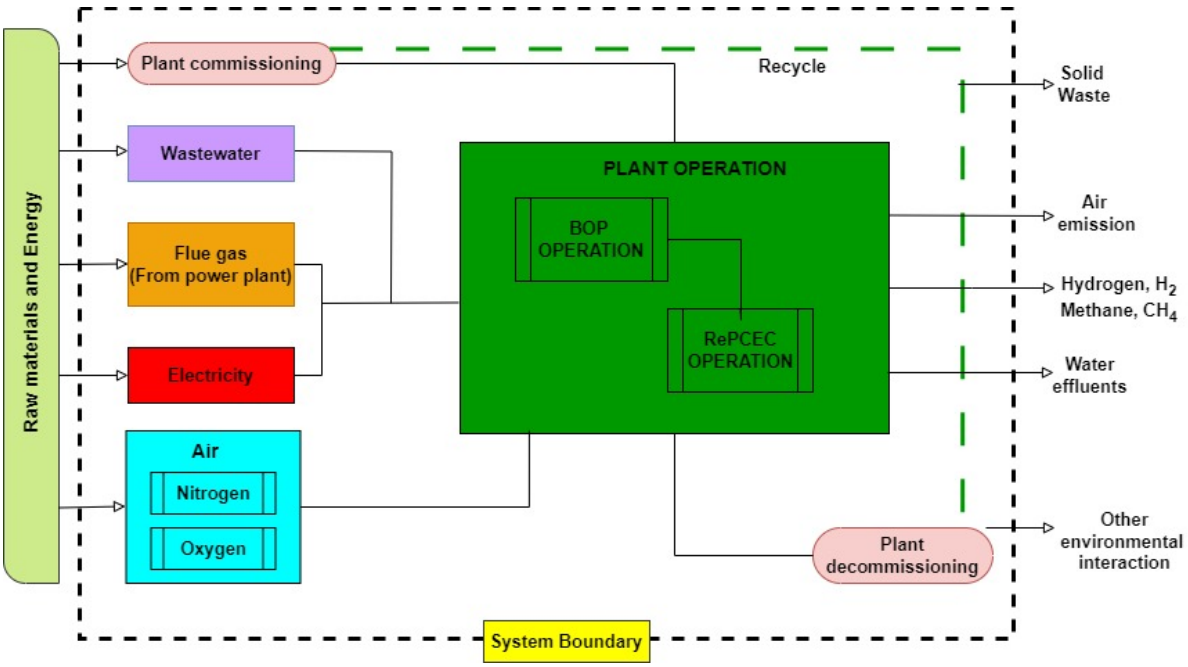

Figure 5.5. RePCEC LCA system boundary for Co-electrolysis of CO_2 and H_2O

The initially selected pipe for the process has a weighted average lifetime of 45 years made up of steel and concrete with a length of 100km, this far beyond the system boundary. This greatly contributes to the output in Figure 5.6. To correct this anomaly, the appropriate pipe with weighted average lifetime of 40 years made up similar materials as the previous one and length 3km is used. This, there is a need to reduce the transport distance to reach the storage tank. Another alternative to minimize the environmental challenge by equipment is to use more environmentally friendly materials in its manufacturing. The BoP components are a major contributor to the global warming potential of many production plants and are often avoided in LCA. Analyzing the BoP with the appropriate newly selected pipe with the right specification gives the result in Figure 5.7. From the new analysis outcome, making the storage tanks have the highest environmental impact. In fact, the pipe now has very low global warming potential compared to other equipment in the cut-off mode. The cut-off mode is the minimum weight criteria set by SimaPro to show participating equipment in the network. The cut-off in field in SimaPro also takes user input values. Components with insignificant impact contribution are not shown by the software but can be viewed in the global database.

Based on the selected LCIA method, the potential environmental impact of the RePCEC stack manufacturing is carried out to identify the impact intensity of each parameter. The global warming potential (GWP) of the stack manufacturing process is 3.63 kg CO_2 eq.

Analyzing the stack component wise, Fig 5.8 shows the contribution network of each of the stack components (most especially, the electrodes and electrolyte) during its part assembly. This figure reveals that the anode materials have the highest global warming potential which is evident from the thickness of the arrow. A deeper dive into the figure shows that nickel is the greatest polluter from the anode materials.

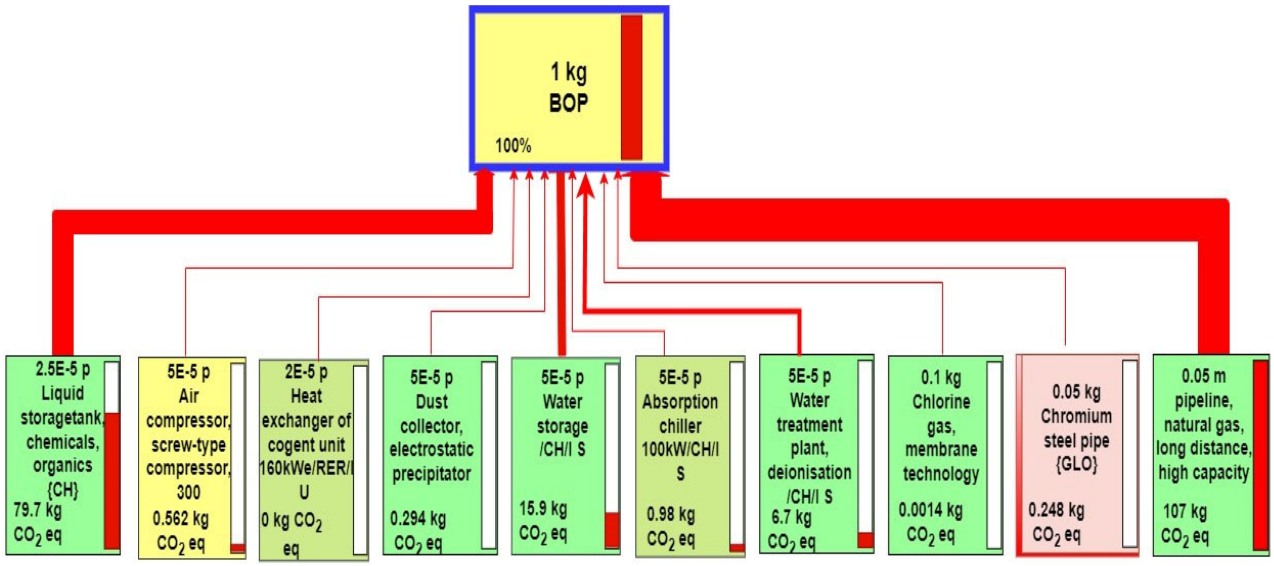

Figure 5.6: Characterization network of BoP component for co-electrolysis

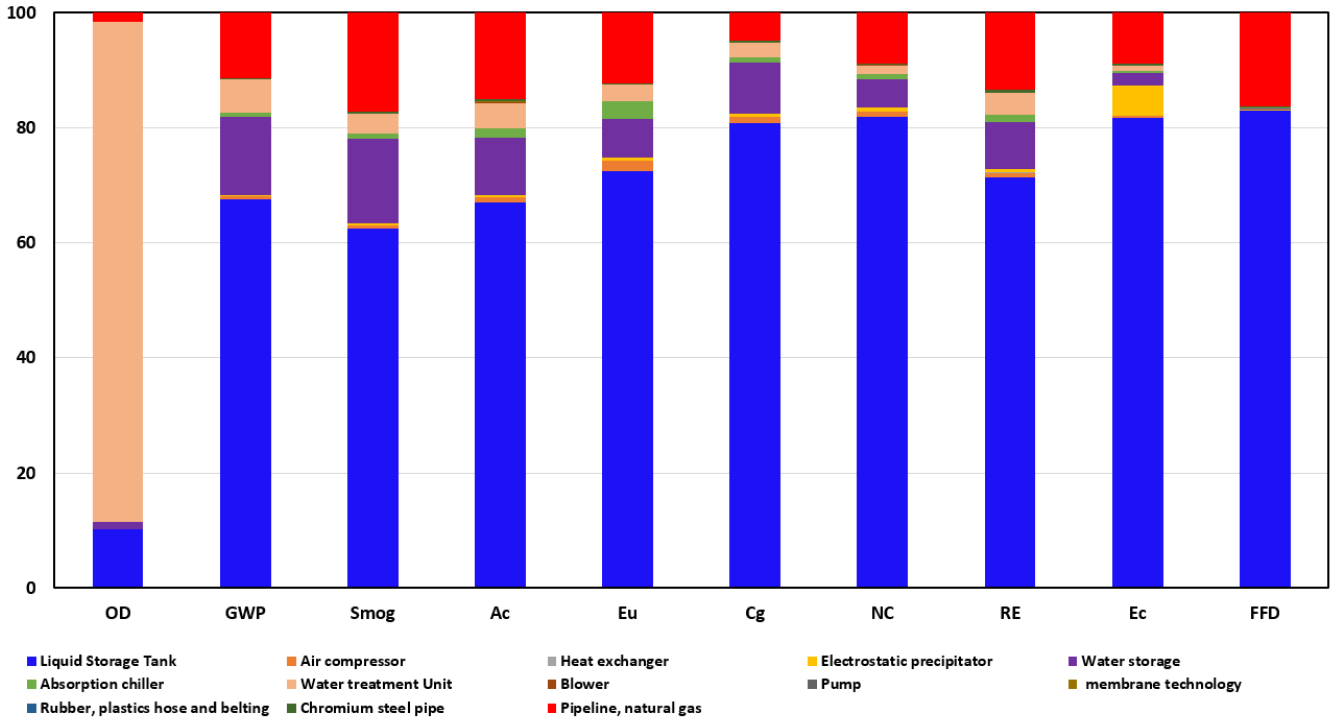

Figure 5.7: Characterization chart for BoP components for co-electrolysis

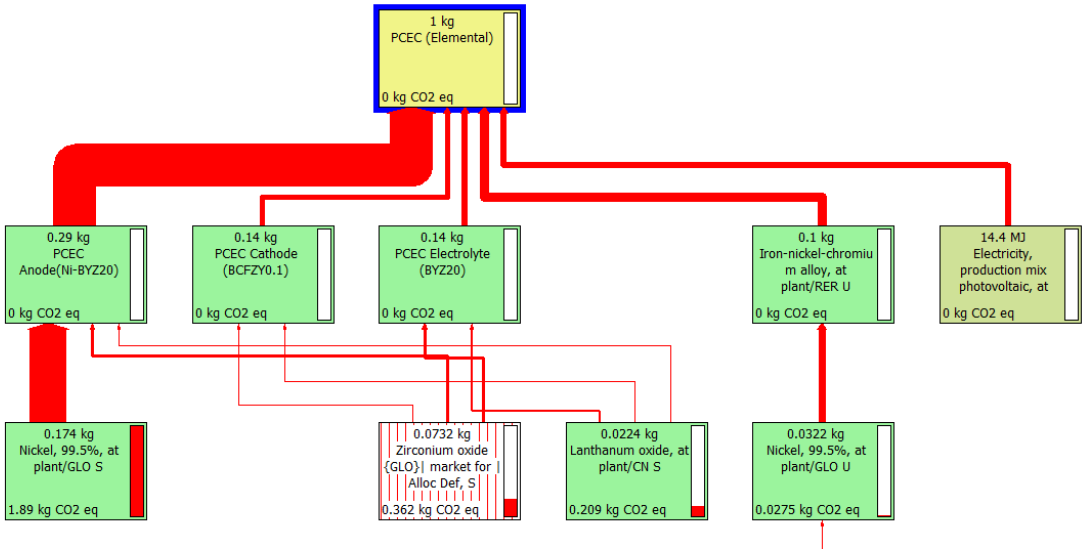

Figure 5.8: PCEC stack component analysis network

The GWP for the actual co-electrolysis operation for the production of methane and hydrogen is 3.83 kg CO_2 eq which is lower compared to 9.35 kg CO_2 eq emission during steam methane reforming for hydrogen production. Comparing the GWP for methane production via RePCEC route with power-to-gas using the energy mix EU-27 countries with 13.8 kg CO_2 eq, shows the RePCEC to be more eco-friendly. Figure 5.9 shows the contribution of each operational process, it is obvious from the graph that energy consumption during the process caused more damage. During the methane production CO_2 is removed from the atmosphere, this is shown as the green bars in Figure 5.9 which is a negative carbon footprint. The savings on each impact category is shown in green. The red bars denote the environmental impact by the energy consumed during the methanation process. Ranging the energy for steam production which takes the larger share of the process and the actual co-electrolysis reaction initialization. The effect of the electrical energy consumed cut across all impact categories.

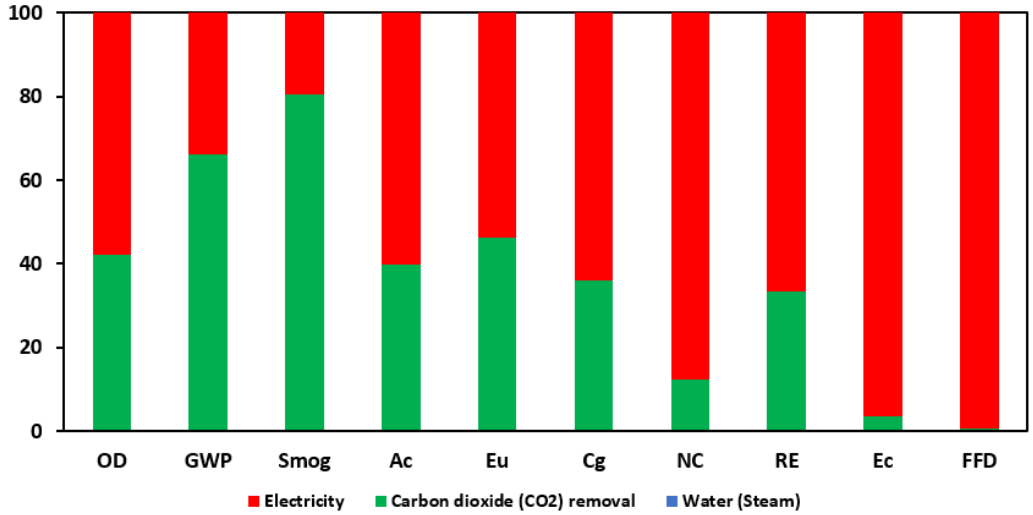

Figure 5.9: Characterization of the methane production process

5.3 Co-electrolysis RePCEC system economic analysis (EA)

The economic viability of using the RePCEC for the production of methane (natural gas) through co-electrolysis of CO_2 and H_2O is evaluated. The base case with a carbon capture system shown in Figure 5.4 is used for this study. The main feedstock flow rates into the system are 4582 kmol/hr and 20000 kmol/hr for CO_2 and H_2O respectively. This yielded an output flow rate with 4046.6 kmol/hr of methane and 3783.2 kmol/hr of hydrogen.

Using an extract from the DOE cost analysis tool, a new techno-economic analysis tool is built using the Excel spreadsheet linked with the Aspen HYSYS system model for the estimation of the level cost of methane. The product output from aspen HYSYS for the case under study, methane heating value, and its conversions is shown in Table 5.2. Considering the levelized cost of hydrogen to be \$2.5/kg of H_2, the levelized cost of methane (LCOM) is \$2.23/MMBtu exempting the separation cost of the two gases. The \$/MMBtu is the conventional unit used for the levelized cost of natural gas and the unit conversion to the metric system is highlighted in Table 5.2. Comparing this value with the Henry Hub daily spot price for natural gas (NG) which ranges between \$3.46/MMBtu and \$9.85/MMBtu as reported by the US Energy Information Administration (EIA)[1], indicates an economic potential. The LCOM is highly responsive to the LCOH since both have a unified cost being produced from the same process which must be split. Since the LCOH has been established in a separate standalone process, the LCOM becomes the dependent variable of the two costs. Also, the LCOM depends greatly on the cost of RePCEC stack being the most expensive of the equipment, and on the cost of other balance of plant components. Estimating the LCOM at various conditions gives insight into reasonable cost ranges, this gives the upper and lower limits of the LCOM obtainable from the RePCEC system. Figures 5.10 and 5.11 compare the lower and the upper bands of the LCOM with the US annual NG price and the global NG price respectively.

Table 5.2: The total capital cost and total operation and maintenance cost

S/N	**Expenses**	**Cost, \$**
1	**Direct expenses**	
a	Equipment F.o.b cost	71190913
b	Installation materials	8542909.56
c	Labor (installation)	170858.191
2	**Indirect Expenses**	
a	Freight, insurance and tax	2397140.42
b	Construction overhead	1598093.62
c	Engineering expenses	7990468.08
3	**Contingency and fee**	

[1] Lawrence, K., *Average cost of wholesale U.S. natural gas in 2022 highest since 2008*. 2023: US EIA.

A	contigency	5593327.65
B	contractor fee	3995234.04
C	Legal fee	7990468.08
4	**Auxiliary facilities**	
A	Site development	3995234.04
B	Auxiliary buildings	2397140.42
C	Off-sites and untilities	1198570.21
	Operating costs	
	Fixed	1198570.21
	Variable and others	75909446.7
	Maintenance Cost	9588561.69

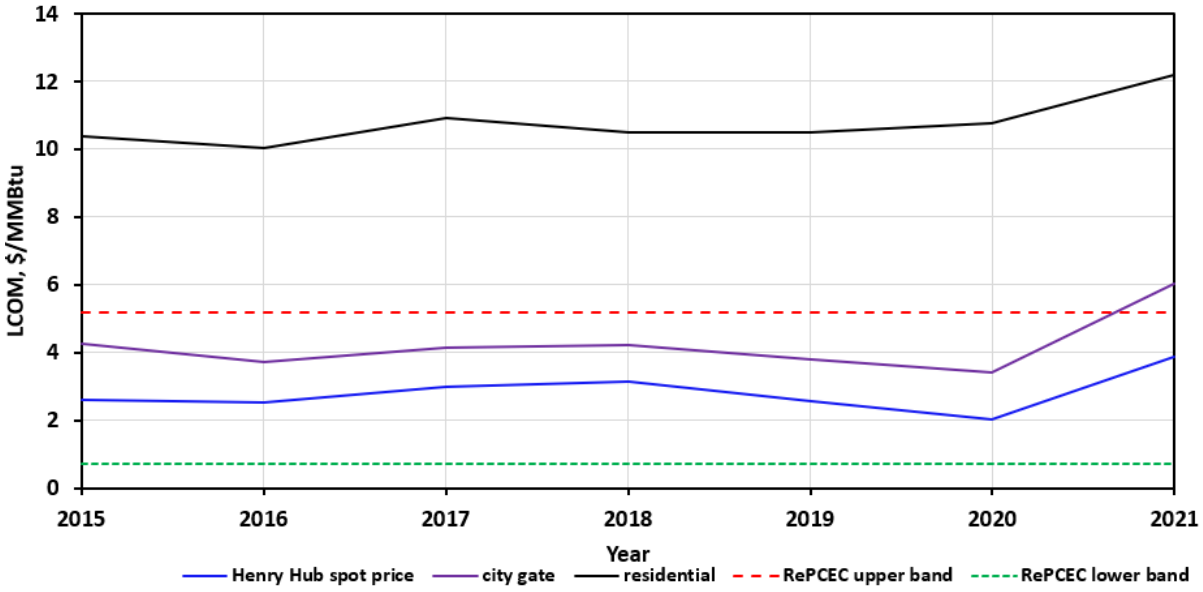

Figure 5.10: LCOM from RePCEC system compared to the US average annual prices of natural gas. Red dash line- highly inflated capital and operational costs for RePCEC system. Blue dash line-reduced capital and operational costs for RePCEC system.

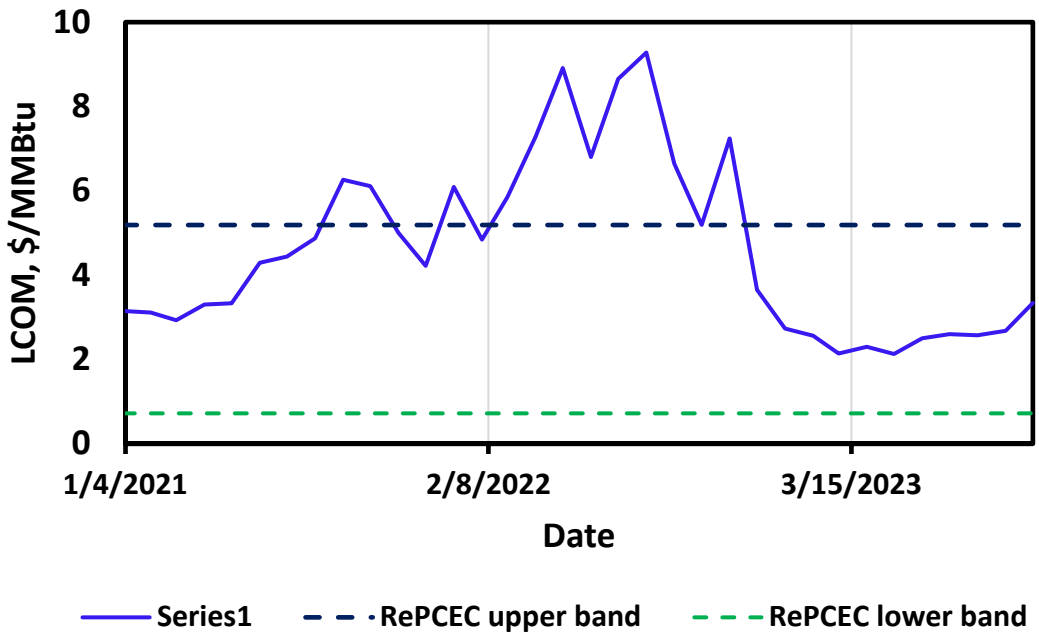

Figure 5.11:LCOM from RePCEC system compared to the US average monthly prices of natural gas from 2021-2023[273]

It can be seen from Figs. 5.10 and 5.11 that adopting the RePCEC production route for methane competes relatively strongly with other routes even in extreme cases as its upper band LCOM depicted. What is obvious from the reports is that all other feasible production routes have been considered, thus operating the RePCEC at relatively optimum conditions, with progress in driving the cost of the technology down will drastically reduce the LCOM. This can probably lead to a paradigm shift in the methane production and markets. If this technology is implemented for this purpose and the potential profitability is confirmed, it enhances the investors' interest.

Publications:

Liu F., Deng H., Diercks D. , Kumar P, Abdul Jabbar M.H. , Gumeci C. , Furuya Y. , Dale N., Oku T. , Usuda M. , Kazempoor **P**., Fang L. , Chen D. , Liu B, Duan C (2023) Lowering the operating temperature of protonic ceramic electrochemical cells to <450 °C, **Nature Energy** , https://doi.org/10.1038/s41560-023-01350-4

Liu F., Deng H., Kazempoor **P**., Liu B, Duan C (2023) Process-intensified protonic ceramic fuel cells for power generation, chemical production, and greenhouse gas mitigation, https://doi.org/10.1016/j.joule.2023.05.009

Jolaoso L, Duan, C. , P. Kazempoor (2023) Life cycle analysis of a hydrogen production system based on solid oxide electrolysis cells integrated with different energy and wastewater sources, **International Journal of Hydrogen Energy**, (2021) https://doi.org/10.1016/j.ijhydene.2023.07.129

Jolaoso L, Bello I., Ojelade O.A., Duan, C. , P. Kazempoor (2023) Operational and scaling-up barriers of SOEC and mitigation strategies to boost H2 production- a comprehensive review, **International Journal of Hydrogen Energy**, (2021) https://doi.org/10.1016/j.ijhydene.2023.05.077

Liu F; Fang L; Diercks D; Kazempoor P, Duan C, (2022) Rationally designed negative electrode for selective CO2-to-CO conversion in protonic ceramic electrochemical cells; **Nano Energy,** 102, 107722. https://doi.org/10.1016/j.nanoen.2022.107722

Jolaoso L.A, Asadi J, Duan C, **Kazempoor P** (2022). A novel hydrogen economy based on electrochemical cells using water-energy nexus framework, **Energy Conversion, and Management,** 276, 116344 https://doi.org/10.1016/j.enconman.2022.116344

Liu F; Park Y; Diercks D; **Kazempoor P**, Duan C, (2022) Superior catalyst for synthetic natural gas production under mild condition, **ACS Applied Materials & Interfaces** 14 (11), 13295-13304. https://doi.org/10.1021/acsami.1c23881

Appendix 1: Technology Maturation Plan (TMP)

Protonic Ceramic Electrochemical Reactor (PCER) technology has successfully transitioned from laboratory-scale small cells to large area stacks, achieving Technology Readiness Level 5 (TRL5) for hydrogen production. However, the application and integration of PCER with fossil fuel assets for converting CO_2 into valuable chemicals are currently at TRL 3. Large-scale stacks and systems have not yet been developed or tested in this specific context. Consequently, further research and development efforts are deemed necessary to advance PCER systems to a fully integrated and mature state.

The active research and development (R&D) phase should be initiated to propel the technology forward. This phase encompasses analytical studies and laboratory-scale experiments aimed at physically validating the analytical predictions of separate elements of the technology. The goal is to integrate the basic technological components, establishing that these pieces will function harmoniously together. This stage is relatively "low fidelity" compared to the eventual system. Examples include integrating PCERs with different sources of CO_2 and designing an integrated system capable of efficiently utilizing CO_2 to produce valuable fuels.

To propel the technology to the next level, collaborative efforts with industry partners are essential. The teams from OU and KSU are prepared to deploy the technology collaboratively. This collaboration involves combining expertise and resources to address the challenges and gaps identified in the current TRL. The collaborative effort aims to accelerate the maturation of PCER systems, ensuring seamless integration with fossil fuel assets for effective CO_2 conversion into valuable chemicals.

The following steps outline the Technology Maturation Plan:

- Integration of Technological Components: Combine basic components of PCER technology to validate their compatibility and functionality, focusing on low-fidelity, laboratory-scale integration.

- Analytical and Laboratory-Scale Studies: Conduct analytical studies and experiments to physically validate predictions related to separate elements of the PCER technology, ensuring alignment with the desired outcomes.

- Efficient Utilization of CO2: Design and test integrated systems that efficiently utilize CO_2 from different sources to produce valuable fuels. This includes exploring various CO2 capture methods and optimizing the overall process.

- Collaboration with Industry Partners: Engage in collaborative efforts with industry partners to leverage expertise, resources, and real-world applications. This collaboration is crucial for addressing challenges specific to integrating PCER with fossil fuel assets and scaling up the technology.

- Technology Deployment: Gradually deploy the technology to larger scales, moving from laboratory-scale stacks to larger area systems. Monitor and evaluate the performance of PCER systems in converting CO_2 into valuable chemicals.

- TRL Advancement: Continuously assess and document the progress, aiming to elevate the Technology Readiness Level from TRL3 to higher levels, ultimately achieving a fully integrated and mature state.

- Through this comprehensive Technology Maturation Plan, the collaborative efforts of the OU and KSU teams, along with industry partners, are expected to propel PCER technology towards practical and scalable applications for the efficient utilization of CO_2 in the production of valuable fuels.